TÉCNICO LISBOA

UNIVERSIDADE DE LISBOA
INSTITUTO SUPERIOR TÉCNICO

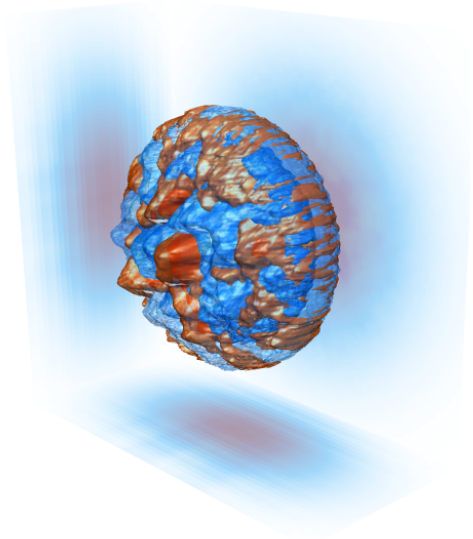

Theoretical and numerical studies of magnetic field generation in plasma astrophysics

Nitin Shukla

Supervisor: Doctor Luís Miguel de Oliveira e Silva

Co-Supervisor: Doctor Jorge Miguel Ramos Domingues Ferreira Vieira

Thesis approved in public session to obtain the PhD Degree in Physics

Jury final classification: Pass with Distinction

2019

TÉCNICO LISBOA

UNIVERSIDADE DE LISBOA
INSTITUTO SUPERIOR TÉCNICO

Theoretical and numerical studies of magnetic field generation in plasma astrophysics

Nitin Shukla

Supervisor: Doctor Luís Miguel de Oliveira e Silva

Co-Supervisor: Doctor Jorge Miguel Ramos Domingues Ferreira Vieira

Thesis approved in public session to obtain the PhD Degree in Physics

Jury final classification: Pass with Distinction

Jury

Chairperson: Doutor Luís Paulo Da Mota Capitão Lemos Alves
Instituto Superior Técnico, Universidade de Lisboa

Members of the Committee:

Doctor Robert Bingham
Faculty of Science, University of Strathclyde, Glasgow, UK

Doctor José Tito da Luz Mendonça
Instituto Superior Técnico, Universidade de Lisboa

Doctor Ricardo Parreira de Azambuja Fonseca
Escola de Tecnologias e Arquitetura, ISCTE - Instituto Universitário de Lisboa

Doctor Jorge Miguel Ramos Domingues Ferreira Vieira
Instituto Superior Técnico, Universidade de Lisboa

Funding Institutions
Fundação para a Ciência e Tecnologia, European Research Council

2019

Resumo

A origem dos campos magnéticos em astrofísica é uma das grandes perguntas científicas ainda sem resposta certa, uma vez que as grandes escalas temporais e espaciais destes campos magnéticos são considerados fundamentais na explicação de observações de erupções de raios Gama. Atualmente é aceite que instabilidades em plasma têm um papel essencial na geração e amplificação do campo magnético. Por exemplo, a instabilidade de Weibel, também denominada instabilidade de filamentação de correntes pode amplificar campos magnéticos e causar a formação de ondas de choque electromagnéticas onde as partículas podem ser aceleradas até energias muito elevadas, ao mesmo tempo que emitem fortes impulsos de radiação. Têm sido desenvolvidos grandes esforços para reproduzir estes mecanismos fundamentais em laboratório, através de experiências que preservam as diferenças de escala dos cenários astrofísicos e regidas por leis físicas semelhantes. No entanto, reproduzir estes cenários extremos no laboratório é ainda um desafio em aberto.

O progresso extraordinário em técnicas de simulação sofisticadas e o aumento do poder computacional permitem uma abordagem *ab initio* para a compreensão de uma vasta gama de problemas astrofísicos e o design de experiências que permitem reproduzir estes fenómenos em laboratório. Nesta Tese usei o código OSIRIS para realizar cálculos numéricos multidimensionais e multi-escala para investigar como podem plasmas neutros de elctroões e positrões movendo-se com velocidades relativistas ser gerados experimentalmente, e como podem ser usados para investigar a instabilidade de filamentação de correntes no laboratório. Determinei as condições limites que estabelecem critérios-chave para as observações experimentais destes processos. Adicionalmente, motivado pelas recentes observações de possíveis nuvens interpenetrantes de matéria negra, investiguei também se a matéria negra pode interagir consigo própria através de interações eletromagnéticas negras. Uma vez que o eletromagnetismo de matéria negra é semelhante ao eletromagnetismo clássico, mas apenas atua em matéria negra, explorámos este tópico através de simulações com o OSIRIS de eletromagnetismo clássico, o que permitiu estabelecer os limites superiores do rácio carga-massa da matéria negra. Finalmente, é mostrado numericamente e experimentalmente que a interação de lasers intensos com alvos sólidos pode levar à geração de campos Weibel, que competem com os campos gerados através do mecanismo da bateria de Biermann. Demonstrei que através do ajuste do perfil de plasma e da dimensão transversal do feixe laser é possível observar campo magnético Weibel em experiências de interação laser-alvo para testar a microfísica relevante da geração de campos magnéticos no laboratório.

Palavras-chave:
Simulações Multi-Escala; Fusão por Confinamento Inercial; Astrofísica em Laboratório; Aceleradores Baseados em Plasma; Novas Fontes de Radiação

Abstract

The origin of magnetic fields in astrophysics is one of the grand scientific questions still without a definite answer. For instance, large-scale and persistent magnetic fields are thought to be essential to explain Gamma-ray bursts observations, but their origin is still an argument of debate. It is currently accepted that plasma instabilities can play a key role in magnetic field generation and amplification. The Weibel or Current Filamentation instability, for instance, can amplify seed magnetic fields and lead to the formation of electromagnetic shocks where particles can be accelerated to very high energies, while also emitting strong radiation bursts. There have been strong efforts to recreate these key mechanisms in the laboratory, through scaled experiments which are governed by similar physical laws. Reproducing these extreme scenarios in the laboratory is still, however, an open challenge.

Outstanding progress in simulation techniques and increasing computation-al power allow for an *ab initio* approach to understanding a wide range of astrophysical problems and the design of these upscale experiments. In this Thesis, using full scale, multi-dimensional numerical calculations employing the particle-in-cell code Osiris, I explored how electron-positron fireballs, that have been produced experimentally, could be used to probe the current filamentation instability in the laboratory. I derived a set of threshold conditions that establish key criteria for the experimental observations of these processes. In addition, motivated by recent observations of potential dark-matter interpenetrating clouds, I also investigated if dark-matter could interact with itself through dark electromagnetic interactions. Because dark-matter electromagnetism is similar to classical electromagnetism but acting only on dark-matter, I studied this topic using classical electromagnetic Osiris simulations, which enabled to set upper limits to the dark matter charge-mass ratio. Finally, it is shown, both numerically and experimentally, that the interaction of intense lasers with solid targets could lead to the generation of Weibel-magnetic fields, which competes with Biermann battery. I have demonstrated that by tuning the plasma profile and large spot size, it is possible to observe Weibel-magnetic fields in the laser-target experiments and, thus, to test the very important microphysics of generating the magnetic field in the laboratory.

Keywords:
Multi-Scale Simulations; Electron and positron beam-plasma interactions, Laser-plasma experiments; Laboratory Astrophysics; Gamma-Rays-Bursts, Dark-electromagnetism

ACKNOWLEDGEMENTS

This thesis is the result of a scientifically stimulating atmosphere and the support of all the infrastructures that I could have accessed at the Grupo de Lasers e Plasmas (GoLP), Instituto de Plasmas e Fusão Nuclear, in Instituto Superior Técnico (IST), during my Ph.D. degree.

According to Butch Rovan, "[Mentors] show you something about yourself that you didn't realize.". This is exactly how I feel about my supervisor Prof. Luis O. Silva. I am indebted to his constant guidance and continuous support. He has been an inspiration to me as a scientist, as an amazing mentor and a group leader. I feel privileged to have work in his group and live the extraordinary years of my life.

I offer deep regards to Dr. Jorge Vieira, my co-supervisor, for guiding my work during my doctoral program.

I also thank Prof. Ricardo Fonseca for helping me with particle-in-cell simulations.

I would like to thank Dr. Kevin Michael Schoeffler for his scientific guidance and friendship.

My special thanks to Dr. Elisabetta Boella, for the scientific guidance, companionship, friendship, and the patience.

My acknowledgments extend to my past and present colleagues for cooperation and direct/indirect help. Special thanks to Dr. Anne Stockem Novo, Dr. Ligia Diana Amorim, Dr. Mickäel Touati, Dr. Joana Martins, Dr. Thales Silva, Dr. Swen Kunzel, Dr. Ujjwal Sinha, Dr. Marija Vranic, Dr. Thomas Grismayer, Dr. Wenlong Zhang and Dr. Timon Mehrling for many scientific discussions.

I would like to thank Paulo Ratinho for his technical support and Ana Luisa Matias for her logistic support. I am deeply thankful to Anabela Gonçalves and Carla Reis for her kindness, friendship, and support.

I am also genuinely thankful to all my friends for sharing amazing and meaningful time.

I would like to thank my mother Kaminee Shukla for all the scarifies and support. I would like to extend deepest regards to my aunt Mrs. Ranjana Shukla. I express my

love to my sisters Rashami, Pushpnajali, Shakshi and Priyansi. I would like give warm regards and love to my brothers Prashant, Pradhiman, and Pushpesh with whom I shared my great time in Germany. I am extremely grateful to my uncle Shri Surya Kant Shukla who supported my family in bad and good times. Without his help, it would have been difficult to pursue my degree with such ease.

Finally, this work is dedicated to my to my Uncle Padma Kant Shukla and my father Prabha Shankar Shukla, whom I miss every day.

CONTENTS

LIST OF FIGURES

List of Tables

CHAPTER 1

INTRODUCTION

1.1 MOTIVATION

Relativistic and non-relativistic plasma outflows are ubiquitous in astrophysical environments like the Gamma Ray Bursts (GRBs), Supernova Remnants (SNRs), TeV-Blazar, Active Galactic Nuclei (AGN) and Pulsar Wind Nebulae (PWN) [1–3]. Much of the Universe is filled with these energetic particles. In these explosions, energies between 10^{30} to 10^{50} ergs are released in a few seconds making them the brightest and most energetic events in the universe [4, 5]. At such high energies matter exists in the plasma state. Thus, the interactions of these particle flows with the external medium becomes increasingly important for a better understanding of extreme astrophysical events. Some of the underlying physical mechanisms in these flows have strong connections with the dynamics and physics of plasmas, and many outstanding problems in astrophysics are closely associated with scenarios where the collisionless dynamics of plasmas can play an important role [6–8]. In particular, some of the long-standing quests in astrophysics are related to the origin of magnetic fields and to the physics involving magnetized flows of charged particles, close to equipartition, where the magnetic field energy is close to the kinetic energy of the flow. In particular, radiation from GRBs indicate the presence of a power law distribution of particles and magnetic fields of strengths close to sub-equipartition levels. For instance, observations of GRBs in afterglow region seems to indicate that the most likely prompt emission is being arisen from synchrotron emissions, which can only be explained due to the presence of strong magnetic fields. Several models have been formulated in the past few decades to explain such observations as well as to design laboratory experiments to develop a better understanding [9–11]. However, studying the self-excitation large scale magnetic field B in GRBs [12, 13], is a still challenging problem.

1.2 HISTORY OF GRBS

More than five decades ago, GRBs were accidentally discovered by the U.S. Vela satellites and which was designed to detect gamma radiation pulses emitted by nuclear weapons tested in space [14]. Although the purpose was to monitor any nuclear activity by the Soviet Union or other nations, the Vela satellites instead detected intense bursts of GRBs coming from deep space. This was one of the most important discoveries in astrophysics of the century. Since then, several GRBs have been observed. In 1991, the Burst and Transient Source Experiment (BATSE) was launched to understand the source of these mysterious events. Over a period of 9 years of continuously monitoring the sky, BATSE recorded thousands (8000 triggered events) of GRBs (1 per day on average). On March 26 2000, the BATSE released incredible results suggesting the evidence of the cosmological distribution of GRBs Fig. [1.1]. Further

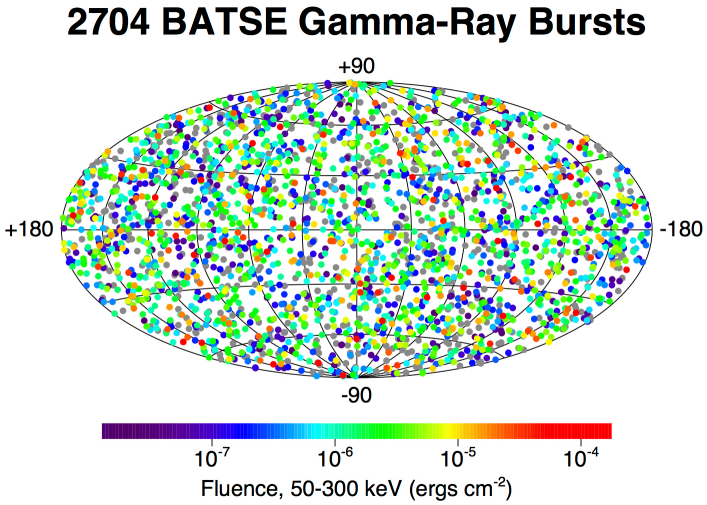

FIGURE 1.1: The locations of 2704 Gamma-Ray Bursts recorded with BATSE in galactic coordinates distributed isotropically. The projection is in galactic coordinates; the plane of the Milky Way Galaxy is along the horizontal line at the middle of the figure. The burst locations are color-coded based on the fluence, which is the energy flux of the burst integrated over the total duration of the event. Long duration, bright bursts appear in red, and short duration, weak bursts appear in purple. Grey is used for bursts for which the fluence cannot be calculated due to incomplete data.

progress in research of GRBs was made with the launch of Italian-Dutch satellite BeppoSAX (1997-2003), which was equipped with detectors of both gamma- and X-rays and observed for the first time the X-ray afterglow coming along with a GRBs [15, 16]. In the fall of 2004, NASA launched the Swift satellite dedicated to solve the mystery of

GRBs. It was equipped with three instruments, Burst Alert Telescope (BAT) to detects gamma rays, X-ray Telescope (XRT) for detecting Xrays, and Ultraviolet/Optical Telescope (UVOT) for optical afterglows. The satellite sends the locations of GRBs within seconds of detection to both ground and space-based telescopes around the world. On October 27 2015, Swift detected 1000th of GBRs (GRB 151027B). Despite such large number of observations, the physics of GRBs remains unknown. GRBs are the most explosive flashes of cosmic γ-rays that have been ever detected since the Big-bang [17]. These rare events that can roughly last anywhere from a milliseconds (30 ms) to tens of minutes (1000 s). In most cases an observed peak energy around 100 keV. A typical photon from a GRBs carries 100,000 times more energy than visible light, and is hundreds of times brighter than a typical supernova and about a million trillion times as bright as the Sun. It is caused by very energetic explosions, when a large amount of energy $E \sim 10^{51} - 10^{53}$erg ($10^{44} - 10^{46}$ Watt) is released over a few seconds in a small volume assuming isotropic emission. It is widely accepted [18,19] the GRB huge luminosities involves a newborn stellar-mass black hole emitting a relativistic collimated outflow (figure 1.2). There is ample amount of evidence revealing that the GRBs are collimated into jets, with opening angles of a few degrees only [20,21].

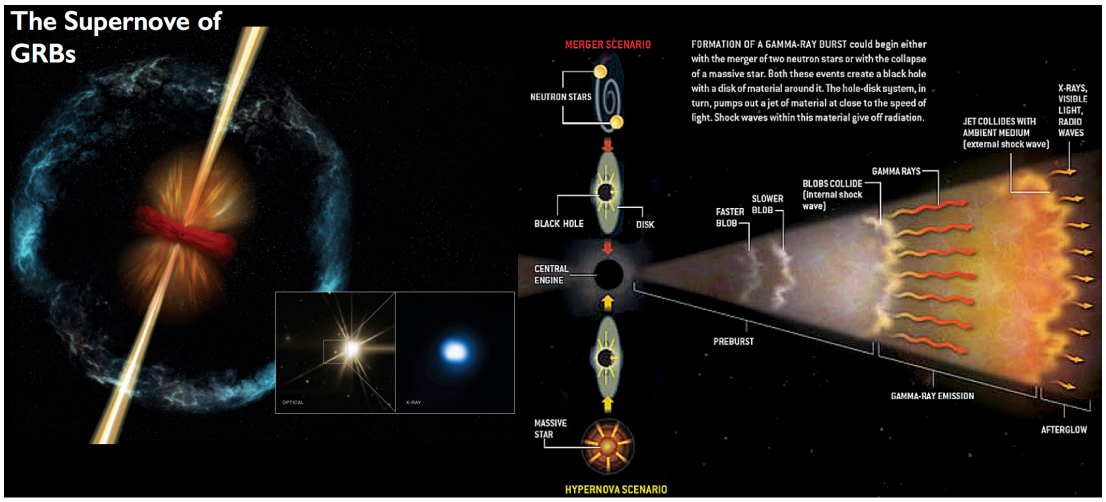

FIGURE 1.2: Cartoon shows the schematic of the GRB fireball model: (1) The source of energy is a collapse of a massive star (2) A compact source produces a relativistic outflow. This could be mediated by hot photons ("fireball model"), or by magnetic field (3) Internal shocks within the outflows produce prompt γ-rays emission (4) while external shocks with the surrounding matter produce the lower energy and longer lasting afterglow. The remaining kinetic energy is deposited into the surrounding medium. (credit NASA).

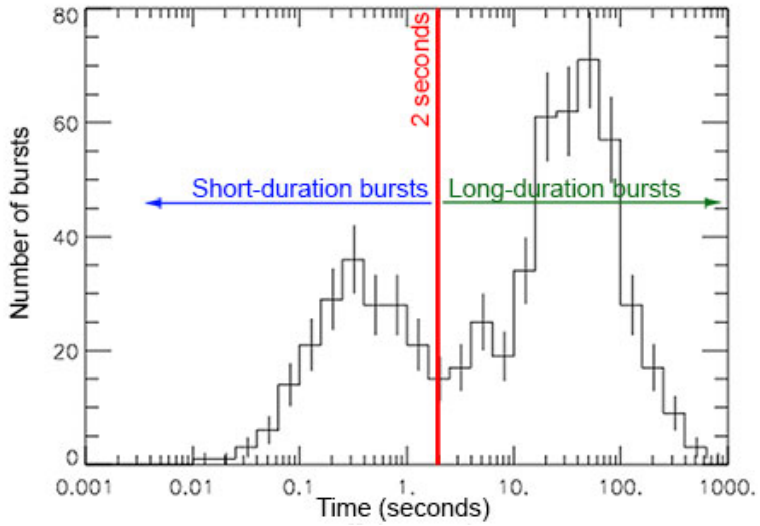

FIGURE 1.3: Graph of the duration versus number of bursts for the gamma-ray bursts observed by the BATSE instrument on the Compton Gamma-ray Telescope *Peer, 37 2015 Advances in Astronomy (2015).*

1.3 THEORY OF THE GRBS

GRBs can be broadly classified into two groups based on the time, T_{90}, it takes to release 90 % of its total energy. GRBs with $T_{90} < 2s$ are called short duration bursts and those with $T_{90} > 2s$ are long duration. The distribution of long and short duration bursts reported by the BATSE instrument is shown in Fig. [1.3] [22]. Gamma ray spectrums have been observed to have peak energies of $\sim 100\,\text{keV}$ and obey a power law distribution given as,

$$N(E)dE \propto E^{-\alpha} \tag{1.1}$$

with a spectral index $\alpha \approx 2$, where N is the number of photons with energy E. The spectrum is non-thermal and can be detected about once per day.

The intriguing feature about GRBs is that it releases enormous amount of energy in a very short time, and objects responsible for the GRBs (”the internal engine”) is still unknown due to the optical thickness of the engine. How can such an emission take place from a compact source is an open question? The detection of GRBs 030329 suggests that core-collapse events during the death of massive stars can give rise to GRBs (see figure 1.2). The engine of many other explosions is still under debate. This is knowns as the compactness problem [23–25].

1.3.1 THE COMPACTNESS PROBLEM

The compactness problem arises due to the combination of the large energy involved, short-time variability and observed non-thermal spectrum. For a typical GRBs corresponds to F $\sim 10^7$ erg cm^{-2}, for an isotropic source at a distance D, the total isotropic γ-ray energy released is

$$E = 4\pi D^2 F = 10^{50}\mathrm{ergcm}^{-2}\left(\frac{D}{3000Mpc}\right)^2\left(\frac{F}{10^{-7}}\mathrm{ergcm}^{-2}\right) \tag{1.2}$$

The scale of emission area is $c\,\Delta t = 3000$ km and implies that the sources are compact with a size R_i ($< c\,\Delta t$). By assuming isotropic emission, this energy E is sufficient to annihilate γ-rays and produces $\gamma\gamma \rightarrow e^-$, e^+ pairs, if the energy in their center-of-mass frame is larger than $2m_e c^2$, the implied optical depth is [22–25]:

$$\tau(\gamma\gamma) \simeq \frac{f_p \sigma_T F D^2}{R_i^2 m_e c^2}$$
$$\sim 10^{13} f_{2m_e c^2}\left(\frac{F}{10^{-7}}\mathrm{ergcm}^{-2}\right)\left(\frac{D}{3000Mpc}\right)^2\left(\frac{\Delta t}{10msec}\right)^{-2} \tag{1.3}$$

where f_p is the photon energy needed to produced e^-/e^+ ($2 \cdot 0.511MeV \sim 1MeV$) and σ_T is Thomas cross section, m_e is the mass of e^-/e^+ and c is the speed of light.

For typical parameters, $D \simeq 100$ kpc, $\sigma_T = 6.25 \times 10^{-25}$cm^2, the resulting pair production optical depth is $\sim 10^{15}$, we get very large optical depth for any reasonable values of f_p and that would therefore mean that the sources are optically very thick to pair production (known as the compactness problem). However, the observed non-thermal spectrum indicates with certainty that the sources must be optically thin. Arguably, there is only one way to get rid of this apparent paradox by considering a source moving at a high relativistic Lorentz factor γ towards the observer. Hence "the new physics" of relativistic motion is inevitable.

There are two ways to resolve this issue: first, the photon energy is blue-shifted by a factor of γ, and therefore the energy at the source frame is reduced by a factor $\gamma \sim \sqrt{1 - v^2/c^2} \gg 1$, hence this significantly reduces the number of photons above the pair production threshold, i.e $f_{2m_e c^2}$ drops by a factor $\gamma^{-\alpha}$. Therefore, the radius from which the radiation is emitted is reduced by a factor of γ^2

$$\tau(\gamma\gamma) \simeq \frac{f_{2m_e c^2} \sigma_T F D^2}{\gamma^\alpha R_i^2 m_e c^2}$$
$$\sim \frac{10^{13}}{\gamma^{4+\alpha}} f_{2m_e c^2}\left(\frac{F}{10^{-7}}\mathrm{ergcm}^{-2}\right)\left(\frac{D}{3000Mpc}\right)^2\left(\frac{\Delta t}{10msec}\right)^{-2} \tag{1.4}$$

The second effect is to introduced the relativistic outflow from generating the real physical scale of the emission region $R_i < \Gamma^2 c\Delta t$ for an observed timescale of Δt. Hence, the problem of compactness can be solved if the source is moving with a Lorentz factor $\gamma > 10^{13/(4+\alpha)} \sim 10^2$. A small fraction of photons is energetic enough in the outflow rest frame to produce e^-, e^+ pairs. The non-thermal spectrum indicates that the observed emission emerges from an optically thin region. To overcome this problem it is widely accepted that the source is moving relativistically with a lower limit of $\gamma \sim 100$. This leads to the relativistic fireball model. A more detailed description of the Compactness problem is discussed in [23, 24].

1.3.2 THE FIREBALL MODEL

The fireball model relies on the dissipation of kinetic energy of an ultrarelativistic flow, where huge amount of energy ($10^{52} - 10^{53}$ erg) is released in such a short time and compact volume. A fraction of the energy ($\sim 10^{-3} - 10^{-2}$ of the total energy) transfers in to high temperature ($\geq MeV$) plasmas. As a result, abundant electron-positron ($e^-\ e^+$) pair plasmas via photon-photon interactions and a small amount of baryons are produced, known as the fireball [26,27] creating a hot fireball which would expand, eventually reaching relativistic bulk velocities. The interaction of the fireball beam, characterised by relativistic factors ranging from $10^2 - 10^6$, with the external medium can drive field structures that accelerate particles to high energies. As particles accelerate to such high energies, the kinetic energy of the jets is dissipated (by internal collisions, in this picture) to produce strong radiation bursts, with wavelengths ranging from γ-rays to radio waves. The remaining part of energy is deposited into the interstellar medium (ISM), heating it and producing the observed afterglow.

The main idea leading to the fireball model involves the gamma-ray emission in GRBs radiates behind a shock that has developed within a shell moving with a Lorentz factor $\gamma > 1$. In particular, the model, depicted in Fig. 1.4, considers

1. **Sources of inner engine:** The core of fireball model is inner engine which ejects a collimated ultrarelativistic electrons and positrons (e^-, e^+) with a Lorentz factor $\gamma \sim 100$ from a compact sources ($10^6 - 10^8$cm) shown in Fig. 1.4 (1). It is believed that the inner engine of a GRBs are either a neutron star or a black hole [17, 23].

2. **Transport of energy:** The general statement of these theories predicts that γ-rays thermalization, caused by photon-photon and electron-positron pair creation, is avoided due to the highly relativistic motion of shells. The energy is relativistically transferred from the source to optically thin regions whose radius is $\sim 10^{10}$cm (Fig. 1.4 (2)).

3. **Conversion of kinetic energy into GRB prompt emission:** The bulk Lorentz factor increases linearly as the fireball shell expands. It accelerates leptons with

higher Lorentz factor $10^3 - 10^4$ by radiation pressure (see Fig. 1.4 (3)). The ultra-relativistic ejecta is slowed down and the shocks arising when faster shells overtake slower ones convert the kinetic energy in internal energy of accelerated particles (electrons, positrons, baryons), which in turn emit the observed prompt γ-rays via synchrotron radiation through internal shocks that take place 10^{13}-10^{15}cm.

4. **Afterglow in external shocks:** The relativistic outflow, whose speed has been decreased by the internal shocks but that has not been stopped, is further slowed down by the surrounding interstellar medium (ISM) at $\sim 10^{16}$cm producing the afterglow (Fig. 1.4 (4)).

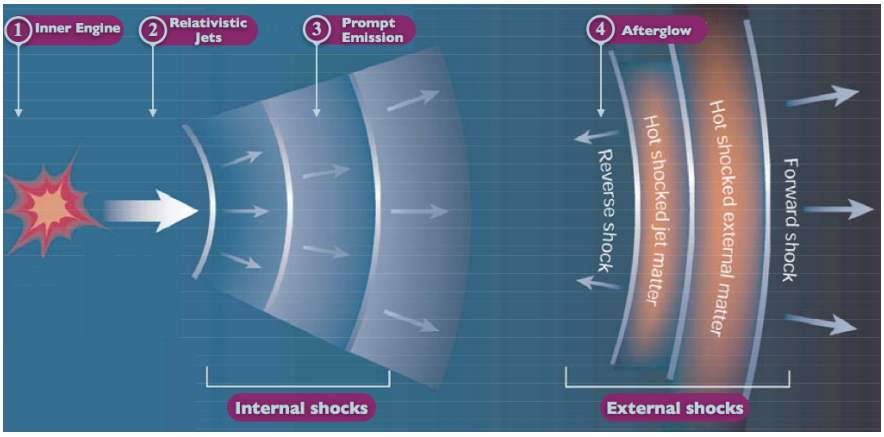

FIGURE 1.4: A schematic diagram of the internal-external shocks model. The magnets depict the essential magnetic fields in this model and their typical values (Crdit: Jaroschek [28]).

Despite of the general acceptance of the model, one of the open questions involves the conservation of kinetic energy of the plasma shells into the nonthermal radiation. Astrophysical observations indicate that the main process leading to radiation emission is synchrotron radiation, which requires large amplitude magnetic fields on the order of G to operate [27, 29]. The origin of magnetic fields, and their amplification to these extreme values is a pressing challenge in astrophysics [3, 29].

1.3.3 MAGNETIC FIELDS IN GRBS

There has been an extensive effort, based on theoretical and numerical advances, with the objective of understanding the mechanisms by which strong magnetic fields are formed in astrophysical scenarios [30–32]. The general consensuses in the scientific community is that plasma instabilities are plausible mechanisms for the magnetic field generation in astrophysics, especially in Gamma-Ray Bursts (GRBs). The

natural occurrence of these plasma instabilities growing density and thermal fluctuations may generate strong magnetic fields which are required to explain the nonthermal radiation [33]. It was suggested that the Current filamentation/Weibel instability (CFI/WI) plays a crucial role in generating relatively strong magnetic fields such that $\omega_c/\omega_p \sim 1$, where ω_c is the cyclotron frequency and $\omega_p = 4\pi n_0 e^2/m_e$ the plasma frequency, from ambient B-field fluctuations [34]. The discription of the kinetic energy of the flow to the amplifications of the magnetic fields leads to the on-set of collisionless shocks, where particles can be accelerate in a Fermi-like accelerations process, where the magnetic field was observed to be amplified substantially at the shock front. Often, an electromagnetic wave propagating ahead of the shock is present, the so-called precursor [35, 36]. The large size of the shock provides enough time for plasma instabilities to occur between the precursor and the surrounding medium. Here, we do not provide a full consistent theory of the shock model, but focus on the precursor regime and the generation of plasma instabilities and the self-consistently generated magnetic field.

The connections between the CFI/WI and GRBs can be described in the following way; When a GRB explodes, it ejects out a dense relativistic jet which collides with the interstellar plasmas. Thus, a counter-streaming return current forms and the instability can grow. In general, longitudinal and transverse instabilities occur simultaneously. Theoretical studies have been made that demonstrate the fastest growing instability which can generate strong magnetic fields [37]. Purely transverse electromagnetic instabilities generate strong magnetic fields which scatter charged particles, emitting the electromagnetic radiation through synchrotron like processes. Numerical simulations reveals the validity of the above mechanism in astrophysical scenarios [38]. Many 2D and 3D numerical simulations have been performed by colliding two plasma shells [39, 40]. Simulation results show that when the magnetic fields are strong enough, charged particles are trapped in the magnetic field. This magnetic field merges into wider filaments causing the magnetic energy to cascade from the initial skin depth scale c/ω_p to larger scales. The magnetic fields saturates typically at a time scale of the order 100 ω_p^{-1}. After the saturation of the instability it is important to understand the relative distribution of magnetic field energy and the kinetic energy of the flow. To explain the GRBs, this relative distribution needs to be close to equipartition, i.e. the magnetic field is comparable to the kinetic energy of the flow. Medvedev and Loeb [41] studied the relativistic two-stream (Weibel) instability in an astrophysical scenario and predicted a near equipartition field distribution, where the magnetic field energy density is comparable with the initial particle energy density. The ratio between the energy density in the B-field and the initial kinetic energy density is of the order of $10^{-3} - 10^{-5}$ [40–42]. In the case of a pure electron-positron plasma, computer simulations have conclusively demonstrated that the generated magnetic field reaches sub-equipartition and grows to about 10% of initial kinetic energy density [40]. These

predictions for the equipartition parameter $10^{-2} - 10^{-1}$ agree with the values inferred from GRBs afterglows. It is concluded that this instability can be the main mechanism to generate sub-equipartition magnetic fields required to explain the afterglow emission of GRBs.

1.4 DARK-ELECTROMAGNETISM

The nature of the dark matter comprising over 23% of the mass of the universe remains a mystery. Having been observed only through its gravitational interactions [43], we know very little about the underlying particle physics of dark matter. A huge array of theoretical possibilities remains open, spanning a 50 order-of-magnitude mass range from $\sim 10^{-22}$ eV to $\sim 10^{19}$ GeV. Dark matter could have a wide variety of possible non-gravitational interactions both with itself and with other particles. Although all we can currently say is that they must be weak enough to have evaded observation. Discovering such interactions would be a huge leap forward in understanding dark matter, and is one of the biggest goals of modern particle physics.

It was recently proposed that with the constrain of dark fine-structure constant ($\alpha_D = 10^{-3}$) and the mass of the Dark matter (DM) ($m_{DM} \leq 10$ TeV), weak dark matter self-interactions could naturally occur with possible observable consequences for large scale structure and halo dynamics. A minimal type of DM self-interaction is a "dark electromagnetism", which could cause DM to exhibit collisionless plasma-like collective behaviour [44]. Besides their difference in charge to mass ratio, DM plasmas can be considered to be cold and collisionless plasma. One of the key questions that has been pointed out is whether plasma instabilities may have significant impact on galactic dynamics [45]. Resolving this will determine whether or not such an interaction is consistent with current observations, and whether plasma instabilities may have significant impact on galactic dynamics.

1.5 INERTIAL CONFINEMENT FUSION (ICF)

The recent developments of ultra-intense laser beams (intensity of the order of $10^{21} - 10^{22}$ W/cm^2) with durations shorter than 1 picosecond (ps) open new possibilities to study different mechanisms for magnetic field generation that can be relevant in inertial confinement fusion (ICF) experiment [46, 47]. In this approach, a small spherical pellet containing micrograms of deuterium-tritium (DT) is compressed by powerful laser beams. The enormous energy influx explodes the outer layer of the target; the remaining portion of the target is driven inward. As a result, a shock wave forms which is hot and dense enough to ignite the DT fuel [48]. Two approaches have been systematically investigated:(i) direct drive and (ii) indirect drive. In indirect drive

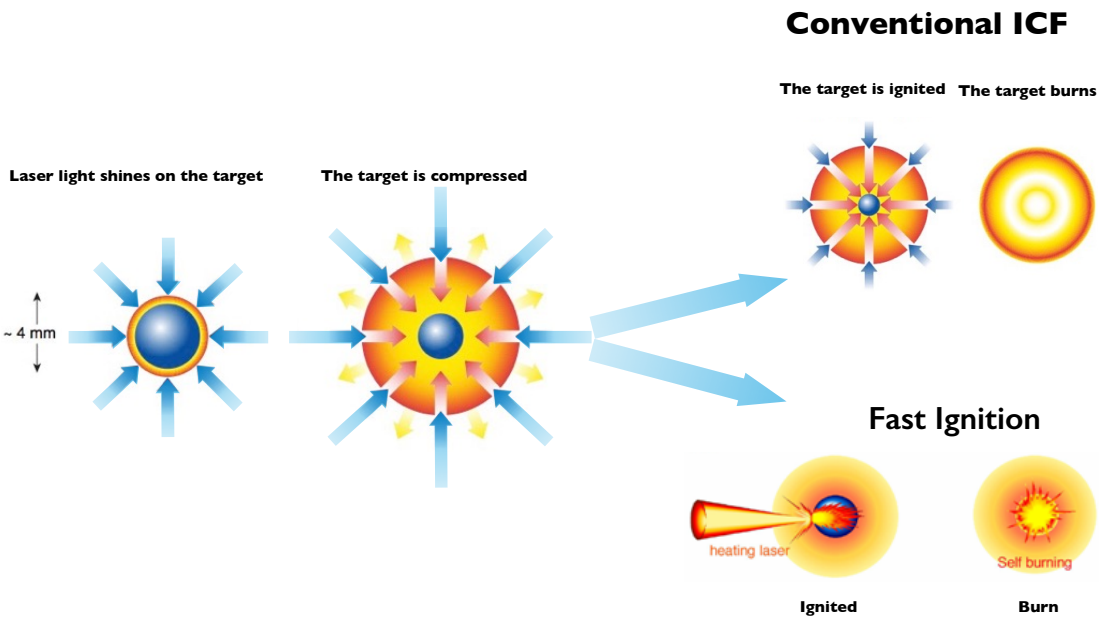

FIGURE 1.5: The standard scheme of Fast Ignition (FI): (a) capsule of DT fuel with an imbedded cone of gold is irradiated by many symmetrically arranged laser beams, (b) the material converges around the tip of a gold cone. The density of the DT is now hundreds of times the density of solid material, (c) An ultra intense laser is fired onto the gold cone. When the laser beam interacts with the tip of the gold cone, a large number of energetic electrons are produced, (d) The energetic electrons travel into the dense DT fuel and deposit their energy. This raises the fuel to 100 million degrees centigrade, which is hot enough to initiate the fusion reactions. (Courtesy of HiPER)

the laser energy is converted into x-rays by the interaction with the holharum [49] to obtain a symmetric compression from a limited amount of laser beam lines whereas in the direct drive scheme a large number of beam lines is used to directly obtain a symmetric compression directly from the laser light [50]. The fast ignition scheme (FIS) is a more recent and an alternative approach to ICF. Using this scheme, very high energies can be obtained by using a low energy driver. Thus, being very efficient in terms of energy gain. It is also less expensive than conventional inertial confinement fusion. The scheme of FI [51] is illustrated in figure 1.5. In this scheme, a capsule of DT fuel is implanted on a gold cone. The spherical pellet of DT is compressed having a density in the core of a target of the order of $300\,g/cm^3$. Then, a very-short ($\sim 10\,ps$) high-power (70 KJ, 4 PW) intense laser beam is incident on the gold cone. When this pulse interacts with the fuel, it produces energetic electrons (3.5 MeV) with relativistic velocities. These electron beams transport the energy to ignite the hot spot in the core of the pre-compressed target and heat up the fuel to 100 million degrees centigrade, which is hot enough for thermonuclear reactions [52, 53].

1.6 Magnetic Field Generation in Laser-Plasma Interactions

The generation of strong magnetic fields is not only a topic of fundamental interest in the extreme astrophysical objects but it also has importance in laser-plasma experiments where similar physical processes could also be provoked. The advent of multi-terawatt lasers ($10^{19}\mathrm{W/cm^2}$) has been helpful to the investigation of such problems in the laboratory. Various mechanisms of generating magnetic fields have been identified in the context of laser-solid interactions [54–57]. The production of large quasi-static magnetic fields has been observed in laser-produced plasma. Such magnetic fields are observed to exceed 100-200 kG in early experiments of a short laser pulse (100 ps) interacting with underdense plasma $n_e \simeq 0.2 n_c$ with target larger than $100\,\mu m$ in diameter [58]. These magnetic fields can only be observed when the target diameter is at least several times larger than the focal spot diameter. For laser pulse lengths longer than 1 ns, one obtains a larger-scale toroidal magnetic field surrounding the laser spot. One is then tempted to attribute these toroidal fields to the $\nabla n \times \nabla T$ mechanism [59], which is responsible for the Biermann battery, where a magnetic field can grow from a configuration that is initially perfectly current and charge neutral, as long as the plasma contains perpendicular temperature and density gradients. The Faraday rotation of a high frequency electromagnetic probe beam has been used to detect such magnetic fields [60].

The propagation of a short laser pulse in an overdense plasma has been widely studied [61]. It was found that high intensity laser pulses drive electrons in the forward direction. For such intense laser pulses, the electron velocity becomes relativistic and with its progress in the background plasma, a return electron current flows in the opposite direction to maintain the global charge and current neutrality. Plasma flows lead to anisotropic velocity distribution which is unstable to transverse electromagnetic perturbations and leads to the Weibel instability (WI) or the current filamentation instability (CFI).

The Weibel instability also appears in the coronal region, typically for densities below $10^{24}\mathrm{cm}^{-3}$ [62]. The evolution of the instability can be divided into two stages, In the linear stage, the fast MeV-beam electrons move into the target; the plasma electrons respond and a return current is set up compensating the micro-currents carried by the fast MeV-beam electrons. These currents induce the magnetic field that reinforces the initial disturbance. This instability generates electromagnetic fields, creating current filaments and the magnetic field amplification. The growth rate of the instability is given by $\Gamma \sim \omega_p^{-1}$ in the linear stage [63]. Later the magnetic field decays rapidly due to the fact that the electrons reach thermal equilibrium and the ions begin to respond to the instability. As a result, the Weibel instability ceases at a few $100\,\omega_p^{-1}$. The Weibel instability breaks the flow of particles into tiny dissipated magnetic field regions. At

this stage, the linear instability enters into the nonlinear dissipative stage and gets filamented. Theoretically, it has been predicted that the magnetic field saturates at $B_{sat} \propto \Gamma^2$ [64] and reaches a quasi-steady linear level with no or very slow decay on a time scale much longer than $100\omega_p^{-1}$. Both the analytical and numerical simulations reveal that these instabilities can play an important role in stopping the hot electrons in the core [65, 66]. Spontaneously generated magnetic fields by these plasma instabilities are an undesirable effect in FIS scenarios [67]. Due to these instabilities, it is a challenge to deposit energies of the order of 10 kJ in a small region of 20 μm radius near the compressed core. Hence, it is necessary to understand the consequence of these instabilities to design FI experiments. Several experiments have been conducted to inspect the role of the Weibel instability in different scenarios [68, 69].

1.7 Particle in cell simulations of plasma instabilities

The importance of plasma instabilities in generating strong magnetic fields as indicated by the synchrotron spectra has been widely recognized. In such instabilities, the dynamics occur at electron time scales and the free energy of the plasma particles are converted into magnetic energy. Thus, a kinetic approach is necessary to simulate such systems. The particle-in-cell (PIC) method is one such suitable technique. We have carried out multi-scale ab initio fully kinetic numerical simulations of plasmas instabilities using the PIC code OSIRIS [39, 40].

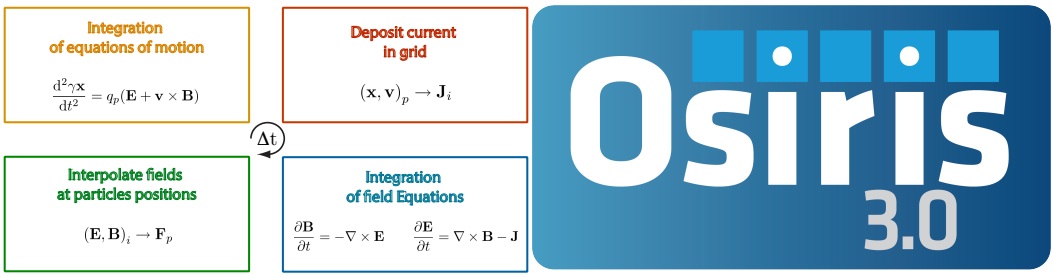

FIGURE 1.6: OSIRIS: fully relativistic, electromagnetic, massively object oriented particle-in-cell with a visualization and data analysis software package

OSIRIS is a fully relativistic, electromagnetic, massively object oriented particle-in-cell (PIC) code with a visualization and data analysis framework (Figure 1.6). The code has been developed for more than ten years by the Osiris consortium composed by University of California at Los Angeles and Instituto Superior Técnico [70, 71].

The full set of Maxwell's equations were solved on a grid using currents and charge

densities calculated by weighting discrete particles onto the grid. Each particle is pushed to a new position and momentum via self-consistently calculated fields. In order to advance the particles, the Boris pusher has been implemented [72]. The method is based on a multi-step process and is second-order accurate in time. The rotational operator is replaced by a finite difference approximation on the grid and fields and current are defined on shifted meshes for achieving a second-order accuracy. The integration in time follows a second order accuracy scheme. A charge-conserving current deposition algorithm has been enforced [73].

The code is written in Fortran 90 in an object-oriented way. The parallelization of the code is done for distributed memory system and it is based on the Message Passing Interface (MPI) paradigm [74]. The parallelization is based on a domain decomposition across the available nodes. The output data are saved in the HDF format, a standard, platform independent and self-contained file format. Simulation result visualization is performed with visXD, a custom designed set of IDL (Interactive Data Language) based tools [75].

1.8 ORIGINAL CONTRIBUTIONS

The primary goal of this thesis is to demonstrate the role of electromagnetic instabilities generating magnetic fields in plasmas, which has been recognized in the context of the inertial confined fusion (ICF) schemes, as well as in the study of gamma-ray-bursts (GRBs). By using first principles kinetic simulations, we identify and establish those conditions, which will also allow to produce and test these astrophysical conditions in laboratory plasmas. Each Chapter of this Thesis corresponds to at least one paper, published or in preparation for publication. The thesis is organized in the following fashion:

Chapter 2 discusses the basic theory beam-plasma interactions, followed by a detailed discussion of the longitudinal to transverse instabilities. We discussed the dominant mechanisms, i.e WI/CFI of magnetic field generation relevant to this thesis.

The physics associated with a realistic condition of the propagation of Ultra-relativistic e^-, e^+ fireball beam or neutral plasma mimicking a realistic plasma shell, with static plasma consisting of e^-, p^+ is studied in **Chapter 3**. Systematic numerical investigation of the multi-dimensional dynamics of the fireball expansion using different fireball densities, temperatures, velocities and dimensions are investigated. The investigation is focused on the propagation of short vs longer fireball beams, i.e. beams that are shorter vs longer than the plasma wavelength, and on the propagation of long beams, i.e. beams that are much longer than the plasma wavelength. The main goal of this part of the work is to find ideal conditions for the amplification of magnetic fields, and modeling of possible experimental set-ups. In addition, we extend

the studies of non-neutral e^-, e^+ beam propagation into plasma.

In **Chapter 4**, we studied the interaction of two dark electromagnetism electron-positron (e^-, e^+) like plasmas. Assuming the electromagnetic interaction to be a fundamental interactions in dark matter, the studies of electromagnetic instabilities in interpenetrating plasma flows can be extended to collision of dark clouds. The instabilities can lead to slowdown of the bulk flow. These studies can help us understand the distribution of the dark matter in space. We established a strong upper bound on the strength of the dark electromagnetic like self-interaction.

Chapter 5 discusses the self generated magnetic field in laser matter interactions. *Ab initio* particle-in-cell simulations of the interaction of short ($\leq ps$) intense ($a_0 \geq 1$) laser-pulses with over-dense plasma targets show observable Weibel generated magnetic fields. This field strength surpasses that of the Biermann battery, usually dominant in experiments, as long as the gradient scale length is much larger than the local electron inertial length; this is achievable by carefully setting of the appropriate gradients in the front of the target e.g. via pump-probe configurations.

Finally, **Chapter 6** summarizes the thesis and discusses possible future research directions.

The work developed in this Thesis has led to the following scientific publications:

1. Generation of neutral and high-density electron-positron pair plasmas in the laboratory, G Sarri, K. Poder, J. M. Cole, W. Schumaker, A. Di Piazza, B. Reville, T. Dzelzainis, D. Doria, L. A. Gizzi, G. Grittani, S. Kar, C. H. Keitel, K. Krushelnick, S. Kuschel, S. P. D. Mangles, Z. Najmudin, N. Shukla, L. O. Silva, D. Symes, A. G. R. Thomas, M. Vargas, J. Vieira, and M. Zepf, Nature communications **6** (2015).

2. Condition for the onset of the current filamentation instability of ultra-relativistic fireball bunches in plasmas, N. Shukla, J. Vieira, P. Muggli, G. Sarri, R. A. Fonseca, L. O. Silva, Journal of Plasma Physics **84** (2018).

3. Ultra-relativistic fireball beam interaction with plasma, P. Muggli, S. F. Martins, N. Shukla, J. Vieira, L. O. Silva, arXiv e-prints (2013), arXiv:1306.4380.

4. A (Nearly) Weaker-than-Gravity bound on long range dark mater interactions, N. Shukla, K. Schoeffler, J.Vieira, R. A. Fonseca, L. O. Silva, J. Mardon, and B. Feldstein, in preparation to Physical Review D (2019).

5. Weibel magnetic field competes with Biermann field in laser-solid interactions, N. Shukla, K. Schoeffler, E. Boella, J.Vieira, R. A. Fonseca, L. O. Silva, in preparation to Physical Review Letters (2019).

CHAPTER 2

PHYSICS OF RELATIVISTIC CHARGED PARTICLE BEAM PROPAGATION

2.1 OVERVIEW

In early 1960, an intense particle beam with power levels up to 10^{13}W was produced using Marx generator technology for time durations of the order of 10-100 nsec. Since then, there have been rapid advances in pulse technology at a number of major laboratories around the world. For example, experiments at SLAC laboratory are capable of driving charged beams with 10^{10} particles per pulse with 120 Hz repetition rate up to an energy of 50 GeV. Much of the research interest in using the interaction of such intense beam with plasmas is to investigate particle acceleration via Plasma Wakefield Acceleration (PWFA) [76–78] and to generate magnetic field via plasma instabilities in order to probe the phenomenon in the laboratory, this explaining energetic phenomena in astrophysical objects [79, 80].

In the following section, the basic physics of propagation of intense relativistic charged particle beams into the vacuum and through a plasma is briefly addressed from a theoretical point of view [9, 41]. Results of this section will help to understand the microphysical plasma processes that have been explored by the means of first principal kinetic simulations for different regimes.

2.1.1 CONCEPT OF PROPAGATING A CHARGE PARTICLE BEAM IN VACUUM

A charged particle beam is a bundle of moving particles such that the trajectories generally make a small angle with the axis of propagation. The dynamics of charged

particles is subjected to self-electric and magnetic fields which obey Maxwell's equations

$$\nabla \cdot \mathbf{E} = 4\pi\rho \tag{2.1a}$$

$$\nabla \times \mathbf{E} = -\frac{1}{c}\frac{\partial \mathbf{B}}{\partial t} \tag{2.1b}$$

$$\nabla \cdot \mathbf{B} = 0 \tag{2.1c}$$

$$\nabla \times \mathbf{B} = \frac{4\pi}{c}\mathbf{J} + \frac{\mathbf{1}}{\mathbf{c}}\frac{\partial \mathbf{E}}{\partial \mathbf{t}} \tag{2.1d}$$

where E, B are the electric and the magnetic field and $\rho = |q|n$ and $\mathbf{J} = |q|n\ \mathbf{v}$ are the charge and current densities of the beam, which satisfy the continuity equation

$$\frac{d\rho}{dt} + \nabla \cdot \mathbf{J} = \mathbf{0} \tag{2.2}$$

The force on a point charge q (e^-, e^+) and velocity $\mathbf{v}$ in an electromagnetic field is defined by Lorentz force

$$\frac{d\mathbf{P}}{dt} = |q|\left(\mathbf{E} + \frac{\mathbf{v} \times \mathbf{B}}{\mathbf{c}}\right) \tag{2.3}$$

where $\mathbf{P} = \gamma m\mathbf{v}$ is the relativistic momentum with $\gamma = 1/(1-\beta^2)^{1/2}$, known as Lorentz factor and $\beta = |\mathbf{v}|/\mathbf{c}$.

To explore the key aspects of the beam dynamic, a cylindrically symmetric beam around the propagation z-direction is assumed. The velocity is decomposed into longitudinal and transverse components

$$\mathbf{v} = v_r\hat{e_r} + v_\theta\hat{e_\theta} + v_z\hat{e_z} \tag{2.4}$$

For a monochromatic relativistic beam, it is assumed that the transverse random motion is smaller than the longitudinal motion $|v_r|, v_\theta \ll v_z$. This assumption is known as the paraxial approximation and it entails that the particles only slightly deviate from their axis. The beam emittance is therefore neglected. Hence, the perpendicular components of the equation of motion are given by:

$$\frac{d(\gamma m\mathbf{v}_\perp)}{dt} = q\left(\mathbf{E}_\perp + \frac{(\mathbf{v} \times \mathbf{B})_\perp}{\mathbf{c}}\right) \tag{2.5}$$

An intense beam in the absence of external fields propagating in vacuum evolves in its self-fields. The radial electric force due to the beam space charge always dominates the self-magnetic pinching force. By transforming to a reference frame with the beam, the magnetic field can be transformed away however the radial electric field does not

change sign. Therefore, it requires a degree of space charge neutralization for the existence of a radial force equilibrium.

Let's consider a cylindrically symmetric electron beam with velocity $v_e = \beta c$ and density n_e propagating in a stationary ion background of density n_i. The radial force F_r on a test electron can computed as:

$$F_r = -e\left(E_r - \beta B_\theta\right) \tag{2.6}$$

From Gauss' law and Ampere's law, E_r and B_θ can be estimated as:

$$E_r = -\frac{4\pi e}{r}\int n_e\left(1 - f_e\right) r dr \tag{2.7}$$

$$B_\theta = -\frac{4\pi e}{r}\int \beta n_e r dr \tag{2.8}$$

where $f_e = n_i/n_e$ is fractional electron space charge neutralization. Substitution of Eqs. (2.8, 2.7) into Eq. (2.6), the radial force yields

$$F_r = \frac{4\pi e^2}{r}\int \left(1 - f_e - \beta^2\right) n_e r dr \tag{2.9}$$

If $f_e = 0$, the beam is unneutralized, the force is radially outward and beam expands (since $1 - \beta^2 > 0$). Therefore, $f_e = 1 - \beta^2 = \gamma_b^{-2}$ is required for $F_r = 0$.

The neutralization of a high intensity relativistic electron beam can also be achieved by using a strong longitudinal magnetic field. However, ion beams require the strength of such a field to be too high to be practical. Although the required magnetic field is feasible for the stability of beam propagation, there still exists a limit to the amount of current that can propagate. It can transport current only up to a maximum value, called Alfvén current limit [81]. This is because currents larger than the *Alfvén current* I_A generate a magnetic field large enough that the Larmour radius of the electrons becomes smaller than the beam radius. As a consequence, the beam is not further transported in the beam direction. For relativistic beams the *Alfvén current* I_A limit is

$$I_A = \beta\gamma\frac{4\pi mc}{q\mu_0} = \frac{qc\beta\gamma}{r_b} \approx 17000\beta\gamma A \tag{2.10}$$

where r_b is the electron classical radius. This fundamental current limit was first derived in 1939 by H. Alfvén [81], who studied the propagation of electrons through a plasma in space. A more detailed description of the beam equilibrium configurations is discussed in [81, 82].

2.1.2 PROPAGATION OF A CHARGED PARTICLE IN A PLASMA

The situation changes when an intense beam passes through a background plasma because the displacement of plasma charges tends to neutralize the beam self-fields. During the beam injection, the background plasma electrons move out of the beam region during the characteristic time $(4\pi\sigma/c)^{-1}$, which is typically quite short (10^{-9} sec). The net space charge effects are quite minimal which does not pose a serious limitation to beam transport in plasma. However, the azimuthal self-magnetic fields of the beam cause a further limitation on the beam transport in plasma. Hence, the Alfvén limit is modified and corresponds to the charge and current neutralization fractions [83]

$$E_r = 2\pi e n_0 r_b (1 - f_e), B_\theta = 2\pi e n_0 r_b \beta_0 (1 - f_m) \tag{2.11}$$

where f_e and f_m are the fractional electric and magnetic neutralization due to the counter-streaming plasma current. When $f_e = 1$ the beam is fully neutralized and, as a consequence of the self-focusing forces, it pinches. When $f_m = 1$ no net fields act on the beam particles which propagates following linear trajectories. Therefore, if $f_e = f_m = f$, the force experienced by the charged particle beams becomes:

$$F_b = -e(E_{br} + v_b \times B_\theta)(1 - f) \propto \frac{1}{\gamma^2}(-eE_{br})(1 - f) \tag{2.12}$$

where v_b is the beam velocity and γ_b is the Lorentz factor. Hence, beams defocuse at a rate $\propto 1/\gamma_b^2$, which is known as Bennett pinch [83]. Therefore, for a highly relativistic beam the defocusing force is sufficiently small. As a consequence, the electric field produced by a relativistic beam compensates almost the self produced magnetic field.

The neutralization of a high intensity relativistic electron beam can also be achieved in the presence of stationary ions with mass m_i. When the beam propagates in the presence of a background plasma, it creates a current imbalanced in the system which is reduced or eliminated by the plasma ions. Therefore, the total current density is $J_b + J_p = 0$, $J_b = -en_b v_b$ and $J_p = Z_i e n_i v_i$. As a consequence, it reduces the defocusing forces [84]:

$$F_b = -e((E_{br} - E_{pr}) + v_b \times (B_{b\theta} - B_{p\theta})) \tag{2.13}$$

where E_{br}, E_{pr} and $B_{b\theta}, B_{p\theta}$ are the self electromagnetic fields of the electrons and plasmas, respectively.

An intense relativistic charged particle beam containing a uniform current density with no emittance can propagate long distances without expansion in the plasma. Even in this area, there are two distinct regimes for beam-plasma interactions depending on the ratio between the transverse size of the beam (σ_r) and the collisionless skin depth (c/ω_p) of the plasma:

- **Plasma focusing regime:** In this regime, the transverse beam size is smaller than the plasma skin depth ($\sigma_r \ll c/\omega_p$ or $k_p\sigma_r < 1$). A relativistic electron beam propagating into a neutral plasma pushes away the electrons via electrostatic repulsive forces. The plasma ions remain immobile because of their high mass. The majority of the plasma return current flows outside of the beam. Thus, $J_b > J_p$ and $n_p/n_p < 1$ lead to $B_{b\theta} > B_{p\theta}$. Therefore, the net magnetic fields $|B_{b\theta} - B_{p\theta}| > 0$ and the background plasma ion Coulomb attractive forces focus the beam reducing the size of the radial beam size σ_r. In the linear regime, the focusing forces scale with the beam density, $F_b \propto n_b$. Thus, the beam generates longitudinal and transverse wake fields. This process is at the base of the mechanism for accelerating electrons called PWFA, which can accelerates electrons to GeV in few centimeters, thus constituting *de facto* a table top accelerator [85–87].

- **Return current regime:** When a highly relativistic beam enters a plasma, it displaces the plasma particles, driving a return current. If the transverse beam size is larger than the plasma skin depth ($\sigma_r \geq c/\omega_p$ or $k_p\sigma_r > 1$), the current flows through the beam. In this case, the net magnetic field $|B_{b\theta} - B_{p\theta}| = 0$. The beam is subject only to the net electric field. Even though the system is not fully neutral, this significantly reduces the focusing force. One of the key problems in the beam propagation in this case is its stability. As the beam interacts with the plasma it can drive several plasma instabilities. In addition, the growing mode is amplified and damped during the propagation. Depending on the density, bulk velocity and emittance of the beam, parallel and transverse modes can be generated [88–91].

2.1.3 Effect of emittance

So far the analysis has been limited to beams with zero emittance. A realistic beam contains finite emittance. The beam emittance is related to the area of the beam in the transverse $x_\perp, p_\perp$ phasespace and it constitutes also a measurement of its divergence. The normalized transverse phase-space emittance is defined as:

$$\hat{\epsilon}_x = \frac{< p_z >}{\hat{\epsilon}} \sqrt{< x^2 >< x'^2 > - < xx' >^2} \tag{2.14}$$

where x is the transverse particle position measured from the beam axis. In addition, $\sqrt{< x^2 >}$, $\sqrt{< x'^2 >}$ and $\sqrt{< x^2x'^2 >}$ are the rms beam size, angular spread and correlation between x and x', respectively. The normalized transverse phase-space emittance is expressed as [92, 93]:

$$\epsilon_n = \frac{1}{m_e c} \sqrt{< x^2 >< p_x^2 > - < xp_x >^2} \tag{2.15}$$

where is $p_x = v_x \gamma m_e c$. If we neglect the terms $< xp_x >^2$, then

$$\tilde{\epsilon}_x = \tilde{x}\tilde{x'}_{th} = \tilde{x}\frac{\tilde{v}_{x,th}}{v_0} \tag{2.16}$$

where $\tilde{x} = \sqrt{x^2}$ is the transverse beam size and $\tilde{v}_{x,th} =< x'^2 >= p_x/p_z$ is the beam divergence. The spread in momentum, or velocity, increases the emittance, which tends to bend the beam spread apart. It is possible to relate the transverse beam energy spread with its effective temperature :

$$\frac{1}{2}m_e\tilde{v}^2_{x,th} = 2\frac{1}{2}k_B T_\perp \tag{2.17}$$

where k_B and $T_{e\perp}$ are the Boltzman's constant and the transverse beam temperature. The beam emittance is an initial condition for the particles velocity and it leads to the defocusing of the beam.

2.2 BEAM-PLASMA INSTABILITIES

The propagation of an intense particle beam into a plasma is subjected to a variety of plasma instabilities [94]. These instabilities are excited and amplified by the kinetic energy of the beam, which represents substantially a source of free energy. The studies concerning beam plasma instabilities are usually carried out by using standard perturbation techniques. If the system is unstable, an initial perturbation increases with time, causing a rapid growth of the electromagnetic field until the plasma reaches again an equilibrium state. In the following section, a general description of collective processes of intense charge particle beams interactions with plasma are provided by resorting to plasma kinetic theory.

2.2.1 KINETIC DESCRIPTION OF A RELATIVISTIC COLLISIONLESS PLASMA

In kinetic theory, a closed set of linearized Vlasov and Maxwell equations are used to derive a linear dispersion for beam-plasma interactions. Here, a relativistic, homogeneous and spatially infinite collisionless plasma is considered. Initially, the system is charge and current neutral (i.e $\sum_j q_j n_j^{(0)} = 0, \sum_j q_j n_j^{(0)} \mathbf{v}_j^{(0)} = 0$, where $\mathbf{v}_j^{(0)}$ is velocity of the species). External magnetic or electric fields are not considered. The initial perturbation for **E** and **B** is assumed to be small enough, such that the linear approximation remains valid. Each plasma species obeys an initial momentum distribution $f_j^{(0)}(\mathbf{p})$ normalized to unity in the momentum space ($\int f_j^{(0)}(\mathbf{p})d\mathbf{p} = n_j^{(0)}$). The linearized Vlasov equation for the total j_{th} distribution function is $f = f_j^{(0)}(\mathbf{p}) + f_j^{(1)}(\mathbf{p})$. The following closed set of equations is required to derive the linear dispersion relation and to determine the complete dynamics of the plasma:

$$\frac{\partial f_j}{\partial t} + \mathbf{v_j} \cdot \nabla_{\mathbf{r}} f_j + q_j \left(\mathbf{E} + \mathbf{v_j} \times \mathbf{B}\right) \cdot \nabla_{\mathbf{p}} f_j = 0, \tag{2.18}$$

$$\rho(x,t) = \sum_j q_j n_j = \sum_j q_j \int d\,\mathbf{p} f_j(x,p,t), \tag{2.19}$$

$$\mathbf{J}(x,t) = \sum_j q_j n_j v_j \sum_j q_j \int d\,\mathbf{p}\,\mathbf{v_j} f_j(x,p,t), \tag{2.20}$$

where $\mathbf{v_j}$ $(p_j/m_j\gamma)$ and $\gamma = \sqrt{1+|p|^2/(m_j c)^2}$ are the relativistic velocity and the Lorentz factor. In order to derive the electromagnetic dispersion relation, the system includes Faraday's (2.1b) and Ampere's laws (2.1d). There is no collision, hence the particles do not interact directly with each other instead interacts via electromagnetic fields.

2.2.2 THE LINEARIZED VLASOV-MAXWELL MODEL

The above system of equations has been linearized and perturbations $\propto \exp(i\mathbf{k} \cdot \mathbf{x} - i\omega t)$, such that $\partial/\partial t \rightarrow -i\omega$, $\partial/\partial x \rightarrow -i\,\mathbf{k}$ have been considered. The Vlasov equation becomes:

$$-i\omega f_j^{(1)} + i\mathbf{v} \cdot \mathbf{k} f^{(1)} + q_j \left(\mathbf{E}^{(1)} + \mathbf{v_j} \times \mathbf{B}^{(1)}\right) \cdot \nabla_{\mathbf{p}} f_j^{(0)} = 0, \tag{2.21}$$

$$f_j^{(1)} = \frac{i q_j}{m_j(\mathbf{k} \cdot \mathbf{v} - \omega)} \left(\mathbf{E}^{(1)} + \mathbf{v_j} \times \mathbf{B}^{(1)}\right) \cdot \nabla_{\mathbf{p}} f_j^{(0)}, \tag{2.22}$$

which results the density current $\mathbf{J}^{(1)} = \sum_j q_j \int d\,\mathbf{p}\,\mathbf{v} f^{(1)_j}$ and the linearized Maxwell-Faraday's and Maxwell-Ampere's equations,

$$i\mathbf{k} \times \mathbf{E}^{(1)} = i\frac{\omega}{c}\mathbf{B}^{(1)}, \tag{2.23}$$

$$i\mathbf{k} \times \mathbf{B}^{(1)} = -i\frac{\omega}{c}\mathbf{E}^{(1)} + \frac{4\pi}{c}\mathbf{J}^{(1)}, \tag{2.24}$$

By combining Eq. (2.23) and (2.24), the following expression is found

$$\mathbf{k} \times \mathbf{k} \times \mathbf{E}^{(1)} + \frac{\omega^2}{c^2}\left(\mathbf{E}^{(1)} + \frac{4\pi}{\omega}\mathbf{J_1}\right) = 0, \tag{2.25}$$

which can be rewritten as

$$\mathbb{T}(\mathbf{k},\omega)\cdot\mathbf{E}^{(1)}=0, \tag{2.26}$$

with

$$\mathbb{T}(\mathbf{k},\omega)=\frac{\omega^2}{c^2}\epsilon(\mathbf{k},\omega)+\mathbf{k}\otimes\mathbf{k}-k^2\mathbf{I} \tag{2.27}$$

where $\otimes$ denotes tensor product, and the dielectric tensor is given by

$$\epsilon_{\alpha\beta}(\mathbf{k},\omega)=\delta_{\alpha\beta}+\sum_j\frac{\omega_{pj}^2}{\omega^2}\int d\mathbf{p}\frac{p_\alpha}{\gamma}\cdot\frac{\partial f_j^{(0)}}{\partial p_\beta}+\sum_j\frac{\omega_{pj}^2}{\omega^2}\int d\mathbf{p}\frac{p_\alpha p_\beta}{\gamma}\frac{\mathbf{k}\cdot\partial f_j^{(0)}/\partial p}{m\omega\gamma-\mathbf{k}\cdot\mathbf{p}} \tag{2.28}$$

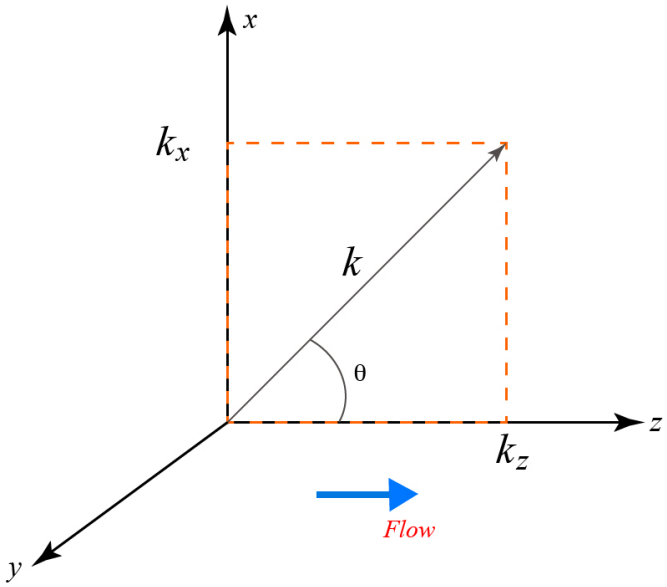

FIGURE 2.1: Axis conventions adopted in this chapter considering the wavevector $\vec{k}$ lies in the (x, z) plane

Equation (2.27) has non-zero solutions if and only if det $|\mathbb{T}|=0$. This allows for finding one or more ω's, $(\omega_{1,k},...,\omega_{n,k}\in\mathbb{C}^N)$ as a function of $\mathbf{k}$, known as the dispersion relation. Each couple $(\mathbf{k},\omega_{j,k})$ defines a proper mode of the system and the unstable modes are those with $\mathrm{Im}(\omega)>0$. Without loss of generality, the wave vector of the perturbation can be preferably considered in the plane $\mathbf{k}=(k_x,0,k_z)$ as shown in Figure 2.1 and that f is an even function of p_x,p_y. Hence, all off diagonal terms $(\epsilon_{xy}=\epsilon_{yz})$ are zeros except ϵ_{xz}. The final form of the tensor $\mathbb{T}$ then reads:

$$\mathbb{T}=\begin{vmatrix}\frac{\omega^2}{c^2}\epsilon_{xx}-k_z^2 & 0 & \frac{\omega^2}{c^2}\epsilon_{zx}+k_xk_z\\ 0 & \frac{\omega^2}{c^2}\epsilon_{yy}-k^2 & 0\\ \frac{\omega^2}{c^2}\epsilon_{xz}+k_xk_z & 0 & \frac{\omega^2}{c^2}\epsilon_{zz}-k_x^2\end{vmatrix} \tag{2.29}$$

The dispersion relation is solved looking for ω looking for roots with positive imaginary part, which corresponds to growing unstable modes depending on the orientation of the wave vector and any orientation of the electromagnetic field with respect to the wave vector.

2.3 A MULTIDIMENSIONAL UNSTABLE SPECTRUM

There has been considerable theoretical progress in studying multidimensional beam-plasma instabilities in the relativistic and non-relativistic regime. In 1925, Langmuir first suggested the existence of oscillations in beam-plasma systems, which was demonstrated by Pierce in 1948 showing unstable oscillations that arise within such systems. In 1949, Bohm and Gross discovered unstable perturbation along the beam direction using a kinetic approach, known as the electron two-stream electrostatic instability (TSI). Later on, Weibel [30] and Fried [95] showed that the beam-plasma system can also be unstable against electromagnetic modulations, also known as the Weibel/Current Filamentation (WI/CFI) electromagnetic instability. Bludman et al. [96] suggested a third type of instability, which is unstable against arbitrary k with respect to the flow, known as the Oblique instability (OBI). There are many possible ways to excite these modes in laboratory such as intense charge particle beam-plasma interactions or two counterpropagating plasma flows, due to laser-plasma interaction. Because of their large presence and importance, the most common configuration of two counter-propagating neutral plasmas is considered. A whole class of instabilities potentially could develop in this configuration [94].

Two identical components of an unmagnetized plasma composed of relativistic electrons and positrons are considered. The beam is homogeneously infinitly long ($\gg c/\omega_p$). Initially the beams are current and charge neutral. Therefore, the equilibrium velocity and the number density are $v_{e1}^{(0)} = v_{p1}^{(0)} \equiv v_1^{(0)}, v_{e2}^{(0)} = v_{p2}^{(0)} \equiv -v_2^{(0)}$ and $n_{e1}^{(0)} = n_{p1}^{(0)} \equiv n_1^{(0)}, n_{e2}^{(0)} = n_{p2}^{(0)} \equiv -n_2^{(0)}$, respectively. We indicate each of them with j_a, where j specifies the charge of the species and a specifies the beam to which it belongs. At equilibrium, we have

$$\mathbf{J}(\epsilon) = \mathbf{J}_{Beam1}(\epsilon) + \mathbf{J}_{Beam2}(\epsilon) \tag{2.30}$$

In this configuration, the interpenetration between two neutral plasma beams could in principle induce several instabilities, involving transverse and parallel modes, that allows small field perturbations to grow exponentially. The full unstable wavenumber k spectrum has been intensively studied in the cold plasma limit. Bi-Maxwellian, waterbag, Maxwell-J*ü*ttner and kappa distribution functions are the most commanly used beam distribution functions to derive the linear dispersion relation for longitudinal, oblique and transverse instability [94]. Since it is cumbersome to analyze the

coupling between the electrostatic and electromagnetic modes, significant progress has been made by considering the electrostatic and electromagnetic modes separately. In order to derive the dispersion relation of TSI/WI/CFI/OBI, an initial cold distribution function for each species is considered:

$$f_{ja}^{(0)} = \delta(p_x)\delta(p_y)\delta(p_z - p_{ja}) \tag{2.31}$$

Eq. (2.29) exhibits two main branches.

— First branch shows the well-known dispersion relation of the electromagnetic waves propagating ($k \perp E$) in a plasma:

$$\omega^2\epsilon_{yy} - k^2c^2 = 0, \tag{2.32}$$

$$\omega^2 + k^2c^2 - \sum_{p,ja} \frac{\omega_{p,ja}^2}{\gamma_{ja}} = 0 \tag{2.33}$$

where $\omega_{p,ja} = \sum_{p,ja} \sqrt{4\pi e^2 n_{ja}/m_e}$ is the electron plasma frequency, e the elementary charge, m_e the electron mass and ω and k the wave frequency and wavenumber respectively.

— The second branch defines mixed modes (longitudinal, transverse or more general Oblique) with electric field the associated in the (x, z) plane:

$$(\omega^2\epsilon_{xx} - k_z^2c^2)(\omega^2\epsilon_{zz} - k_x^2c^2) - (\omega^2\epsilon_{xz} - k_xk_zc^2)^2 = 0, \tag{2.34}$$

The analysis of this dispersion relation gives unstable growing modes. In next sub-sections, we distinguish three major types of instabilities (TSI, WI/CFI, OBI), separately.

2.3.1 Purely longitudinal instability: Two-stream Instability (TSI)

Eq. (2.34), for the wave vector parallel to the beam flow, $k_x = 0$, the off-diagonal terms ϵ_{xz} vanishes, giving rise to:

$$(\omega^2\epsilon_{xx} - k_z^2c^2)\omega^2\epsilon_{zz} = 0, \tag{2.35}$$

The dispersion relation for the purely two-stream instability is obtained for $\epsilon_{zz} = 0$ (see Appendix A):

$$D(k,\omega) = 1 - \frac{\omega_{p,ja}^2}{2}\left[\frac{1}{\gamma_1^3(\omega - kv_1^{(0)})^2} + \frac{1}{\gamma_2^3(\omega + kv_2^{(0)})^2}\right] \tag{2.36}$$

When two plasma beams propagate against each other, a density perturbation on one beam is reinforced by the force due to bunching off the particles in the other stream and vice versa. As a consequence, the beam velocity is higher than the phase speed of plasma waves $v_b > \omega_{pe}/k$. Hence, the instability is being seeded by spatial inhomogeneities, in which electrons are bunched together, and their energy is transformed into the energy of plasma waves. The perturbation grows exponentially in time driving purely longitudinal electric fields. The instability stops growing when all the free energy of the beams is converted into field energy. At saturation, the beams thermalize and a hot plasma is formed.

2.3.2 TRANSVERSE ELECTROMAGNETIC INSTABILITY

Now, if we consider wave vectors normal to the flow, i.e. $k_z = 0$, we obtain the following dispersion relation

$$\epsilon_{xx}(\omega^2\epsilon_{zz} - k_x^2c^2) - \omega^2\epsilon_{xz}^2 = 0, \tag{2.37}$$

The unstable solutions of this dispersion relation have an electric field that, in general, lies in the (x, z) plane. The collection of these modes represents the instability called filamentation instability. Generally, the filamentation instability is not considered to be a purely transverse mode i.e it has a finite electrostatic component [97]. However, when the beam and return current are perfectly symmetric (i.e with same density, drift energies and temperature), there is no space charge separation, $\epsilon_{xz} = 0$, leading to the purely transverse mode. Thus, we can recover the dispersion relation of purely "transverse" filamentation instability.

$$\epsilon_{zz} - k_x^2c^2/\omega^2 = 0, \tag{2.38}$$

In the literature, two classes of purely transverse electromagnetic instabilities are reported, i.e the Weibel (WI) [30] and the Current Filamentation instability (CFI) [95]. Even though, these two instabilities are quite similar in nature driving a purely transverse mode, but there is a difference how these instabilities are generated in the first place. The Weibel instability is generated due to temperature anisotropy in a homogeneous collisionless plasma. However, the CFI is strictly driven due to counterpropagating beams (see Fig 2.2). During the past few decades, the WI and CFI have been thoroughly studied both theoretically and as well experimentally [94,98]. In following section, we briefly explain the basic mechanisms of WI and CFI.

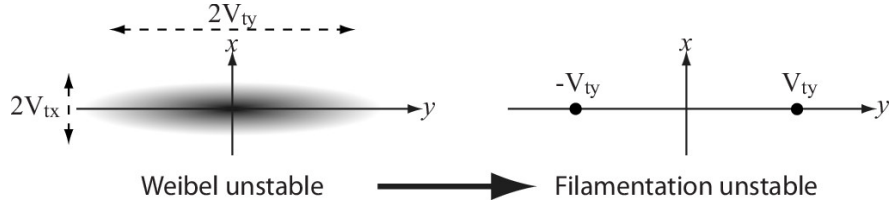

FIGURE 2.2: (From Bret et al. [94]) Illustration of typical distribution functions subject to the Weibel and the filamentation instabilities. An anisotropic Weibel-unstable hot plasma can be approximated by a cold filamentation-unstable two-beam system.

WEIBEL INSTABILITY

The Weibel instability [30] is considered to be the most important for a purely growing electromagnetic mode in an anisotropic plasma (for full derivation see Appendix B). In his seminal paper [30], Weibel found that an anisotropic plasma having a directional dependence of the temperature is unstable against a magnetic field perturbation. Transverse modes are amplified in a collisionless plasma even in the absence of an external magnetic field. The free energy is stored in the electron temperature anisotropy, which causes a purely growing magnetic field. Ions is assumed to be immobile. The dispersion relation in an unmagnetized plasma was derived by using a closed set of linearized Vlasov-Maxwell equations, given by

$$\omega^2 - k^2c^2 - \int_0^\infty \int_{-\infty}^\infty \left(\frac{\partial f_0}{\partial v_0} - \frac{v_0 k}{(\omega + k v_z)} \frac{\partial f_0}{\partial v_z} \right) v_0^2 \, dv_0 \, dv_z = 0, \tag{2.39}$$

where $f_0(v)$ is an anisotropic distribution functions for the electrons, with $v_0^2 = v_x^2 + v_y^2$. The wave vector $\mathbf{k}$ is parallel to the z-direction, and a bi-Maxwellian distribution function (temperature anisotropy $(v_0/v_z)^2 - 1 > 0$) was chosen to solve Eq. (2.39) and determine the growth rate Γ of a purely growing electromangetic growing wave. The distribution function is thus given by:

$$f_0 = \frac{n_0}{v_0^2 v_z (2\pi)^{3/2}} exp\left(-\frac{v_0^2}{2u_0^2} - \frac{v_z^2}{2u_z^2} \right), \tag{2.40}$$

where u_0 and u_z are the intial thermal velocities in the direction of v_0 and v_z, respectively. The dispersion, in the limit $\omega/kv_z \gg 1$, reads

$$\omega^4 - (\omega^2 + k^2c^2)\omega^2 - k^2 u_0^2 \omega_{pe}^2 = 0, \tag{2.41}$$

where ω is the frequency of the unstable wave.The solution of the biquadratic Eq. (2.41) is

$$\omega = \pm \left(\frac{1}{2} [(\omega_{pe}^2 + k^2 c^2) \pm ((\omega_{pe}^2 + k^2 c^2)^2 + 4k^2 u_0 \omega_{pe}^2)^{1/2}] \right)^{1/2}. \tag{2.42}$$

The negative imaginary solution of the above equation shows the growth rate of self-excited waves. In the limit $ku_z/\omega \ll 1$ (and thus $u_0 \gg u_z$) is

$$\omega \simeq i \frac{k u_0 \omega_{pe}}{(\omega_{pe}^2 + k^2 c^2)^{1/2}}, \tag{2.43}$$

Hence, a large electron temperature anisotropy drives the instability with a higher growth rate. The saturation of the Weibel instability is magnetic trapping of particles in filaments [99]. When the magnetic field reaches the value

$$B_{sat} = \frac{\gamma_i^2 \Gamma_{i0}^2 m_i}{k u_{i0} e_i} \tag{2.44}$$

When the magnetic fields are so strong that the Larmor radius becomes smaller than the thickness of the filaments, particles entering the filament will move in closed orbits. The particles cannot overcome the magnetic potential and are trapped.

CURRENT FILAMENTATION INSTABILITY

The physical picture of the Weibel instability in the presence of counterstreaming electron beams in plasmas was given by B. D. Fried [95]. To understand the physical mechanism of the Weibel instability, let us consider a system of counterstreaming electrons moving parallel and anti-parallel to the x-axis (see Fig. 2.3). We also assume some initial perturbation in the magnetic field $\mathbf{B} = \hat{\mathbf{z}} B_z \cos(ky)$, which is polarized along the z-axis and propagating along the propagating along the y-axis, arising from noise. As electrons move, they experience the Lorentz force $\propto (-e(v/c) \times \mathrm{B})$. The electrons are deflected by the magnetic field and micro-currents, in turn, enhance the initial magnetic fluctuation due to the Lorentz force. The growth rate for the Weibel instability in the presence of two-components of non-relativistic electrons streaming (with the speed v_e) relative to each other is

$$\Gamma_{max} = \frac{\omega_{pe} v_e}{c}, \tag{2.45}$$

The magnetic field generated by the instability always lies in the plane perpendicular to the bulk electron motion. The case of the Current filamentation instability with the ultra-relativistic electron streams (viz., $v_e/c \sim 1$) was investigated by Yoon and Davidson (derivation see Appendix B) who obtained the maximum growth rate as

$$\Gamma_{max} = \frac{\omega_{pe}}{\gamma^{1/2}}, \tag{2.46}$$

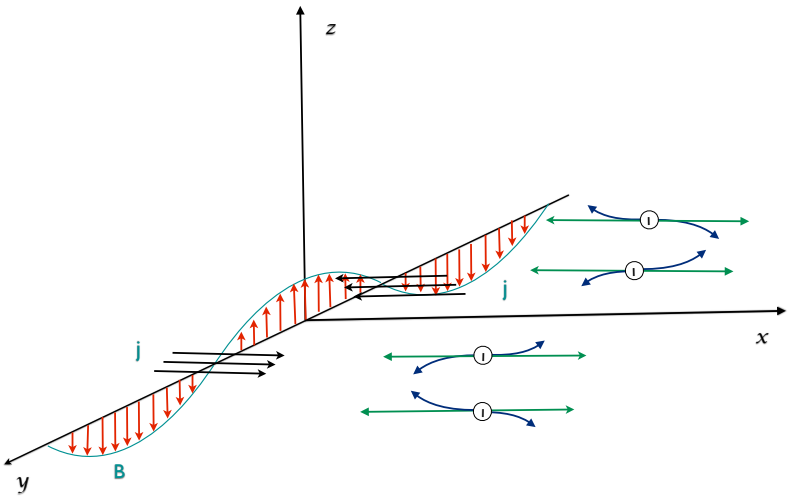

FIGURE 2.3: Physical mechanism of the Weibel instability: counter-propagation of two electron beams [41].

where $\gamma = (1 - v_e^2/c^2)^{-1/2}$ is the relativistic gamma factor. The instability generates a transverse magnetic field.

The Weibel plasma instability has a wide range of relevance in astrophysical plasmas, such as gamma ray burst sources, supernovae and galactic cosmic environments. The Weibel instability has been extensively studied in both the relativistic and nonrelativistic regimes [30, 41, 67, 94, 95] .

2.3.3 OBLIQUE INSTABILITY

In an ultra-relativistic dilute electron beams propagating through a cold plasma, the oblique instability grows faster than CFI/WI. The modes of the instability lie in the plane perpendicular or in between the longitudinal k_x and transverse k_z plane. The modes were first investigated in the fluid approximation [96]. There are two distinct regimes i.e cold plasma limit or hydrodynamic (reactive limit) and kinetic regime.

HYDRODYNAMIC (REACTIVE) REGIME

In this limit, the particle distribution function does not play a role in defining the physics of the instability, as it is only the bulk response that is important. The beam particles are resonant with the unstable wave over a timescale much longer than the growth time, i.e., the beam particles do not drift a distance larger than the wavelength of the unstable mode over the growth time of the instability. The growth rate of the oblique instability in the reactive regime can be calculated directly from the continuity

equation and the momentum equation in cold plasma limit $k_B T \to 0$, we find (for full derivation see Appendix C)

$$\omega_{OBL}(k) = \sqrt{\frac{3}{2^{4/3}}} \left(\frac{2\alpha}{\gamma_b}\right)^{1/3} \left(\frac{k_z^2}{k^2} + \frac{k_x^2}{\gamma_b^2 k^2}\right)^{1/3} \omega_p \tag{2.47}$$

where k_x and k_z are the longitudinal and transverse components of the wave vector relative to the beam. The transverse inertia is much smaller than the longitudinal inertia (by a factor of γ_b^2), so that the modes transverse to the beam are the easiest to be excited. The fastest growing oblique mode occurs at $k_x \sim k_z \sim k/\sqrt{2}$

$$\omega_{OBL}(k) \sim \sqrt{\frac{3}{2^{4/3}}} \left(\frac{2\alpha}{\gamma_b}\right)^{1/3} \omega_p \tag{2.48}$$

KINETIC REGIME

The linear and nonlinear features of the oblique modes in a fully kinetic framework indicates a specific orientation of the wave vector relative to the beam velocity vector for which the instability domain is unbounded. Given the symmetries of the problem, the dispersion relation for the oblique instability is given by the Eq. (2.34) within the (x, z) plane. We consider the ions are immobile providing the neutralization condition. The dielectric tensor components ϵ_{ij} are given by

$$\epsilon_{ij}(\omega, k) = \delta_{ij} + \Sigma_{\alpha=b,p} \frac{n_\alpha}{\omega^2} \int\int\int \frac{p_i}{\gamma} \frac{\partial f_\alpha^0}{\partial p_l} d^3p + \Sigma_{\alpha=b,p} \frac{n_\alpha}{\omega^2} \int\int\int \frac{p_i p_j}{\gamma^2} \frac{k \cdot \partial f_\alpha^0}{(\omega - k \cdot p/\gamma)} d^3p \tag{2.49}$$

where n_α is density of the electrons beam and plasma (hereafter labeled b and p) normalized by the total electron density.

Finally, it is useful to summarize the hierarchy of these modes for the cold regime in the (α, γ) phase space. In Table 2.1, we report the dimensionless maximum growth rates of competing instabilities, with their variation from $1 \ll \alpha < 1$ (where $\alpha = n_b/n_p$). In the case $\alpha \ll \mathbf{1}$; the couple of longitudinal and transverse modes becomes important provided the wave vectors have both the two components. In this case the growth of the instability is contributed to both components (longitudinal and transverse component see Fig. 2.4). Therefore, it is hard to distinguish between purely longitudinal and transverse mode in this case. As a result, the grow rate of this oblique instability has an intermediate value between their grow rate. On other hand, for $\alpha = \mathbf{1}$, the transverse filamentation instability grows faster than the longitudinal mode. There is no oblique extremum in this case.

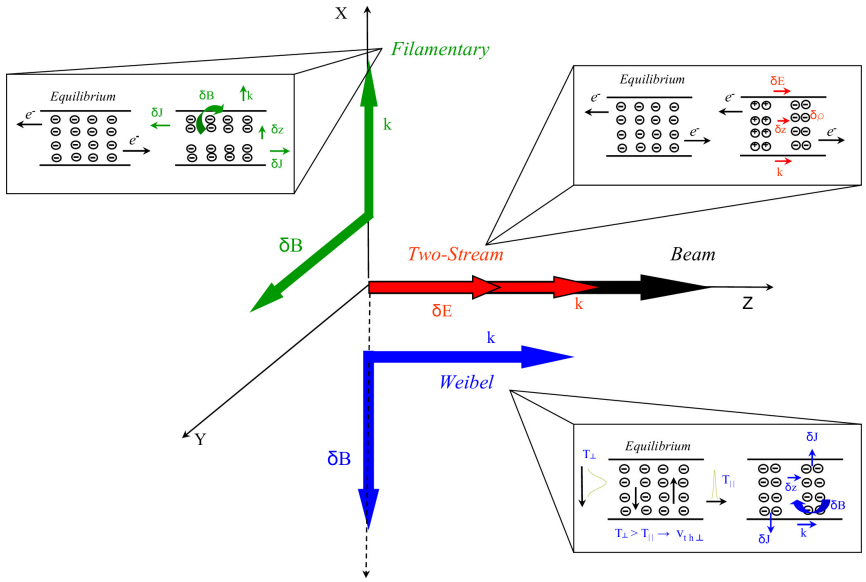

FIGURE 2.4: Illustration of the beam-plasma instabilities (Cottrill el al. [100])

TABLE 2.1: Analytical expression of the dimensionless maximum growth rate $\tilde{\Gamma}_{max}$ and associated dimensionless wave vector k in the cold limit for each class of instability in the case $\alpha \ll \mathbf{1}$ and $\alpha = \mathbf{1}$ (where $\alpha = n_b/n_p$)

	Two-stream	**Filamentation**	**Oblique**
$\alpha \ll \mathbf{1}$			
$\tilde{\Gamma}_{max}$	$\sim \frac{\sqrt{3}}{2^{4/3}} \frac{\alpha^{1/3}}{\gamma_b}$	$\sim \beta_b \sqrt{\frac{\alpha}{\gamma_b}}$	$\sim \frac{\sqrt{3}}{2^{4/3}} \frac{\alpha^{1/3}}{\gamma_b}$
$\tilde{k}_z$	~ 1	0	~ 1
$\tilde{k}_x$	~ 0	$\gg \beta_b$	$\gg 1$
$\alpha = \mathbf{1}$			
$\tilde{\Gamma}_{max}$	$\sim \sqrt{\frac{1}{2\gamma_b^3}}$	$\sim \beta_b \sqrt{\frac{2}{\gamma_b}}$	...
$\tilde{k}_z$	$\sim \frac{\sqrt{3}}{2\gamma_b^{3/2}}$	0	...
$\tilde{k}_x$	~ 0	$\gg \sqrt{2} \frac{\beta_b}{\gamma_b^{3/2}}$	...

During the past few decades, two/three dimensional, relativistic, massively parallel, particle-in-cell code are being used to model beam-plasma interactions. These simulations represent an efficient and powerful tool probing the microphysics on the time scale of the electron collective dynamics. The growth of electrostatic and transverse electromagnetic modes trigger due to the interaction of the plasma stream. The instabilities give rise to the growth in the electric or magnetic field energy which grows exponentially with time ($< E^2 >, < B^2 > \propto exp(2\Gamma t)$), where Γ is the growth rate of the instabilities. In general, we normally discuss the linear growth of a given instability since theory can only predict the linear phase of the instability. Obviously, the linear phase cannot grow indefinitely. At some point the instability enters the non-linear phase and the instability stops growing.

2.4 CONCLUSIONS

In conclusion, the stability of beam propagation in vacuum and plasma is introduced. The full electromagnetic dispersion relation in the entire k-space associated with the Bi-Maxwellian and waterbag distribution functions is briefly described. We also briefly discuss condition how current filamentation instability can be observed in the finite beam-plasma system.

Relativistic and non-relativistic plasma outflows are quite ubiquitous in astrophysical scenarios, as well as in laboratory plasmas. The plasma outflows are an important candidate to mediate shock formation, energy transfer processes, non-thermal particle acceleration and generation of large-scale magnetic field via current filamentation (CFI)/ Weibel instability. The goal of this thesis is to identify and investigate those astrophysical conditions, which will allow as to reproduce astrophysical scenarios in laboratory plasmas.

CHAPTER 3

PROPAGATION OF A NEUTRAL BEAM INTO AN UNIFORM PLASMA

3.1 OVERVIEW

Relativistic outflows of lepton mass, with an arbitrary mixture of electrons-positrons-ions ($e^-e^+p^+$), are ubiquitous in astrophysics such as jets from active galactic nuclei (AGN), gamma-ray bursts (GRB), and ultrahigh-energy cosmic rays (UHECR). Recent advent in the observation of such high-energy astrophysical object demands to be investigated in the laboratory which is required to gain insights into the underlying physics. It is known that these baryonic highly collimated objects are expanding at Ultra-relativistic velocity interacting with surrounding mediums. There are many outstanding problems in astrophysics closely associated with these flows and have strong connections with particle acceleration, shock formation, magnetic field generation or non-thermal radiation. The role of microscopic collisionless plasma instabilities plays a pivotal role dissipating the free kinetic energy of an ultra-relativistic plasma-shell into electric and magnetic turbulence, ultra-high energy charged particles and non-thermal radiation.

Although such extreme experimental conditions relevant for astrophysics are complex and needs a careful design of such complex experiments, a theoretical together with sophisticated computer simulations effort is quite essential to provide the experimental condition for future fireball experiments. The possibility to explore in the laboratory the physics of relativistic outflows would be of great interest not only for astrophysics but also to understand the physics of relativistic beam-plasma interactions. Experimentally probing of the relativistic fireball model is still an open challenge, since the creation of these astrophysical conditions in the laboratory is very

difficult. However, present laboratory facilities, such as the Stanford Linear Accelerator (SLAC), may offer a possible solution to this problem [101, 102]. Nevertheless, theoretical and numerical work is still necessary. Thus, the prime goal of this work is to investigate the physics of fireball beams by mimicking astrophysical conditions in the laboratory through the detailed investigation of the expansion and dynamics of fireball beams in plasmas.

This Chapter is organized as follows: In section 3.2, we briefly elaborate the future possible experimental set-up within the framework provided at the Stanford Linear Accelerator Center (SLAC), could produce a neutral beam that resembles high-energy astrophysics phenomena in the lab. Section 3.3 demonstrates the regime of the existence of two competing instabilities i.e Current Filamentation and Oblique Instability which depends on the bunch length. We investigated a detailed numerical and theoretical studies of a fireball beam propagation into a pre-formed static plasma using *ab initio* multi-dimensional relativistic PIC simulations, which mimic realistic astrophysical scenarios in Section 3.3.1. The detailed investigation of SLAC fireball beam interaction with plasma is being carried out using ab initio 3D/2D PIC simulations. The numerical method OSIRIS [70, 71] and unique computational infrastructure (IST cluster), which supports this work, is developed and maintained at GoLP. The multi-dimensional dynamics of the fireball beam using different densities and beam sizes are demonstrated in section 3.3.2. In Section 3.4, the effects of beam emittance with different beam velocities are described. In addition, the effect of energy spread of the fireball beam is demonstrated through 2D PIC simulations and verified by the theoretical predictions in Section 3.5. Finally, the conclusions are presented in Section 3.7.

3.2 ULTRA-RELATIVISTIC FIREBALL BEAMS IN THE LABORATORY

The SLAC National Accelerator Laboratory is capable of delivering electron e^- and positron e^+ beams of the order of $\simeq GeV$ with the bunch length of the order of the plasma wavelength or about 10 μm and consists of 10^{10} particles. The bunch energy density is the order of $10^{13} J/m^3$. Typical relativistic bunched beam Debye radius (λ_D) is smaller than bunch length but larger than the transverse beam size. With the help of a sailboat magnetic chicane, the relativistic electron and positron bunched beam could be used to combine with an equal charge. High-resolution beam position monitors have been demonstrated to aligned these two beams to micro precision and temporal locations could be synchronized using the damping rings' RE phase control which help effectively both in space and time to create a neutral beam (*fireball beam*). Neutral co-moving e^-, e^+ beams reduce the disruptive effect of one beam's electromagnetic

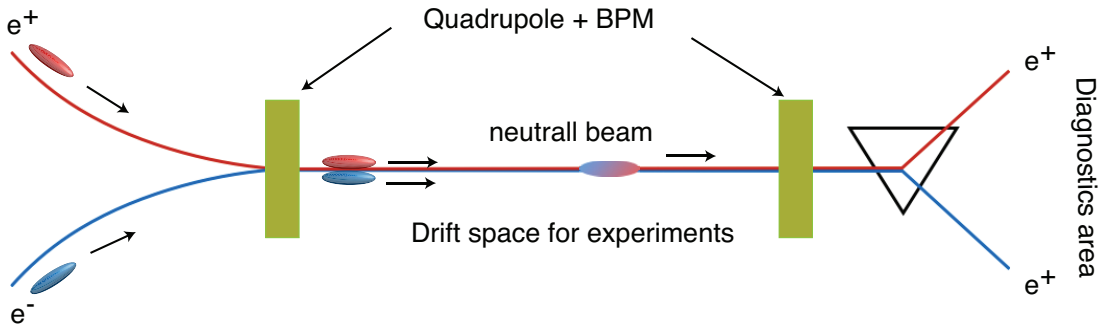

FIGURE 3.1: slack layout: Combining electron and positron bunches to form a relativistic plasma. [101]

fields (EMF) by compensating the EMF fields generated by another beam. Hence, such neutral beams could be stable at the sub-picosecond level. The experimental step is illustrated in Figure 3.1 which could produce a neutral beam using the SLAC facility. For a relativistic bunched beam, the emittance is one of the key parameters which defines the beam's transverse temperature given by

$$kT_{\perp} = \frac{\gamma mc^2 \epsilon^2 \beta^2}{4\sigma_r^2} \tag{3.1}$$

where γ the Lorentz factor, σ_r the transverse beam size, $\beta = |v|/c$, c speed of light and ϵ is the beam's emittance. The longitudinal temperature due to energy spread is negligible for relativistic beams. Using typical SLAC parameters, the beam emittance in longitudinal direction $\epsilon_{\parallel}$ and transverse $\epsilon_{\perp}$ direction could be achieved to $10^{-10} mrad$, $10^{-8} mrad$ respectively. Note also that, as in astrophysics, these parameters correspond to a collisionless fireball-plasma interaction: $\nu_{ei}/\omega_p = \vartheta(10^{-18})$, where ν_{ei} is the beam e^-, e^+ background p^+ collision frequency. This creates a possibility to generate the first-ever collision between relativistic neutral plasmas in the laboratory: a relativistic fireball beam propagating into a e^-, p^+ plasma at rest, separating the effects of the space charge fields associated with a charged beam.

3.3 PIC-SIMULATIONS OF A FINITE NEUTRAL BEAM INTERACTION WITH PLASMA

The temporal and spatial growth of self-electromagnetic fields as result of fireball beam interaction with plasma is examined. The results focus on the underlying physics of multi-dimensional effects, such as beam defocusing due to the finite beam radius and finite emittance. We have simulated a wide range of fireball beam Lorentz

factors $\gamma \sim 10^3$ to 10^4, fireball beam peak density 10^{15} - 10^{17} cm^{-3} and transverse beam temperature, with the aim of providing the optimal conditions to explore instabilities in the laboratory.

A distinct regimes of beam-plasma interaction is identified, where the ratio between the transverse beam size σ_y and the plasma collisionless skin depth (c/ω_p), where $\omega_p = \sqrt{4\pi n_0 e^2/m_e}$ is the plasma frequency with n_0 being the plasma the plasma density, m_e the mass of the electron, e the charge of the electrons and c the speed of light, drives the Current Filamentation or Oblique Instability. It is found that in the case of short fireball beams, i.e beams are shorter than the plasma wavelength, plasma return currents can flow through the beam leading to the growth of CFI. The effect of the propagation of long beams, i.e beams are longer than the plasma wavelength is also investigated by keeping the total number of particles constant with exact parameters. The results show some degree of tilting of magnetic field lines, which clearly indicates coupling of the CFI and the two-streaming instability i.e Oblique Instability. The existence of two-streaming instability reduces the growth rate of the CFI. The effect of higher temperature has also been investigated. When the beam is warm, the Oblique Instability saturates. The filament inside the fireball is destroyed due to the temperature effect.

3.3.1 INTERACTION OF A SHORT ($\sigma_y \leq c/\omega_p$) BEAM WITH STATIC PLASMA

In order to illustrate the generation of magnetic fields through the CFI, the two and three dimensions numerical simulations were performed with the fully relativistic, massively parallel particle-in-cell (PIC) code OSIRIS [70, 71] by considering the propagation SLAC fireball beam in a pre-formed plasma. The simulations use a moving window travelling at c. The simulation box has absorbing boundary conditions for the fields and for the particles in the transverse direction. The globally neutral fireball beam is initialized at the entrance of a stationary plasma with $n_0 = 10^{17}\ cm^{-3}$. The initial density profile for the electron and positron fireball beam is given by $n_b = n_{b0} \exp(-x^2/\sigma_x^2 - y^2/\sigma_y^2)$ where $n_{b0} = n_0 = 10^{17}$ cm^{-3}, $\sigma_x = 0.99\ c/\omega_p = 10.2\ \mu$m and $\sigma_y = 2\ c/\omega_p = 20.4\ \mu$m are the bunch peak density, length and transverse waist, respectively. The simulation box dimensions are $L_x = 8.02\ c/\omega_p$ and $L_y = 20.0\ c/\omega_p$. The box is divided into 128×512 cells with 2×2 particles per cell. The globally neutral fireball beam used in the simulation consists $1.8 \times \times 10^{10}$ same number of electrons e^- and positrons e^+ with an incoming energy of 29 GeV and a normalized emittance of 2×10^{-5}m $-$ rad, corresponding to a peak beam density $n_b = n_e$. Hence, the beam propagates with Lorentz factor $\gamma_b = 5.6 \times 10^4$, with transverse velocity spread $v_{th}/c = 1.7 \times 10^{-5}$ and with no momentum spread in the longitudinal direction. We used a total of 2 million simulation particles which is pushed for $\sim 10^4 c/\omega_p \simeq 10$ cm of pre-formed plasma. The time step is $0.033/\omega_p$. We have performed simulation of a

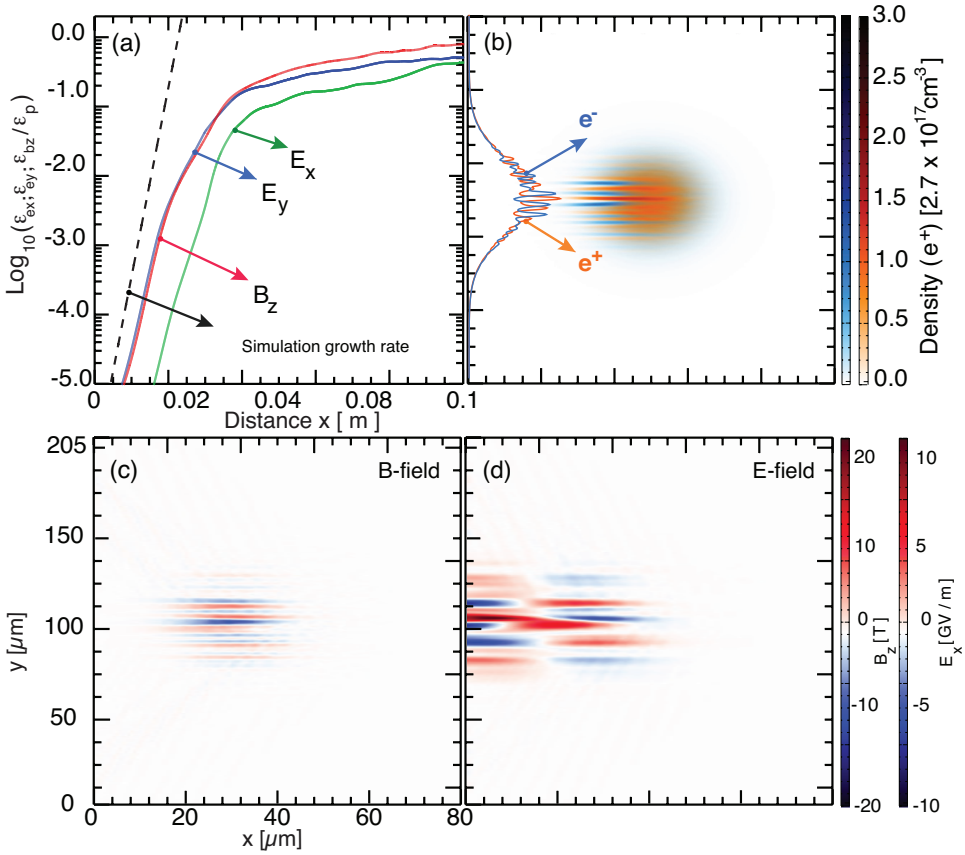

FIGURE 3.2: The interaction of a neutral e^-, e^+ fireball beam having a Gaussian profile with $\sigma_x = 2\sigma_y = 20.4\,\mu m$, peak density $n_b = 2.7 \times 10^{17}\,\mathrm{cm}^{-3}$, $\gamma_{b0} = 5.6 \times 10^4$ with a static plasma with $n_0 = n_b$. (a) Evolution of Transverse magnetic ϵ_{bz} (red), Longitudinal ϵ_{ex} (green) and transverse electric ϵ_{ey} (blue) field energy as function of distance normalized to the initial kinetic energy of the beam $\epsilon_p = (\gamma_0 - 1)V$, where $V_b = \pi \times \sigma_x \times \sigma_y$ is the volume of the beam. The dotted line represents the theoretical growth rate of the CFI (b) the density filaments corresponds to the electron e^- (blue) and positron e^+ (red) spatially separated from each other (c) shows the associated transverse magnetic (B_z) filaments at linear regime after 3.7 cm (d) due to space charge radial electric field (E_x) created.

neutral fireball beam into vacuum to guarantee it's stable propagation with at constant radius. The background neutral-plasma (e^--p^+) is assumed to be static.

Figure 3.2 depicts the growth of the transverse magnetic field energy (panel a), the beam filaments due to the CFI (panel b), and the typical electromagnetic field structure (panels c and d). In Fig. 3.2a shows that the growth of the magnetic field energy as a function of the propagation distance is exponential. The electromagnetic field is

normalized with respect to the initial kinetic energy of the particles $\epsilon_p = (\gamma_0 - 1)V_b$, where $V_b = (\pi \times \sigma_x \times \sigma_y)$ is the volume of the beam. Simulations reveal that the field energy grows at the expense of the total kinetic energy of the fireball beam. The linear growth rate of the CFI measured in the simulation is $\Gamma_{CFI}/\omega_p \simeq 6.0 \times 10^{-3}$, in good agreement with Silva et. al [67]. As a consequence of the instability, the beam breaks up into narrow (with a width on the order of $0.5c/\omega_p$, which corresponds to $5\mu m$) and high current density filaments. Figure 3.2(b) shows that these electron-positron filaments are spatially separated from each other. Each filament carries strong currents which lead to the generation of strong out-of-the-plane (i.e. azimutal) magnetic fields with amplitudes beyond 20 T. The azimutal magnetic fields are also filamented, as shown in Figure 3.2 (c). Because of their finite transverse momentum, simulations show that current filaments can merge. As merging occurs, the width of the filaments increases, until beam breakup occurs. At this point, the CFI stops growing, and no more beam energy flows into the generation of azimutal magnetic fields. Simultaneously, radial E-fields above 15 GV/m are also generated (Fig. 3.2d).

To examine the multi-dimensional effect on the growth of CFI, additional 3D PIC simulations in OSIRIS [70,71] were carried out. In these simulations, the fireball beam is defined with Gaussian profiles in all directions with rms sizes: $\sigma_x = \sigma_y = 2\sigma_z = 2c/\omega_p = 20.4\mu m$ where $n_{b0} = n_0 = 10^{17}\ cm^{-3}$ is the bunch peak density. The system is studied numerically with a $205 \times 205 \times 82\ \mu m^3$ window moving at the speed of light along the z-direction, and discretized in $400 \times 400 \times 80$ cells with absorbing boundary conditions for the fields and for the particles in the transverse x, y directions.

The results shown in Fig. 3.3, reveal the similar results demonstrating the existence of CFI. Figure 3.3 (a)-(c) shows the beam filament structure after 10 cm propagation in the laboratory plasma, or, equivalently, to the propagation of a fireball with a density 1 cm^{-3} in $>$ 50 km in the background density of 1 cm^{-3}. Figure 3.3 (d)-(e) illustrates the large B-fields in radial and azimuthal magnetic field generated due to the CFI. The CFI generates well-defined current (and density) filaments, which size increases as the beam propagates in the plasma, and may grow to a thickness above 5 μm $\simeq 0.5\ c/\omega_{\rm pe}$. These conditions correspond to a beam with $\sigma_r/(c/\omega_{\rm pe}) \simeq 2$, which explains the few filaments obtained at saturation, reached when the filaments coalescence ceases and the B-field energy remains constant. The large currents associated with the beam filaments generate local B-fields up to 2 MGauss (Fig. 3.3d). The space charge separation, also associated with the filaments, leads to radial E-fields as high as 5×10^8 V/cm. Finally, a system of filaments is present in the background plasma, behind the beam, evidencing a 3D structure. As the filaments merge, the space-charge separation leads to the plasma blowout and to the generation of strong E-fields.

As merging occurs, the width of the filament increases, until the beam filament width becomes comparable to the initial bunch transverse size. At this point, the CFI stops growing, and no more beam energy flows into the generation of azimuthal mag-

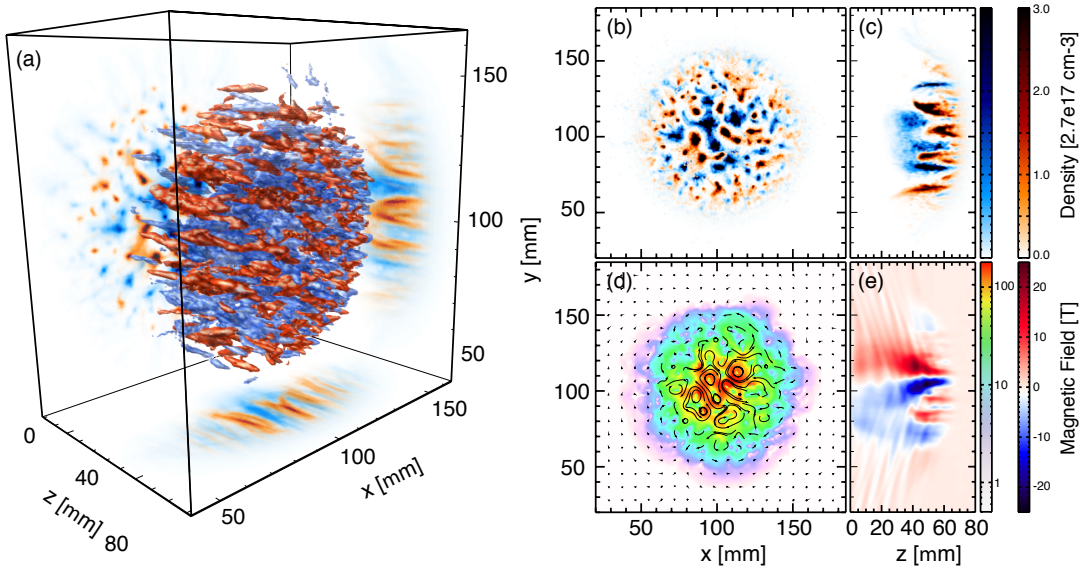

FIGURE 3.3: Beam density and B-field after 10 cm propagation in a plasma with $n_e = 2.7 \times 10^{17}$ cm^{-3}. (a) Isosurfaces of e^- (blue) and e^+ (red) density; projections correspond to the integration along the corresponding direction. (b-c) 2D central beam density slices (e^- blue, e^+ red). (d) 2D central slice of radial B-field, $B_\perp = \sqrt{B_x^2 + B_y^2}$, responsible for particle transverse motion and radiation (vectors represent B-field lines). (e) Integral of B_y along y ($\int B_y dy / \int dy$), measurable experimentally by Faraday rotation.

netic fields. Simultaneously, radial E-fields above 10 GV/m are also generated (Fig. 1d) due to space charge effects related to the separation between plasma electrons and ions. The beam transverse size is larger than the plasma skin depth, which corresponds to the spatial scales where the instability growth rate is maximum [79]. Our simulations show a clear transition from the linear to nonlinear stage of CFI due to the merging of fireball bunch filaments and we expect that the mechanisms leading to the saturation of the magnetic fields in our simulations will not differ from well-known saturation mechanisms, described in [41, 103, 104]

In Fig. 3.4, we present the evolution with propagation distance in the plasma of the total normalized energy in the B-field, ϵ_B for different beam/plasma parameters, illustrating the exponential growth and saturation within the 10 cm range. The growth rates ($\Gamma_{\rm std}/\omega_{\rm pe} \simeq 2.0 \times 10^{-3}$, $\Gamma_{\rm hot}/\omega_{\rm pe} \simeq 1.7 \times 10^{-3}$, $\Gamma_{\rm high}/\omega_{\rm pe} \simeq 2.3 \times 10^{-3}$) are within the range predicted for this configuration for the purely transverse CFI ($\Gamma_{\rm max}/\omega_{\rm pe} \simeq \sqrt{2}\beta_0/\sqrt{\gamma_0}[1+\beta_{\rm th}]$, with $\beta_{\rm th} = v_{\rm th}/c$ the particle thermal rms spread of velocity [67]). A more detailed analysis reveals, however, that for higher plasma densities (keeping the beam density fixed) the growth rate is higher, but the saturated level of the B-field is lower. The former is an indication of the spatial-temporal charac-

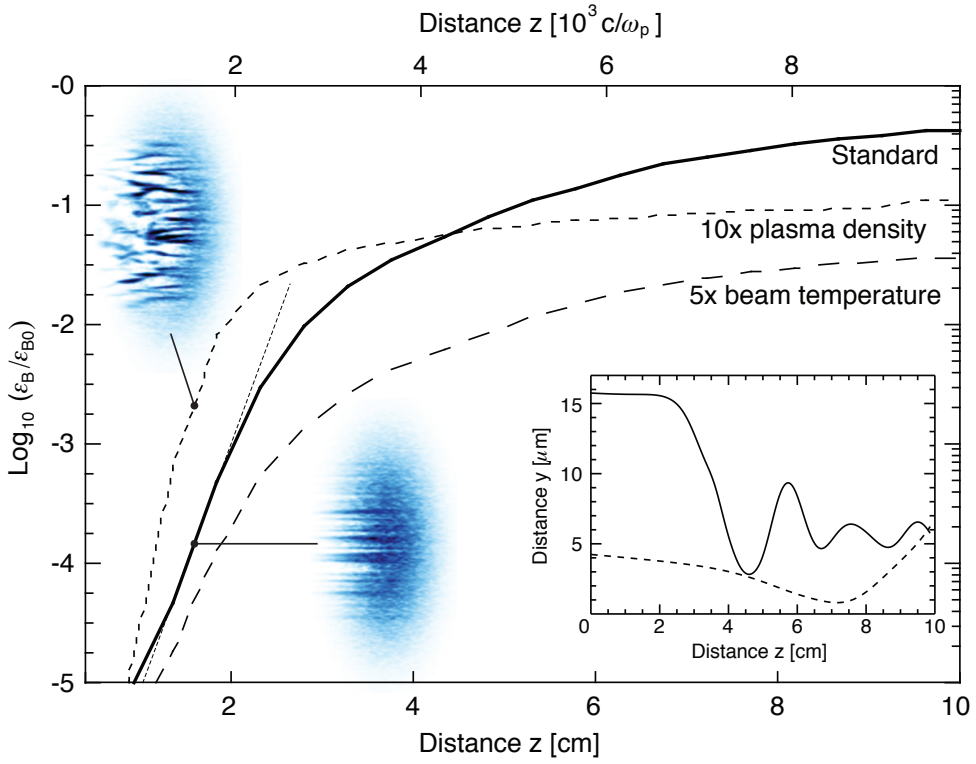

FIGURE 3.4: Evolution of the equipartition parameter ϵ_B, i.e., the total B-field energy ($B_x^2 + B_y^2 + B_z^2$) normalized to the kinetic energy of the particles $\epsilon_p = (\gamma_0 - 1)V_b$, ($V_b$ the volume of the beam) for different beam and plasma parameters. Values are normalized to ϵ_{B0}, where B_0 is the field when the growth becomes exponential (after ~ 0.1 mm, or $10/\omega_{\rm pe}$). Standard case (solid line): *fireball beam* with 2×10^{-5} m-rad emittance, in a plasma with $n_e = 2.7 \times 10^{17}$ cm^{-3} (which also defines the baseline density for the normalization). The dotted line illustrates the linear growth rate. Slices of the density in the middle of the beam after ~ 1.5 cm of plasma (plotted in blue) illustrate the difference in the instability structure. The inset includes the trajectories of two fireball electrons for the standard case.

ter of the instability in this configuration, while the latter is evidence for the different saturation mechanisms involved when the mixed mode/tilted filamention is dominant [37].

3.3.2 MODELLING OF LONGER BEAMS IN LONGITUDINAL DIRECTION

In the previous section, a short beam, when compared with the plasma wavelength $\lambda_p = 2\pi c/\omega_p$ was considered. Here, we investigate the propagation of longer beams with $\sigma_x \geq \lambda_p$, while keeping the total number of the beam particles constant. In these

TABLE 3.1: Modelling of longer beams with constant beam particle number

Run	**beam size** $\sigma_{\parallel}$	**beam size** $\sigma_{\perp}$	$\alpha = n_{b0}/n_{e0}$
R_1	$\lambda_{pe} = 6.28$	2.00	1
R_2	$2\ \lambda_{pe} = 12.56$	2.00	0.01274
R_3	$4\ \lambda_{pe} = 25.12$	2.00	0.006368
R_4	$6\ \lambda_{pe} = 37.68$	2.00	0.004245
R_5	$8\ \lambda_{pe} = 50.24$	2.00	0.003184
R_6	$10\ \lambda_{pe} = 62.80$	2.00	0.002547

conditions, we found that the growth rates of the CFI can be substantially lower and that competing instabilities also grow.

With the set-up described in the previous section, we have further carried out simulation with same parameter except the longitudinal beam length/peak beam density which is given in Figure 3.5. We have performed a detailed study of different longer beams as shown in the following table 3.1.

ROLE OF THE PEAK BEAM DENSITY AND BEAM DURATION IN THE GROWTH OF CURRENT FILAMENTATION INSTABILITY

In the previous section, and for illustration purposes only, we have considered that the total beam density was twice the background plasma density. In this section, we will investigate the propagation of beams with lower peak densities. In order to keep the number of particles constant, we then increase the beam length, such that $\sigma_x \geq \lambda_p$. In these conditions, the OBI competes with the CFI [97]. The OBI can grow when the wave-vector is at an angle with respect to the flow velocity direction, and it leads to the generation of both electric and magnetic field components. The maximum growth rate for the CFI and the OBI, assuming the beams are infinitely long, are given by $\Gamma_{\mathrm{CFI}} \sim \sqrt{\alpha/\gamma_b}\,\beta_{b0}$ and $\Gamma_{\mathrm{OBI}} \sim \sqrt{3}/2^{4/3}(\alpha/\gamma_b)^{1/3}$ respectively [105], where α is the beam (n_b) to plasma density (n_e) ratio and $\beta_{b0} = v_b/c$ is the normalized velocity of the beam. Thus, the ratio between the CFI growth rate and the OBI growth rate is given by:

$$\frac{\Gamma_{OBI}}{\Gamma_{CFI}} = \frac{\sqrt{3}}{2^{4/3}} \frac{1}{\beta_b} \left(\frac{\gamma_b}{\alpha}\right)^{1/6} \tag{3.2}$$

Equation (3.2) provides criteria for determining which of the two instabilities will dominate. The OBI is almost universally faster than the CFI. However, due to the weak dependence on γ_b/α, given $\gamma_b \sim 10^4$ the OBI will begin to dominate when α is much smaller than 1.

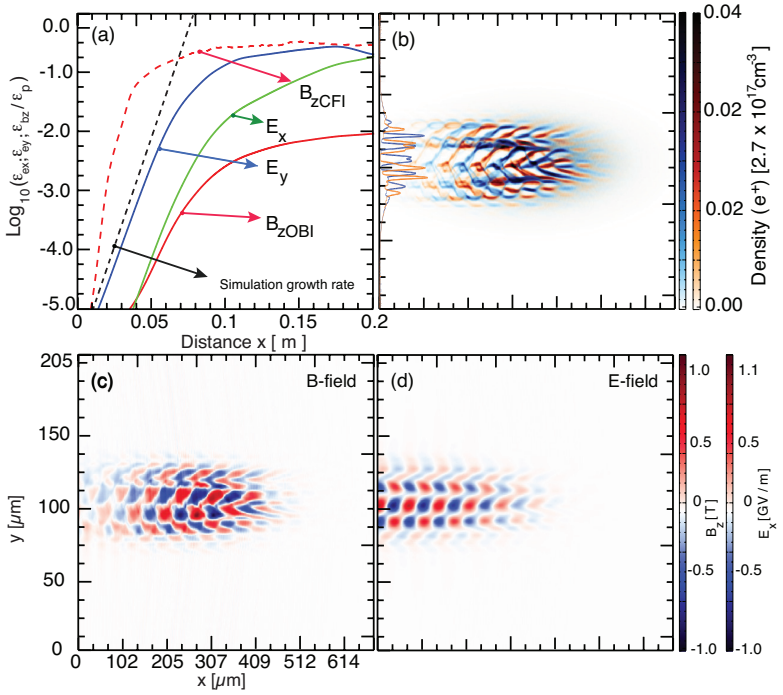

FIGURE 3.5: Interaction of a neutral e^-, e^+ fireball beam with longitudinal beam size $\sigma_x = 2 \times \lambda_p$ and a static plasma by keeping constant beam particle number. (a) Evolution of Transverse magnetic ϵ_{bz} (red), Longitudinal ϵ_{ex} (green) and transverse electric ϵ_{ey} (blue) field energy as function of distance normalized to the initial kinetic energy of the beam ϵ_p. The dotted line represents the theoretical growth rate of OBI (b) the density filaments corresponds to the electron e^- (blue) and positron e^+ (red) spatially separated from each other (c) shows the associate transverse magnetic (B_z) filaments at linear regime between $x_1 = 0.0551 - 0.0556$ m (d) the space charge separation leads to radial electric field (E_x).

In order to verify this hypothesis, we have carried out additional 3D and 2D dimensional OSIRIS PIC [70, 71] simulations using the ini tial set up described in Sec. 3.3.1, varying σ_x between $2\lambda_p < \sigma_x < 10\lambda_p$, for which α varies between $0.0026 < \alpha < 1$. In all these cases, our results have been consistent showing the evidence of the OBI growth.

In Figure 3.5, we show an illustrative simulation result considering $\sigma_x = 2 \times \lambda_p$ and with $n_b = 1.274 \times 10^{15}$ cm^{-3}, for which $\alpha = 0.01274$. In order to describe the propagation of a longer beam, we have increased the simulation box length. The box dimensions are then $L_x = 63c/\omega_p$ ($L_y = 20c/\omega_p$ remains identical to that of Sec. 3.3.1). The box is divided into 1024×512 cells and uses 4×4 particles per cell for each species.

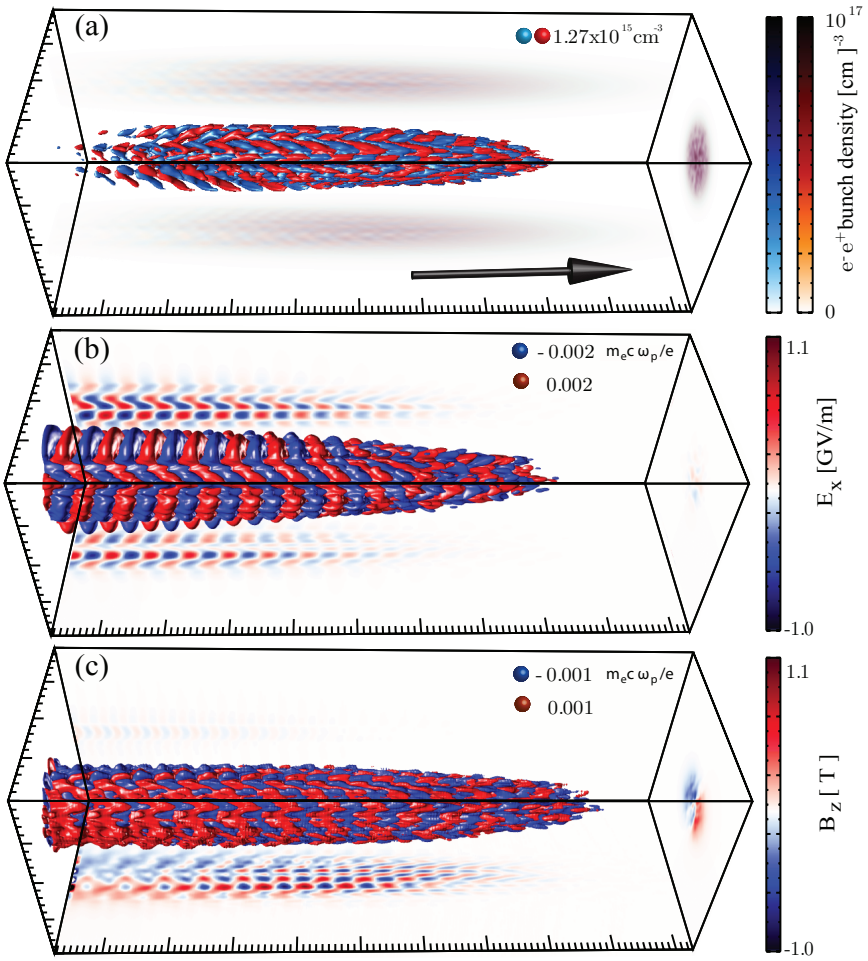

FIGURE 3.6: Simulation results of the propagation of beams with longer longitudinal bunch ($\sigma_x \geq \lambda_p$) and lower peak densities. The arrow indicates the bunch propagation direction. (a) Isosurfaces of e^- (blue) and e^+ (red) density showing existence of Oblique Instability (b) Longitudinal electric (E_x) fields shows the wakefield (c) Magnetic field (B_y) filaments show some degree of tilting, revealing coupling between Current Filamentation and Two-stream instability

Figure 3.5 (a) illustrates the evolution of the longitudinal and transverse electric and transverse magnetic energy (normalized to $\epsilon_p = (\gamma_0 - 1)V_b$, where $V_b = (\pi \times \sigma_x \times \sigma_y)$ is the volume of the beam). The emergence of oblique modes can be seen in Figs. 3.5 (b), which shows tilted beam filaments. The corresponding oblique wave-vector couples the transverse (filamentation) and longitudinal (two-stream) instabilities. Unlike Fig. 3.2, the simulation results in Fig. 3.5 show that the transverse electric field component provides the dominant contribution to the total field energy. The

plasma is only weakly magnetized $\omega_c/\omega_p = 0.01$, and the CFI does not play a critical role in the beam propagation. The longitudinal and transverse electric fields grow exponentially, as predicted by the linear analysis of the OBI, matching well the simulation results. The growth rate measured in the simulations is $\Gamma_{\max}/\omega_p \simeq \Gamma_{\rm OBI} \simeq 2.1 \times 10^{-3}$, while the theoretical growth rate is $\simeq 2.0 \times 10^{-3}$. The OBI generates plasma waves with strong radial electric fields in excess of 500 MV/m (Fig. 3.5 (d)). After 20 cm, the beam can not penetrate deeper inside the plasma, which leads to the saturation of the OBI.

These results were further supported by one-to-one 3D simulations using identical simulations setup in OSIRIS [70, 71], which confirms presence of tilting angle in the beam filament and magnetic field filaments indicating coupling between Current Filamentation and Two-stream instability shown in panel 3.6 (a) and (c).

3.4 EFFECTS OF FINITE BEAM WAIST AND EMITTANCE

Theoretical and numerical studies performed to identify the effect of beam emittance on the growth of plasma instabilities and their saturation [42, 106, 107] typically assume that the beam is infinitely wide. In this section, we will investigate the role of the beam emittance considering finite beam size effects, in order to make closer contact with laboratory conditions. To study the influence of the beam emittance on the propagation, we first consider the equation for the evolution of the beam waist σ_y in vacuum [108]:

$$\frac{1}{c^2}\frac{\mathrm{d}^2\sigma_y}{\mathrm{dt}^2} = \frac{1}{4}\frac{\epsilon_N^2}{\sigma_y^3\gamma_b^2}, \tag{3.3}$$

where σ_y is the beam radius, $\epsilon_N \simeq \Delta p_y \sigma_y$ is a figure for the beam emittance (corresponding to the area of the beam transverse phase space), and Δp_y is the transverse momentum spread. According to Eq. (3.3), the evolution for σ_y and for sufficiently early times is given by:

$$\sigma_y \simeq \sigma_{y0}\left(1 + \frac{\epsilon_N^2\, t^2 c^2}{4\sigma_{y0}^4\gamma_b^2}\right)^{1/2}, \tag{3.4}$$

where σ_{y0} is the initial beam radius. Hence, according to Eq. (3.3), the rate at which σ_y increases is:

$$\frac{1}{\sigma_y}\frac{\mathrm{d}\sigma_y}{\mathrm{dt}} = \frac{1}{4}\frac{t\, c^2\, \epsilon_N^2}{\sigma_{y0}^2\gamma_b^2}\frac{1}{\sigma_y^2}, \tag{3.5}$$

Equation (3.5) indicates that the beam expands in vacuum due to its transverse momentum spread. As the beam expands, n_b decreases as $n_b/n_e \sim (\sigma_{y0}/\sigma_y)^2$, in 3D, and as (σ_{y0}/σ_y), in 2D. Because of the reduction of n_b/n_e, the growth rates for the CFI and for the OBI will also decrease. We then estimate that these instabilities (i.e

CFI and OBI) are suppressed when the rate at which n_b/n_e decreases is much higher than the instability growth rate. Matching the rate at which the beam density drops, which in 2D is given by $(1/\sigma_y)$ $(\mathrm{d}\sigma_y/\mathrm{dt})$, to the growth rate of the instability (Γ) gives an upper limit for the maximum beam divergence $\theta = \Delta p_y/\gamma_b$ (and emittance $\epsilon_N \approx \sigma_y(< p_y^2 >)^{1/2}$) allowed for the growth of the CFI/OBI:

$$\theta = 2\left(\frac{\Gamma\sigma_{y0}^2}{L_{\mathrm{growth}}\, c}\right)^{1/2}, \tag{3.6}$$

where we have considered that $t \sim L_{\mathrm{growth}}/c$ in Eq. (3.6), being L_{growth} the growth length of the CFI/OBI instability. Equation (3.6) then gives the threshold beam divergence, beyond which the CFI/OBI will be suppressed. It indicates that beams with higher energy can support higher thermal spreads and still be subject to the growth of the CFI because the beam expands slowly in comparison to lower energy beams. Similarly, beams with higher σ_{y0} also support higher emittance than narrower beams because of the slower expansion rate.

To confirm our theoretical findings, we performed additional two-dimensional simulations using fireball beams with relativistic factors $\gamma_b = 700, 1050, 1400$ (the lower γ_b factors used now, in comparison to Sec. 2, minimize the computational requirements). We use $\sigma_x = 0.22\ c/\omega_p = 11.7\ \mu$m and $\sigma_y = 10\ c/\omega_p = 530\ \mu$m with peak density $n_{b0} = 10\, n_e = 10^{15}\ \mathrm{cm}^{-3}$. For each case, we varied the transverse temperature $\Delta p_y = \gamma_b\theta = 1, 3, 5, 7, 10$ and 20 in order to determine the threshold beam spread for the occurrence of instability. We note that we have used the classical addition of velocities in the beam thermal spread initialization in order to more clearly identify the dependence of evolution of the instabilities with emittance.

Figure 3.7(a) shows that the magnetic field energy decreases with increasing transverse momentum spread. Fig. 3.7 (a) also shows a transition in the evolution of the magnetic energy between $\Delta p_y = 10$, where the B-field still grows at the end of the simulation, and $p_y = 20$, where the B-field decreases with propagation distance. According to Eq. (3.6), using $L_{\mathrm{growth}} \sim 0.037$ m and $\Gamma_{\mathrm{CFI}} \sim 1.657 \times 10^{11} s^{-1}$, we obtain the threshold $\theta \sim 0.12$ for the shutdown of the instability. This is in good agreement with Fig. 3.7 (a).

Figure 3.7 (b) depicts the dependence of the threshold beam emittance with the fireball beam energy. Figures 3.7 (c)-(d) show the positron density for two simulations, where all the parameters are kept constant, except for the beam emittance. In particular, in Fig. 3.7 (c) a beam emittance of $\Delta p_y = 1$, much smaller than the threshold value given by Eq. (3), has been considered. In this case, the CFI develops, leading to the filamentation of the beam (see Fig. 3.7c) and to the exponential growth of the magnetic field energy (see Fig. 3.7 (a), red curve). However, in the second case (Fig. 3.7 (d)) a higher beam emittance $\Delta p_y = 10$ is considered. This suppresses the growth of the

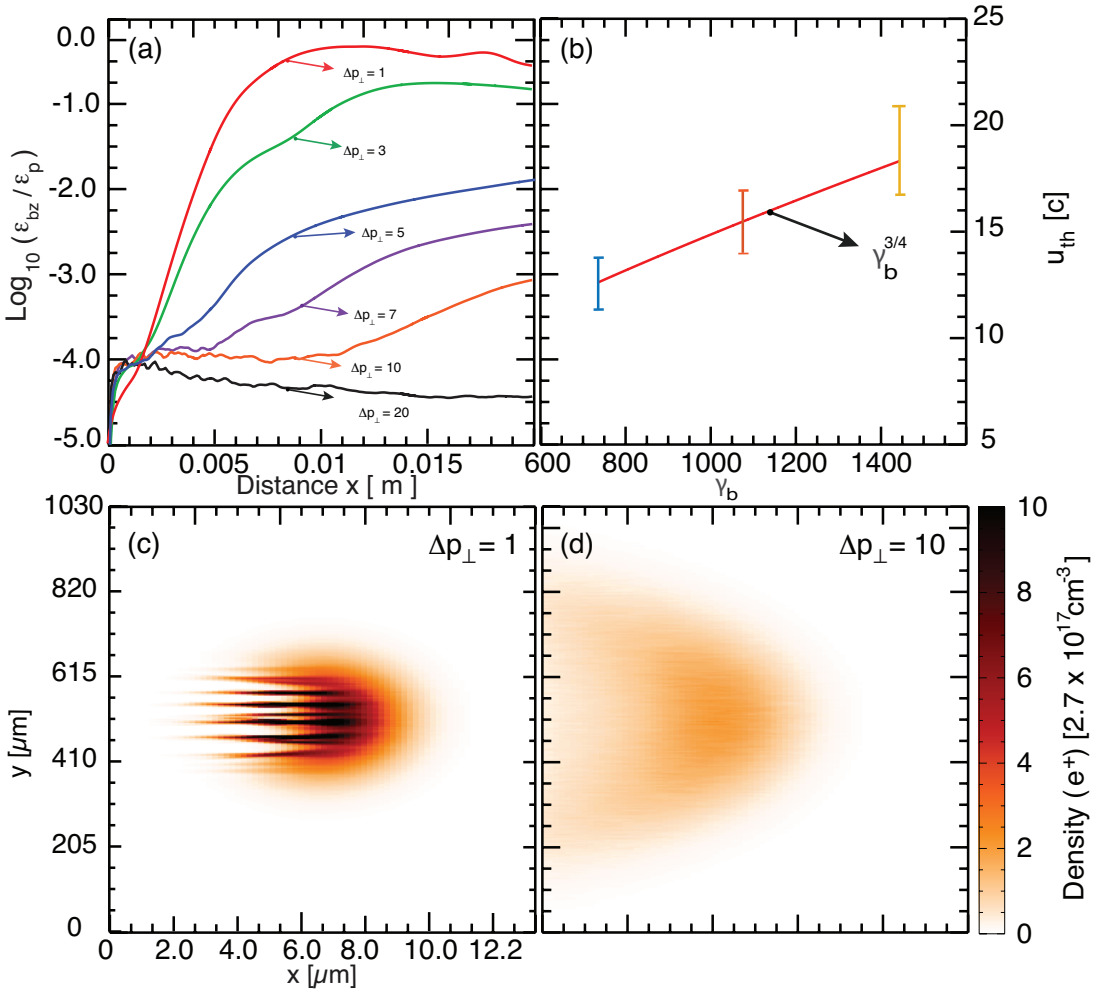

FIGURE 3.7: (a) Temporal evolution of the transverse magnetic field energy for different beam emittance (b) Thermal velocities as function of Lorentz factor γ_b, filamentation suppressed for higher thermal velocities. At time $t = 705.60\ \ [1/\omega_p]$, panels (c)-(d) show beam filaments for thermal velocities $\langle p_z \rangle = \langle p_z \rangle = 1, 3, 5, 7, 10, 20$ from 2D PIC simulations.

magnetic field energy (see Fig. 3.7 (a), orange curve). As a result, the beam expands before the development of the CFI. These results show that the growth of CFI can only be achieved if the beam emittance is sufficiently small.

3.5 EFFECT OF BEAM ENERGY SPREAD

In typical laboratory settings [80], electron-positron fireball beams can contain finite energy spreads. It is, therefore, important to evaluate the potentially deleterious role of the energy spread in the growth of CFI. In this section, we then present simula-

tion results with finite longitudinal momentum spreads. We consider that the central beam relativistic factor is $\gamma_b = 700$, and compare two simulations with $\Delta p_x/\gamma_b = 0.13$ and $\Delta p_x/\gamma_b = 0.29$ (Δp_x is the longitudinal momentum spread). All other simulation parameters are similar to those described in previous section.

In order to study the role of the beam energy spread, we derive the CFI growth rate considering a model where the fireball bunch is decomposed into beamlets with different energies, but where each beamlet has no energy spread and no transverse emittance. We consider electromagnetic waves propagating with the transverse wave vector $\vec{k} = k\hat{z}$, with the counter-propagating neutral fireball beams propagating in the x-direction. In equilibrium, the densities of each electrons (e^-) and and positrons (e^+) is $n_a e^-$ and $n_a e^+$, respectively, where a = (1,n) and n is the number of beamlets. Each beamlets has longitudinal momentum $p_a^- = p_a^+$. Thus, the charge and current densities of each fireball beam is,

$$\sum_{a=1}^{a=n} n_{a\alpha} Q_\alpha = 0 \text{ and } \sum_{a=1}^{a=n} n_{a\alpha} Q_\alpha \beta_{a\alpha} c = 0. \tag{3.7}$$

where α denotes the charge of electron (e^-) and positron (e^+).

To obtain a general linear dispersion relation, we use a relativistic cold fluid model that neglects pressure perturbations. Hence the dispersion relation for a purely transverse mode ($\vec{k} \cdot \vec{E} = 0$) is given by (see Appendix B):

$$\omega^2 - k^2c^2 - \sum_{a=1}^{a=n} \frac{\omega_{a\alpha}^2}{\gamma_{a\alpha}} - k \sum_{a=1}^{a=n} \frac{\omega_{a\alpha}^2}{\gamma_{a\alpha}} \frac{v_{a\alpha}}{\omega - \vec{k}\cdot\vec{v}_{a\alpha}} + \sum_{a=1}^{a=n} \frac{\omega_{a\alpha}^2}{\gamma_{a\alpha}} \frac{\beta_{a\alpha}^2}{\left(\omega - \vec{k}\cdot\vec{v}_{a\alpha}\right)^2} \left(\frac{\omega^2}{c}\left(1 - \frac{k^2c^2}{\omega^2}\right)\right) = 0 \tag{3.8}$$

By assuming $\vec{k} \cdot \vec{v} = 0$, we obtain a reduced dispersion relation, which can then be written as :

$$\omega^2 - k^2c^2 - \sum_{a=1}^{a=n} \frac{\omega_{a\alpha}^2}{\gamma_{a\alpha}} - \sum_{a=1}^{a=n} \frac{\omega_{a\alpha}^2}{\gamma_{a\alpha}} \frac{\beta_{a\alpha}^2}{\omega^2}(\omega^2 - k^2c^2) = 0 \tag{3.9}$$

We consider that $\omega = i\,\Gamma_{CFI}$ and $|\Gamma_{CFI}|^2 \ll k^2c^2$. Thus, Eq. (8) can be rewritten as :

$$k^2c^2 + \sum_{a=1}^{a=n} \frac{\omega_{a\alpha}^2}{\gamma_{a\alpha}} = \sum_{a=1}^{a=n} \frac{\omega_{a\alpha}^2}{\gamma_{a\alpha}} \beta_{a\alpha}^2 \frac{k^2c^2}{\Gamma_{CFI}^2} \tag{3.10}$$

as:

$$\Gamma^2_{CFI}[1/\omega^2_{a\alpha}] = \frac{\sum_{a=1}^{a=n} \frac{2n_{a\alpha}\beta^2_{a\alpha}}{\gamma_a}}{1 + \frac{2}{\tilde{k}^2}\sum_{a=1}^{a=n} \frac{n_{a\alpha}}{\gamma_a}} \tag{3.11}$$

Equation (10) shows that the finite energy spread will not suppress the instability. The main contribution to the growth rate comes from the particles with lower energies, which, by having lower relativistic masses can react quicker to the initial perturbations.

In order to simplify the analysis, and without losing generality, we now consider a case of two fireball beams (a = 1, 2 ; $\alpha = e^-, e^+$) propagating into opposite direction. The reduced dispersion relation given by Eq. (10) can then be written as :

$$\Gamma^2_{CFI}[1/\omega^2_{a\alpha}] = \frac{\frac{2n_{1\alpha}\beta^2_{1\alpha}}{\gamma_1} + \frac{2n_{2\alpha}\beta^2_{2\alpha}}{\gamma_2}}{1 + \frac{2}{\tilde{k}^2}\left(\frac{n_{1\alpha}}{\gamma_1} + \frac{n_{2\alpha}}{\gamma_2}\right)} \tag{3.12}$$

The growth rate of CFI due to ultra-relativistic neutral plasma attains its maximum growth rate when $\vec{k} \to \infty$, for which :

$$\tilde{\Gamma}_{CFI} = \sqrt{\frac{2n_{1\alpha}\beta^2_{1\alpha}}{\gamma_1} + \frac{2n_{2\alpha}\beta^2_{2\alpha}}{\gamma_2}} \tag{3.13}$$

To confirm our theoretical predictions, we have performed numerical simulations considering the propagation of two fireball beams with energy distribution given by $\gamma_b = \delta(\gamma - 300) + \delta(\gamma - 700)$ ($\gamma_b = 350, 700$) beams into the plasma. Figures 3.8 (a)-(b) show the temporal evolution of the beam electrons density for $\Delta p_x/\gamma_b = 0.13$ (Fig. 3.8(a)) and for $\Delta p_x/\gamma_b = 0.29$ (Fig. 3.8 (b)). The initial energy spectra of these two beams are shown in Fig. 3.8 (c). Figure 3.8 (d) shows the comparison of the magnetic field energy evolution. The blue curve shows the growth of magnetic field energy generated by the fireball beam with energy spread $\Delta p_x/\gamma_b = 0.29$, while the red curve is associated with the lower energy spread $\Delta p_x/\gamma_b = 0.13$.

The simulation growth rate ($\Gamma/\omega_p \simeq 2.8 \times 10^{-2}$; shown by dotted black line in Fig. 3.8 (d)) is consistent with the theoretical growth rate predicted for the purely transverse CFI [109, 110]. We notice that one to one comparisons with the simulation growth rate are non-trivial. We speculate that the differences are probably due to the finite beam size and non-uniform density profile in the transverse directions. We have performed additional simulations, which confirmed that numerical results converge to theoretical predictions as simulations considered progressively wider beams. In fact to the best of our knowledge, the excitation of these modes for finite length finite-width modes has not been investigated. Thus, this work also motivates further theoretical developments that could predict the exact growth rate for non-uniform

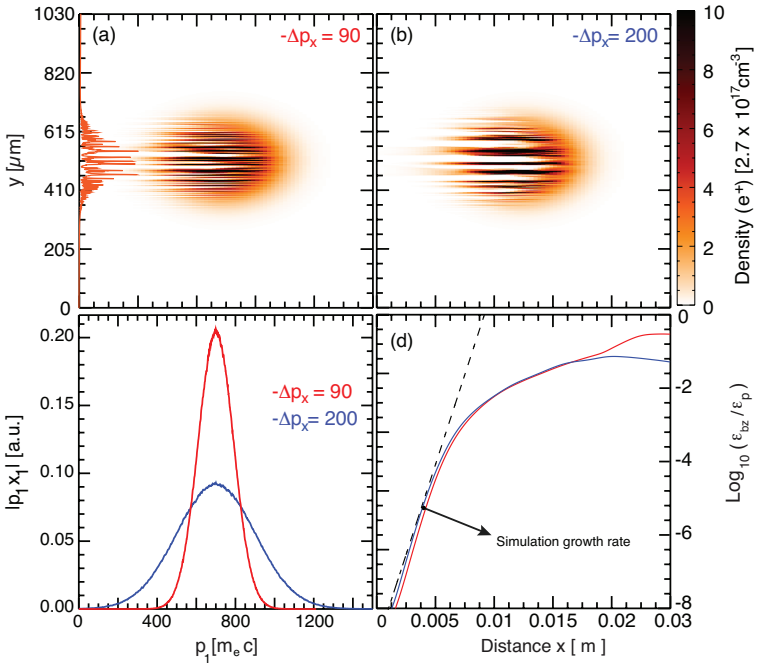

FIGURE 3.8: (*a*) -(*b*) Temporal evolution ($t = 705.60\ [1/\omega_p]$) of positron density exhibits the filaments for energy spread $\Delta p_x = 90, 200$ (*c*) (Color) the spectrum of two different energy spread (*d*) The solid line represents the simulation growth rate of CFI for different energy of beam.

density profiles. However, this discussion does not prevent the main purpose of this section, namely, the energy spread naturally present in laser-produced fireball beams will not prevent the CFI to occur.

3.6 PIC SIMULATIONS OF THE LEPTONIC BEAM (400MeV) DYNAMICS IN A BACKGROUND ELECTRON-ION PLASMA

Exploring laboratory surrogates capable of reproducing these mechanisms under controlled conditions is a promising path to gain physical insights that would be otherwise inaccessible. Recent experimental developments [80] promise to make this exploration possible. The generation of quasi-neutral electron-positron fireball beams, with maximum energy $\simeq$ 400 MeV (average fl $\sim$ 15), has been achieved in a laser-plasma accelerator. These beams have large energy spreads, they have a finite length and transverse size, and have small charge. Further details of experimental results can be found in Sarri *et. al.* [80]. In order to the check the validity of the experiments, we carried out three-dimensional (3D) particle-in-cell (PIC) simulations using OSIRIS [39].

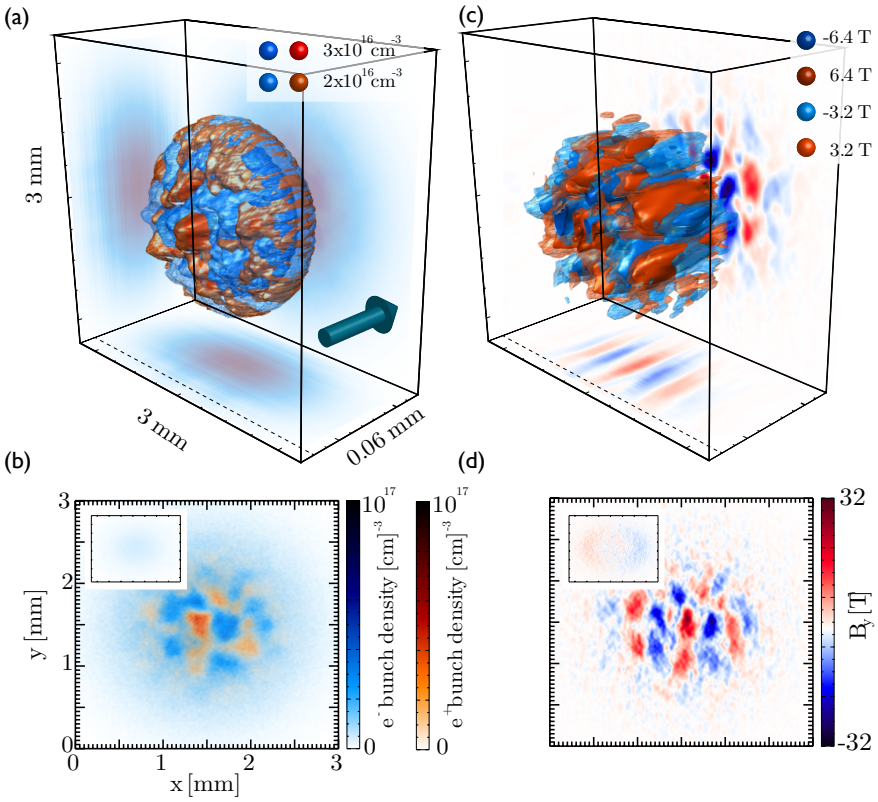

FIGURE 3.9: Simulation results of the propagation of a fireball bunch in a plasma. The arrow indicates the bunch propagation direction. (a) electron (blue) and positron (red) density isosurfaces showing growth of the Weibel instability at the back of the bunch. (b) Magnetic field (B_y) filaments due to the Weibel instability,where the B_y lies on the plane transverse to bunch propagation direction. The insets in (c) and (d) show the electron density and magnetic field corresponding to the propagation of a purely electronic fireball bunch.

Simulations used a moving window with dimensions $1.5 \times 100 \times 100\ (c/\omega_p)^3$ divided into $75 \times 1000 \times 1000$ cells with $2 \times 1 \times 1$ particles per cell for plasma electrons and for fireball particles. A charge-neutral fireball constituted by electrons and positrons was initialized at the entrance of the plasma with $n_0 = 10^{16}$ cm^{-3}. The density profile for electrons and positrons is given by $n_b = n_{b0} \exp\left(-\xi^2/\sigma_\xi^2 - r^2/\sigma_r^2\right)$ where $n_{b0} = 10\ n_0 = 10^{17}$ cm^{-3}, $\sigma_\xi = 0.22\ c/\omega_p = 11.7\ \mu$m and $\sigma_r = 10\ c/\omega_p = 530\ \mu$m are the bunch peak density, length and transverse waist respectively. The bunch transverse energy spread is $\langle p_r \rangle = 7\ m_e c$ with relativistic factor $\gamma = 700$ such that the fireball divergence is 0.01 mrad.

Simulation results are illustrated in Fig. 3.9 of fireball beam propagation through a denser e^--ion plasma, showing the growth of the Weibel/current filamentation instability from the back to the front of the bunch illustrating the spatial-temporal nature

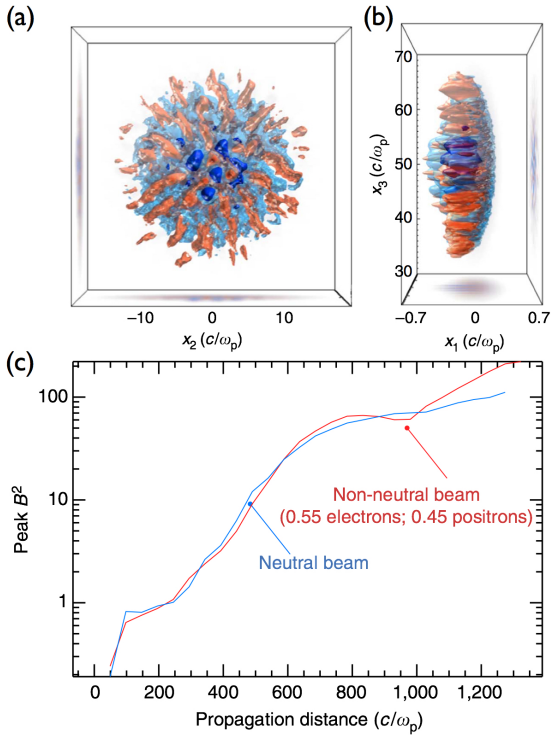

FIGURE 3.10: Simulation results of the propagation of a fireball bunch through an e^--ion plasma. The first row depicts the results for a perfectly neutral beam (50% electrons and 50% positrons). (a,b) depict the results for an analogous simulation, with the only difference that now the positrons account only for 45% of the beam. The frames show slices of the electron (blue) and positron (red) spatial distribution. (c) Comparison between the magnetic field growth for the case of a purely neutral beam (blue) and a slightly asymmetric beam (45% of positrons, red). For what concerns the plasma dynamics, the two cases are virtually undistinguishable.

of this instability. The instability leads to the formation of electron and positron filaments with thicknesses of $2-4\ c/\omega_p\ =\ 100-200\ \mu$m (Fig. 3.9a). The filaments from fireball electrons/positrons are located in complementary regions without positrons/electrons (Fig. 3.9b). This leads to a current imbalance and generation of magnetic field filaments (Fig. 3.10c) with maximum amplitudes in excess of 40 T at the middle of the bunch. Magnetic field filaments are also clearly visible in the plane transverse to the propagation direction (Fig. 3.9d). At early times, the simulations show that the transverse scale length of the filaments is even shorter than the initial beam skin depth. To further understand the impact of charge neutrality on the instability onset, additional 3D simulations were performed using a purely electron bunch with the same characteristics. In this case, the electron bunch generates plasma wakefields, and neither filamentation of the beam (insets in Fig. 3.9 b) nor the generation of

strong magnetic fields (inset Fig. 3.9 d) are observed. These results corroborate the expectation that current filamentation instability growth can be controlled by changing the beam overall total charge and it is maximized for a purely neutral e^-/e^+ plasma.

Finally, we performed an additional 3D PIC simulation devoted to study whether a slight charge imbalance in the e^-/e^+ plasma could result in a change in the plasma dynamics if compared with the idealized perfectly neutral plasma scenario shown in Fig. 3.10. We have thus maintained exactly the same conditions as the other simulation, with the only difference is that now the positron account for 45% of the plasma population, in order to match the experimental findings more closely [80]. The obtained spatial distribution of the e^-/e^+ plasma after propagation through the background electron/ion plasma is shown in Fig. 3.10 a,b, indicating essentially no difference if compared with the purely neutral case. This statement is corroborated by the growth of magnetic fields due to CFI. This is plotted in Fig. 3.9 c that shows virtually the same magnetic field growth for the purely neutral case (blue line) and for the slight charge imbalance (red).

3.7 SUMMARY

In summary, the growth and saturation of an ultra-relativistic beam propagating through plasma have been investigated using particle-in-cell (PIC) simulations. We have shown that short fireball beams, i.e beams shorter than the plasma wavelength, interacting with uniform plasmas lead to the growth of the CFI. For typical parameters available for experiments, the instability can generate strong transverse magnetic field on the order of the MGauss. We found that in typical laboratory settings, the incoming fireball beam filamentation saturates after 10 cm of propagation for the SLAC parameters [102], while for the laser-plasma generated fireball beam produced recently [80] it saturates after 4.4 cm.

We have demonstrated that the beam density needs to be higher than the background plasma density to suppress the growth of the competing OBI instability, which leads to the growth of electrostatic modes (instead of electromagnetic). Beams with lower peak densities will then drive the OBI, which results in tilted filaments and the generation of mostly electrostatic plasma waves. We have also shown that the beam emittance needs to be minimized, reducing transverse beam defocusing effects, which can shut down the CFI or the OBI if the beam defocuses before these instabilities grow. We have also extended our numerical studies to investigate the effect of finite fireball energy spreads on the growth of CFI, and showed that the energy spreads of currently available fireball beams allow for the growth of CFI in the laboratory.

In conclusion, we have identified the factors for the generation of strong magnetic fields via CFI. We expect that the results will influence our understanding of astro-

physical scenarios, by revealing the laboratory conditions where these effects can be studied.

CHAPTER 4

INFLUENCE OF PLASMA INSTABILITIES ON INTERPENETRATING PLASMA CLOUDS AS A TEST FOR ELECTROMAGNETIC DARK MATTER SELF-INTERACTIONS

4.1 INTRODUCTION: THE MYSTERY OF DARK MATTER (DM)

Our Milky Way contains approximately 10^{11} stars with total mass $\sim 5 \times 10^{10} M_{\odot}$, where $M_{\odot} = 2.99 \times 10^{10}\, kg$ is a unit solar mass, with a radius 10 kpc and with height of ~ 0.5 kpc. The circular velocity of the stars is $v_c(r) = (GM/r)^{1/2}$, where M is the enclosed mass, r is the radial distance, and G is the gravitational constant. At the distances beyond Galactic disk ($r \geq R_{disk}$), the total mass in the disk M should remain constant following Gauss's law. Instead, the observational findings indicate that the circular velocity curve flattens out at these distances, implying that $M(r)\, \alpha$ r suggesting a hidden component of matter beyond the visible matter, known as "dark" matter [111–115]. Dark matter (DM) contributes approximately 23 % the energy density of the Universe, with an abundance about five times as large as that of baryonic matter. It neither emits nor absorbs light or any other electromagnetic radiation at any significant level. The DM can only be observed via gravitational effects: galactic rotation curves, gravitational lensing, cosmic microwave background [116, 117]. Having been observed via only gravitational interactions, we know very little about the underlying particle physics of dark matter [118]. A huge array of theoretical possibilities remains open, spanning a 50 order-of-magnitude mass range from $\sim 10^{-22}$ eV to $\sim 10^{19}$ GeV (assuming dark matter is a new type of particle). Dark matter could have a wide vari-

ety of possible non-gravitational interactions both with itself and with other particles although all we can currently say is that they must be weak enough to have evaded observation [116,117]. Discovering such interactions would be a huge leap forward in understanding dark matter, and is one of the biggest goals of modern particle physics.

4.1.1 How do they interact?

Interestingly, as we explore in this paper, the most minimal type of dark matter interaction can have rich astrophysical consequences over the entire allowed mass range [118,119]. An unbroken U(1) gauge force, similar to electromagnetism but acting only between dark matter particles, would mediate long-range dark-matter self-interactions. We refer to such a force as *dark electromagnetism* (dark-EM) [120,121]. This is a very natural possibility that arises in a wide range of underlying dark matter models [122–125]. The stability of dark matter constrains these models as the conservation of dark-EM charge could forbid dark matter decay. In general, constraints on this scenario or observable consequences are of broad interest and merit thorough study. Assuming the interactions are weak enough not to bind dark matter particles together, dark matter would then consist of a net-neutral plasma of dark-EM charged particles. In this paper we investigate the effects this would have on halo dynamics.

4.1.2 Dark-matter could interact due to the presence of dark-charge particles

The dynamics of dark matter halos is the natural place to observe dark matter self-interactions. A recent observation of the "Bullet Cluster" (1E 0657-558), where a collision between a sub-cluster and the main cluster confirmed that the dark matter halo of the subcluster passes through the main cluster with no visible offset between the stars and the DM, thus indicating weak self-interactions. The seemingly clean passage of one halo through another in the "Bullet Cluster" led to well-known bounds being placed on $2 \to 2$ hard scattering (i.e. short-ranged interactions) [125,126]. Dark-EM also gives rise to conceptually different effects which result in far stronger bounds, due to the collective dynamics of the dark-matter plasma. The dark-EM interaction would act as a $N \to N$ rather than a $2 \to 2$ scattering process, where N is extremely large. The bounds from $2 \to 2$ scattering require that a typical dark matter particle has never undergone a hard scattering [122,123]. This indicates that the dark-matter plasma is in the "collisionless" regime [124,125]. Under this hypothesis, we shall see whether the most minimal type of dark matter self-interaction via a new long-range force analogous to the electromagnetic interaction in the standard model could have impact on the DM self-interactions. This possibility raises the question of whether plasma instabilities may have significant impact on galaxy and cluster dynamics. Resolving

this will determine whether or not such an interaction is consistent with current observations, and whether plasma instabilities may have significant impact on galactic dynamics.

4.1.3 Pedagogical description of plasma instabilities known in literature

In this work, we consider the simple possibility of an electromagnetic self-interaction between two collisionless dark matter plasma slabs. The equations that govern DM self-interactions is identical to that of a collisionless e^-, e^+ plasma. Collisionless plasma dynamics is both a well-studied field and an area of active research with rich dynamics that are still not fully understood. It is known that two counterpropagating plasmas are subjected to the several microinstabilities that generate the growth of electromagnetic fields, involving transverse and parallel modes. The full unstable wavenumber k spectrum has been intensively studied in the cold plasma limit [40,94,127,128]. There are three main dominating instabilities which exist with different wave-vectors with respect to the flow: The two-stream instability (TSI), which has a wave-vector aligned with the flow, is driven by the two peaked nature of the velocity distribution [127]. The anisotropy in the velocity spread in different directions (larger along the flow direction) excites the Weibel/Filamentation instability (WI/FI) with a wave-vector normal to the flow [30]. A hybrid of these two modes, with a wave vector with and angle oblique to the flow, is known as the oblique instability (OBI) [128].

Plasma instabilities are well understood analytically in the linearized regime with small perturbations to an infinite homogeneous plasma. Furthermore, the theoretical estimates of linear growth of electromagnetic field generated via plasma instabilities, complemented by numerical simulations, have been well studied during the interaction of two plasma slabs [42,99]. The electromagnetic fields driven by these plasma instabilities will lead to bulk slowdown of the counterpropagating plasma slabs as long as there is sufficient time for the instabilities to grow. The exact time required before a significant slowdown occurs, however, depends on nonlinear effects not included in such analysis and can be only captured via numerical simulations, as performed in this paper. Our studies, therefore, can place a limit on the interaction strength.

The dimensionless quantities, $\alpha_B = U_B/\mathcal{E}_p$ and $\alpha_E = U_E/\mathcal{E}_p$ are the respective magnetic and electric equipartition parameters. Here the energy density of the magnetic fields ($U_B = \int B^2 dV$) and electric fields ($U_E = \int E^2 dV$) is normalized to the initial total kinetic energy density in the system $\mathcal{E}_p = \sum_\alpha \int n_{0\alpha} m_e v_{fl}^2/2 dV$, summing over each species α; in our case the number of species is $N_{SP} = 2, (e^-, e^+)$. Here m_e, $n_{0\alpha}$, v_{fl}, are the respective mass, density, and the velocity of the species, and V is the total volume of the two slabs. Above quantities will be used demonstrating the slowdown process that occurs during the interaction of two plasma slabs.

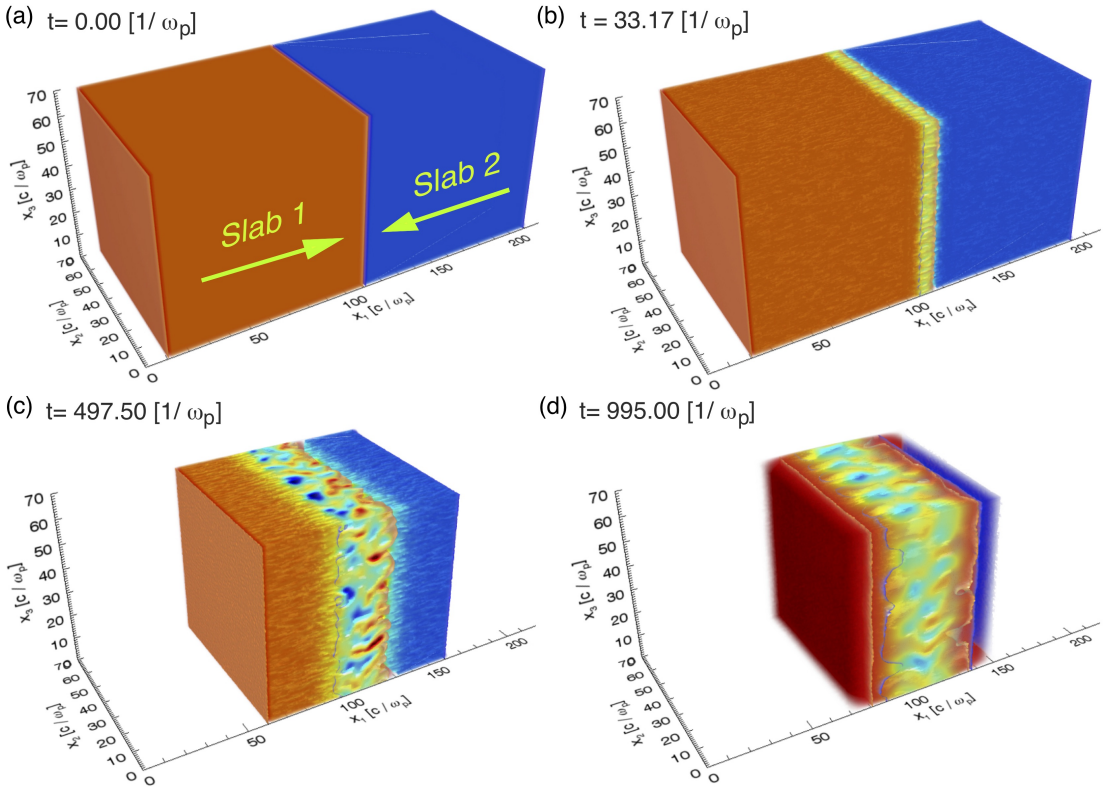

FIGURE 4.1: (color online) The temporal evolution of the e^- filament density for simulation R_1, where Slab 1 (orange) and Slab 2 (blue) are moving to the respective right and left at $t\omega_p = 0.0, 33.17, 497.50, 995.00$ (a)-(d). The green color represents where the plasma from both slabs overlap.

4.2 MODELING OF DARK-PLASMA INTERACTION WITH PIC

In order to put a limit on the strength at DM self-interactions, we simulate the interaction of two initially unmagnetized electron-positron plasma slabs propagating towards each other. Two and three dimensional numerical simulations were performed with the fully relativistic, massively parallel, particle-in-cell (PIC) framework OSIRIS [70, 71]. The box has dimensions of $2.2L \times L_\perp^2$ with a resolution Δx, where L is the length of the plasma slab and $L_\perp$ is the transverse dimension. The two slabs, shown in Fig. 4.1a, consist of a plasma with uniform density n_0 moving to the right (red) between $x_1 = 0.1L - 1.1L$, and moving to the left (blue) between $x_1 = 1.1L - 2.1L$ with a bulk proper fluid velocity v_{fl}. We chose a step function density profile rather than Gaussian in order to maximize the interaction time where the plasmas are unstable. We ran each simulation for one crossing time $\tau_c = L/v_{fl}$ with a temporal resolution $\Delta t \approx 0.98\Delta x/\sqrt{D}c$, where D is the number of dimensions of the simula-

tion.

We performed 3D simulations (R_1) with 4 particles per cell for each plasma species, and 2D simulations (R_2, R_5, and R_6) with 16 particles per cell for each plasma species, all with $L = 100[c/\omega_p]$, $L_\perp = 70[c/\omega_p]$, and $\Delta x = 0.1[c/\omega_p]$, where c/ω_p is the electron skin depth, c the speed of light, $\omega_p = \sqrt{4\pi e^2 n_0/m_e}$ the electron plasma frequency, e the elementary charge, and m_e the electron mass. The rest of the simulations are 2D with 16 particles per cell for each plasma species. Simulations (R_3 and R_7) have $L = 5[c/\omega_p]$, $L_\perp = 5[c/\omega_p]$ with resolution $\Delta x = 0.01[c/\omega_p]$, and ($R_4$ and R_8) have $L = L_\perp = 0.02[c/\omega_p]$ with $\Delta x = 0.0004[c/\omega_p]$.

We performed simulations with respective flow and thermal velocities $v_{fl}/c \in [0.01 - 0.1]$ and $v_{th}/c \in [0.001 - 0.01]$ which have been listed in the table 4.1 and 4.2. Absorbing boundary conditions have been used for the fields and the particles in the direction parallel to the flow velocities and periodic in the transverse direction. To suppress the numerical heating, a fourth order interpolation scheme has been used together with a 5-pass filter to evaluate current and fields. Larger transverse box sizes, higher spatial and temporal resolution and the higher number of particles per cell were tested, showing overall convergence.

4.3 INTERPRETATION OF SIMULATION RESULTS

Here we report the three dimensional simulation results of the most representative run (R_1). In Fig. 4.1, we show four representative times over the period of one crossing time $\tau_c = L/v_{fl}$. During this time, the plasmas penetrate (see in Fig. 4.1b), filament (see in Fig.4.1c), and slow down significantly by τ_c (see in Fig. 4.1d). The slowdown and isotropization of the velocity distribution occurs at three time scales, that of the two-stream/oblique instability, the Weibel instability, and the crossing time of the plasma slabs.

At the earliest stage, the overlapping plasma slabs result in two peaks in velocity space in opposite directions, which drives the oblique instability. The oblique instability generates electric and magnetic fields at the expense of the initial bulk energy: a fraction of the initial kinetic energy ϵ_p is transferred into the different components of longitudinal E_1 and transverse electric E_2, and magnetic fields B_3 shown in Fig. 4.2a. In Fig. 4.2a, we present the temporal evolution of the electric and magnetic field energy. Throughout this study, when we refer to the oblique instability, the two-stream component of the oblique instability dominates. The oblique instability (not just two-stream) can be seen in Fig. 4.2a, since the magnitude of the longitudinal E_1 and the transverse electric fields E_2 (unique to the oblique instability) are about equal. During the linear stage of the instability at time $t\omega_p \approx 13$, the transverse electric fields E_2 are greater than the transverse magnetic fields B_3, consistent with the

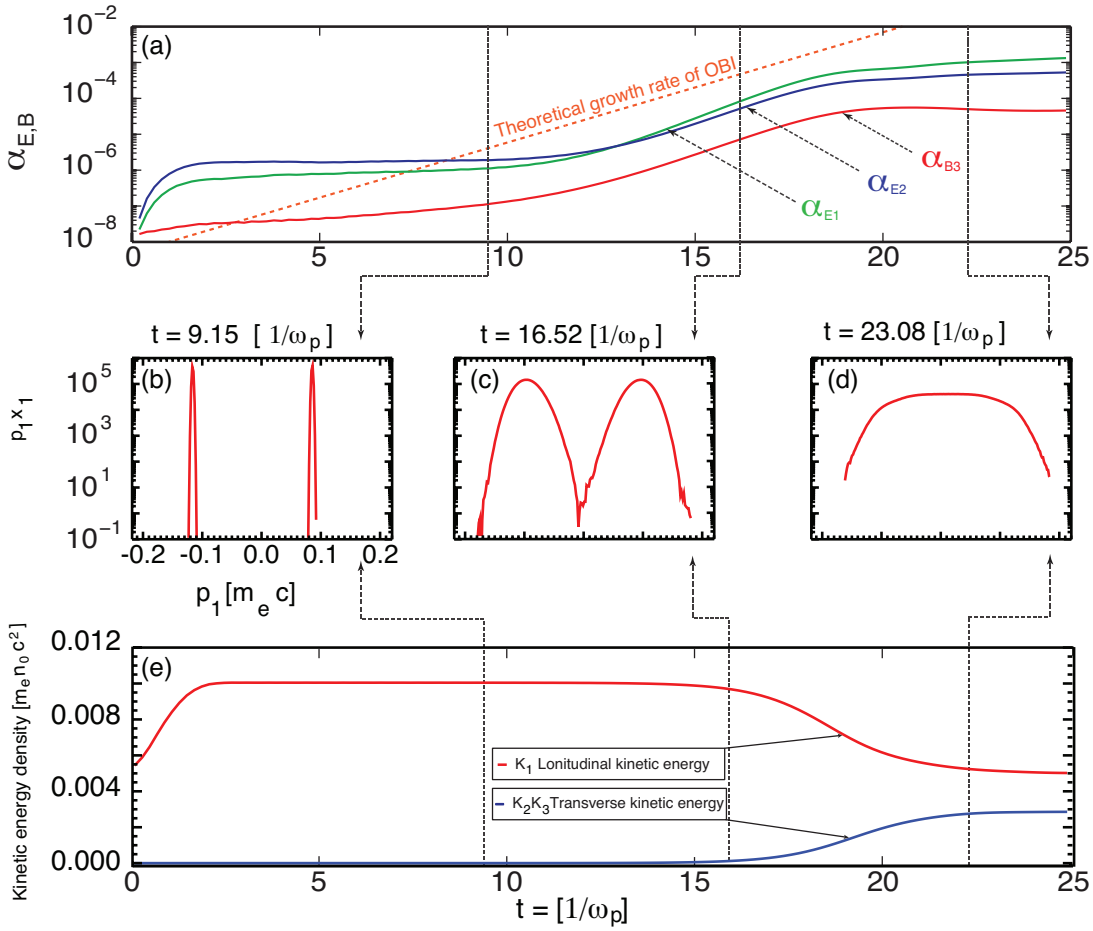

FIGURE 4.2: (a) Temporal evolution of the total electromagnetic energy of the system for the 3 components E_{x1} (blue), E_{x2} (green), and B_{x3} (red) in their normalized form $\alpha_{E,B}$. Panels (b)-(d) show the electron distributions of momentum along the x_1 direction calculated between $x_1 = 109.9 - 110.1\,[c/\omega_p]$ over all x_2, for $t\,\omega_p = 9.15, 16.52$, and 23.08. Panel (e) shows the temporal evolution of the mean kinetic energy density of electrons in slab 1 over the same region (K_1 (red) and $K_2 = K_3$ (blue), where $K_i \equiv \langle m_e n v_i^2/2 \rangle / m_e n_0 c^2$. K_1 is longitudinal kinetic energy in the direction of flow velocity and, K_2 and K_3 are transverse)

modes of the oblique instability. The theoretical growth rate of the oblique instability $\Gamma_{TS} \approx \omega_p/\sqrt{2}$ [94] shown in Fig. 4.2a (red dotted), matches well with the simulation result.

To further illustrate that the instability acts like the two-stream instability, we examine the evolution of the distribution $f_0(p_1)$ through the course of the growth and saturation of the oblique instability in the region x1 $= [109.9 - 110.1]\,[c/\omega_p]$. At $t\,\omega_p = 9.15$, once the two slabs overlap, the two peaks in velocity space in opposite directions is illustrated in Fig. 4.2b. During the interaction, the electric field grows lin-

early due to the oblique instability causing a strong heating which broadens the initial particle distribution (see Fig. 4.2c). After the linear phase, at time $t\,\omega_p = 23.08$, the instability saturates and the distribution is completely thermalized (see Fig. 4.2d). Here the free energy that drives the oblique (two-stream) instability is no longer present. During the linear phase of the instability, the transverse electric field accelerates the particles in the transverse directions x_2 and x_3. The particles slow down in the longitudinal (x_1) direction, such that the total kinetic energy does not change much, as only 0.1 % of the initial flow kinetic energy is converted into field energy, see in Fig. 4.2(a,e). In this process, the kinetic energy becomes significantly isotropized (see Fig. 4.2e); each of the components of the kinetic energy density approach a number close to 0.004 $[m_e n_0 c^2]$.

Here we estimate the typical timescale for isotropization of the kinetic energy in D dimensions solely due to the electric fields. Assuming that the total kinetic energy does not change, complete isotropization of the velocity distribution will occur once the change of velocity along the directions perpendicular to the flow is

$$\Delta v = \sqrt{\langle v_i^2 \rangle} \approx 1/\sqrt{D} v_{fl}. \tag{4.1}$$

Each component of the electric field can be expressed as $E_i = \omega_p m_e / e \sqrt{\alpha_{E,loc} N_{sp}/D}\, v_{fl}$, where $\alpha_{E,loc} \equiv E^2 / m n_0 N_{sp} v_{fl}^2/2$ is the local electric equipartition parameter. From the Lorentz equation:

$$\frac{\Delta v}{\Delta t} = -\frac{e}{m_e} E_i \tag{4.2}$$

by substituting $\Delta v / v_{fl}$ and E_i, we can estimate the isotropization time due to electric field:

$$\Delta t_{\alpha_E} \omega_p = \sqrt{\frac{1}{\alpha_{E,loc} N_{sp}}} \approx 5.85, \tag{4.3}$$

where $\alpha_{E,loc}$ is calculated at $t\omega_p = 16.52$, when the α_E begins to saturate (Fig.4.2a$\alpha_{E,loc}$) reaches a maximum $\alpha_{E,loc} = 1.46\%$ at $x_1 = 109.8\,[c/\omega_p]$. This timescale is in good agreement with the simulation result (see Fig. 4.2e between $t\omega_p = 16.52$ and 22.37. Note that further isotropization occurs after $t\omega_p = 25.00$.

The Weibel instability is driven by a temperature anisotropy [30]. Although the oblique instability thermalizes, and significantly isotropizes the plasma velocity distribution, an anisotropy remains (see Fig. 4.2e). At about $t\omega_p = 40.00$, the magnetic field energy grows at a rate consistent with the theoretical growth rate ($\Gamma_{WI}/\omega_p \approx v_{fl}/\sqrt{2} \approx 0.07$ [94]) indicated by the red dotted in Fig. 4.3a. The instability saturates at about $t\omega_p = 100.00$, and the magnetic fields are responsible for the further isotropization of the slabs. After saturation, the magnetic field strength

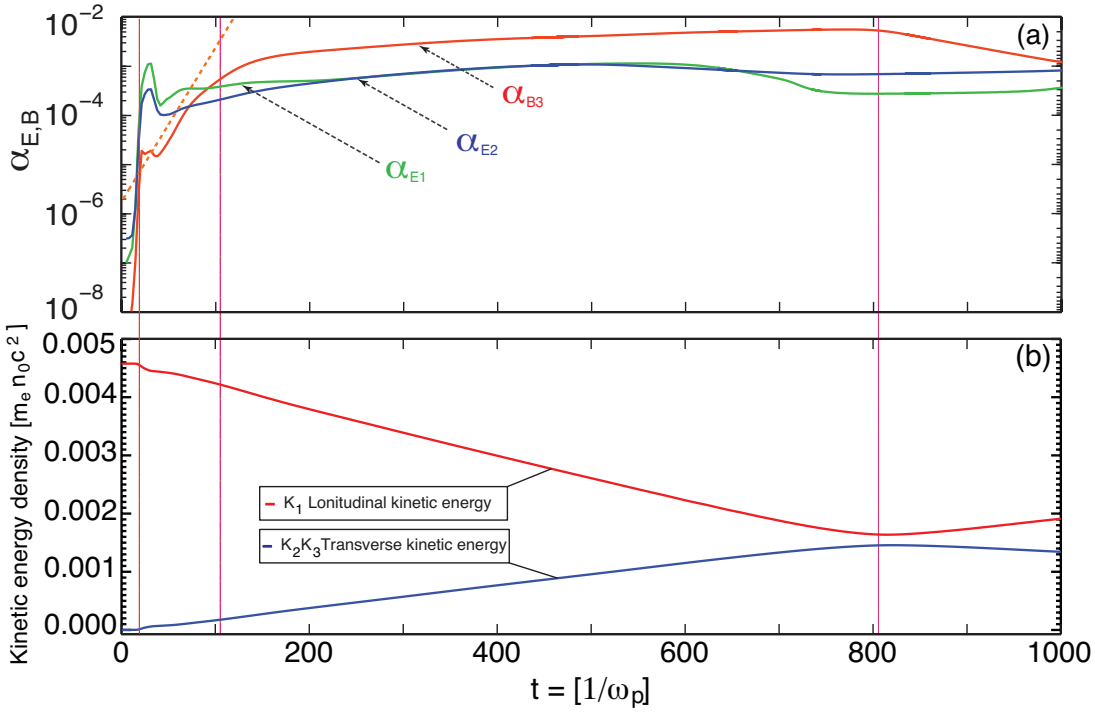

FIGURE 4.3: (a) Temporal evolution of the total electromagnetic energy of the system for the 3 components E_{x1} (blue), E_{x2} (green), and B_{x3} (red) in their normalized form $\alpha_{E,B}$. Dashed lines indicate $\Delta t_{\epsilon E}, \Delta t_{\epsilon B}$, and the time plotted in Fig. 4.4d when the maximum velocity along the plasma slab drops below $0.5 v_{fl}$ (the slabs have transited past each other). Panel (b) shows the temporal evolution of the mean kinetic energy density of electrons in slab 1 (K_1 (red) and $K_2 = K_3$ (blue), where $K_i \equiv \langle m_e n v_i^2/2 \rangle / m_e n_0 c^2$, averaged over all x_1, x_2. K_1 is longitudinal kinetic energy in the direction of flow velocity and, K_2 and K_3 are transverse). The red dotted line is the theoretical growth rate of the Weibel instability.

grows linearly, between $t\omega_p = 200.00 - 800.00$, as the shock front propagates across the plasma slab. The magnetic field isotropizes the kinetic energy by bending the trajectories such that K_1 is converted to K_2 and K_3 see Fig. 4.3b.

A similar method is adopted to calculate the istropization time due to the magnetic fields ($\alpha_{B,loc} = 0.3\%$ calculated from Fig. 4.4f at $x_1 = 109.8\,[c/\omega_p]$)

$$\Delta t_{\alpha_B} \omega_p = \sqrt{\frac{2}{D \alpha_{B,loc} N_{sp}}} \frac{c}{v_{fl}} \approx 105.4, \tag{4.4}$$

consistent with the saturation of the Weibel magnetic field at time $t\omega_p \approx 100.0$

Fig. 4.4a illustrates the formation and propagation of the shock front presented with the best fit solid line. As the slabs overlap, the density of plasma slabs increases from n_0 to $4n_0$ see Fig. 4.4b-d. The step region in the density shows a shock front which

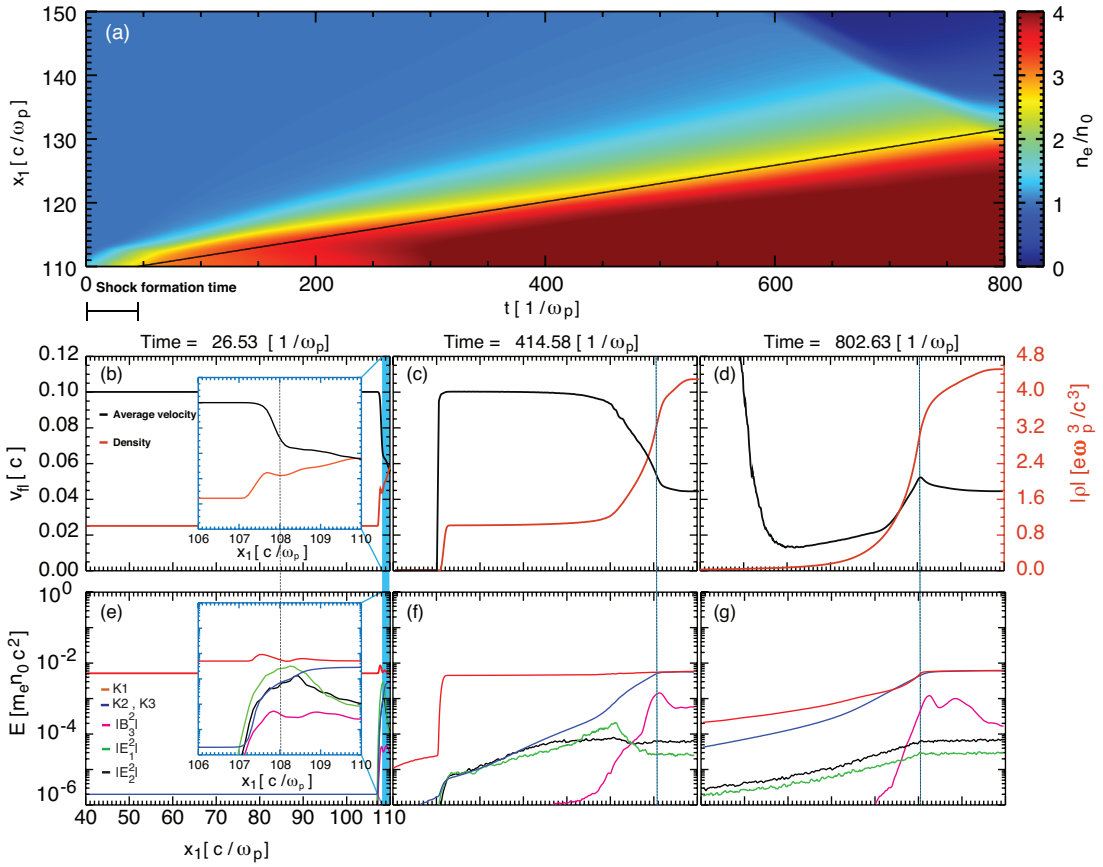

FIGURE 4.4: (color online) Panel (a) shows the evolution of the plasma density vs. time. The solid line indicates a line of best fit the shock front ($x_1 = t_0 + 0.0286\,c \times t$), where $t_0\omega_p$ is 110. Panels (b-d) show the spatial profiles of the average x_1 velocity of electrons with positive velocity (to the right) (black) and average density (red) averaged along the x_2 direction. Panels (e-g) show the energy densities of each component of the electromagnetic fields and the kinetic energy averaged along the x_2 direction. The black dotted line is the position of the shock front, and at $t\omega_p = 26.53$ where there is no shock, this represents the density front.

propagates at the average speed (0.0286 c) shown in Fig. 4.4 a. The shock develops fully once both the oblique (two-stream) and the Weibel instabilities have time to grow and saturate. The isotropization time ($\Delta t_{\epsilon_B}\omega_p \approx 105.4$, see Eq. 3, which is about equal to the Weibel saturation time), is consistent with the shock formation time $t_0\omega_p = 110$ shown in Fig. 4.4a.

The growth and saturation of both instabilities can be seen as a function of space, during various times, eventually leading to the total slowdown of the plasma slab. At early time (see Fig. 4.4e) the E-fields from the oblique instability begin to isotropize the kinetic energy and significant slowdown occurs (see Fig. 4.4b). The electric field of the oblique modes are coincident with the density front at $t\,\omega_p = 26.53$ (see Fig. 4.4b,e).

At this stage the shock is not yet formed.

As the plasma slabs overlap further, the Weibel instability begins to play role (see Fig. 4.4f). At $t\,\omega_p = 414.58$, the density front has become a fully formed shock. The slabs slow down in the shock region, as seen in Fig. 4.4(c,f) between $L = 80 - 100\,[c/\omega_p]$. This slowdown of v_{fl} across the shock is stronger than in Fig. 4.4b. In Fig. 4.4f, at the position $x_1 = 92.0[c/\omega_p]$, the electric field generated by the oblique instability contributes to the isotropization of the kinetic energy. The magnetic field generated by the Weibel instability, peaking at $x_2 = 102.0[c/\omega_p]$, further isotropizes the kinetic energy (until $K_1 \approx K_2 \approx K_3$). Assuming a steady state propagating shock front has been established (evidenced in 4.3a), and the flow velocity $v_{fl} = 0.1c$, the time between $x_1 = [90 - 100][c/\omega_p]$ can be estimated by 100 $[1/\omega_p]$, matching the Weibel saturation time.

At the transit time $t\omega_p = 802.63$, once the shock has traversed the entire slab (see Fig. 4.4d), the slowdown of the two slabs is completed. Fig. 4.4f shows the complete isotropization across the entire slab.

We determined two measures that can be used to quantify the slowdown of the plasma; the average velocity of the initially right moving electrons $v_{init} = \int_{-p}^{+p} pf(p)dp \,/\, \int_{-\infty}^{+\infty} f(p)dp$ (from the left slab only) (blue) and instantaneously right moving electrons $v_{inst} = \int_{0}^{+\infty} pf(p)dp / \int_{0}^{+\infty} f(p)dp$ (from both slabs) (red). We define a significant slowdown as $v_{init} < 0.46\,v_{fl}$, and $v_{inst} < 0.9\,v_{fl}$ to determine whether there is slowdown or not. At the transit time $t\omega_p = 802.63$, the velocities reach $v_{init} = 0.1444\,v_{fl}$ and $v_{inst} = 0.5\,v_{fl}$, a significant slowdown under both measures (Fig. 4.5a).

Note the slowdown of v_{inst} is consistent with the prediction that once isotropized $v_{inst} = \Delta v \approx 0.577 v_{fl}$, see Eq.1. Furthermore, a significant slowdown of the front of the plasma slabs (at the center of the box) is shown in the inset Fig. 4.5b. This occurs at a much shorter time scale $t\omega_p = 25$, the time scale of the two-stream/oblique instability.

The relative growth of the WI/OBI and the crossing time τ_c, which determines whether there can be a slowdown of the two plasma-slabs, depends on L, v_{fl}, and v_{th}. Now, we present simulation results varying these key parameters. As there is small difference between the 2D and 3D runs, in order to minimize the computational time, these simulations are done in 2D. To explore the influence of L and v_{fl} on the slowdown of the plasma slabs, we have performed 4 simulations listed in Table 4.1 varying these parameters, while keeping $v_{th} \ll v_{fl}$. This parameter space with each of the simulations is presented in Fig. 4.6.

For $L/v_{fl}\Gamma_W \geq 10$ we expect slowdown of the plasma caused by both the Weibel and oblique instabilities in the red shaded region shown in Fig. 4.6. This is confirmed for runs R_1 and R_2 which exhibit a significant slowdown. Even when this constraint is not satisfied, and only $L/v_{fl}\Gamma_{TS} \geq 10$, we expect a moderate slowdown caused by the oblique instability shown in Fig. 4.6 in the green shaded region. This is confirmed in R_3

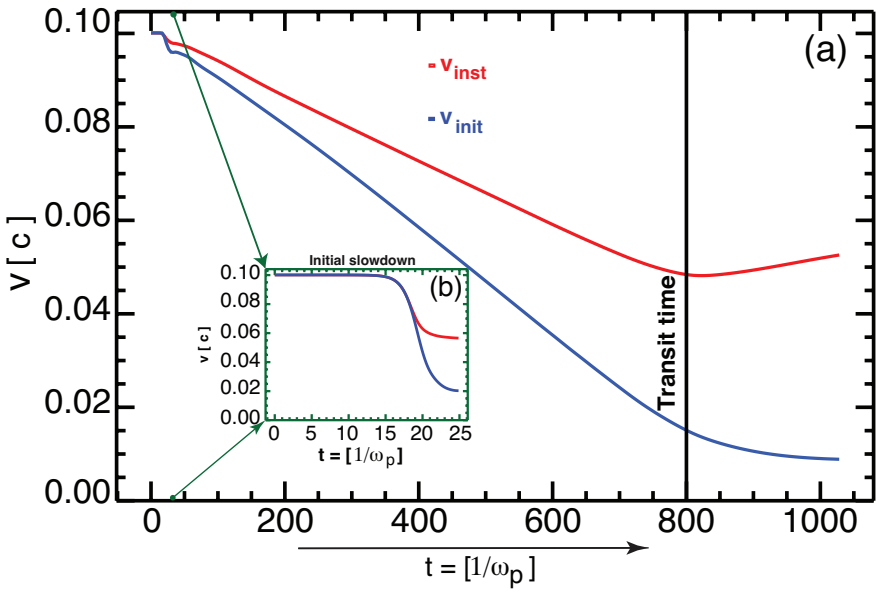

FIGURE 4.5: (a) (Color online) Temporal evolution of v_{init}, the average velocity over the entire simulation box of all electrons that were initially moving to the right (blue), and v_{inst}, the average velocity of all electrons moving to the right at time t (red) and (b) averaged between $x_1 = 110.3 - 110.5\,[c/\omega_p]$ over all x_2. The solid line is the time plotted in Fig. 4.4d when the maximum velocity along the plasma slab drops below $0.5v_{fl}$ (the slabs have transited past each other).

TABLE 4.1: Slowdown ($1 - v/v_{fl}$, where v is the final measured velocity) expected due to the two-stream/oblique or Weibel instability for various v_{fl} and L with cold slabs $v_{th}/v_{fl} = 0.1$.

Runs	v_{fl}/c	**L** $[\omega_p/c]$	**Cause**	$1 - v_{inst}/v_{fl}$	$1 - v_{init}/v_{fl}$
R_1	0.1	100	WI/OBI	0.5000	0.8556
R_2	0.01	100	WI/OBI	0.4680	0.8765
R_3	0.01	5	OBI	0.3490	0.5580
R_4	0.01	0.02	No slowdown	0.00171	0.000024

where there is moderate slowdown. However, if neither of these constraints are met, highlighted as the blue region in Fig. 4.6, no slowdown is expected. For simulation R_4, neither the oblique instability nor the Weibel instability has time to grow and there is no slowdown. For the cases where there is significant slowdown, the velocity is thermalized such that the new thermal velocity $v_{th}^{'} = v_{inst}$. For example for Run R_1, after the slabs have crossed they obtain a thermal velocity $v_{th}^{'} = 0.05$ ($T/m_ec^2 = 0.0025$).

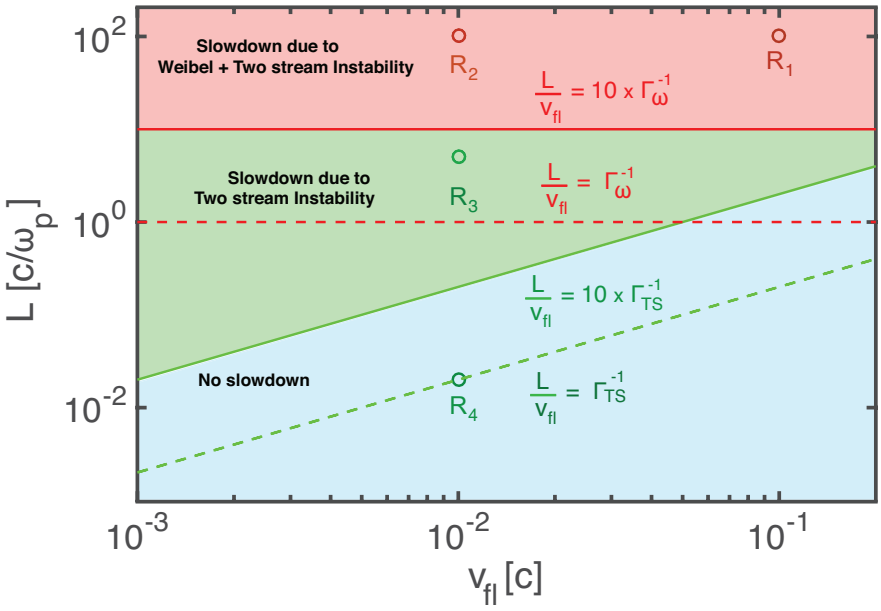

FIGURE 4.6: *Length of DM plasma slab vs initial velocity.* Parameter space showing the slowdown of DM slab is expected due to two-stream/oblique or by the Weibel instability. In the red region, both the Weibel and the two-stream/oblique instabilities are expected to lead to a significant slowdown. In the green region, only the two-stream/oblique instability should act to slow down the plasma. In the blue region slow down is not expected. The dashed red and green lines show where the growth rate of the respective Weibel and two-stream/oblique instabilities are equal to the rate at which the two slabs cross past each other. Significant slowdown is expected after a factor of 10 growth times, based on our predicted slowdown times $\Delta t_{\alpha B}\Gamma_W \approx 6.324$ and $\Delta t_{\alpha E}\Gamma_{TS} \approx 8.66$.

TABLE 4.2: Slowdown ($1 - v/v_{fl}$, where v is the final measured velocity) expected due to the two-stream/oblique or Weibel instability for various v_{fl} and L with warm slabs $v_{th}/v_{fl} = 1.0$.

Runs	v_{fl}/c	**L** $[\omega_p/c]$	**Cause**	$1 - v_{inst}/v_{fl}$	$1 - v_{init}/v_{fl}$
R_5	0.1	100	WI	0.3765	0.7020
R_6	0.01	100	WI	0.14287	0.9436
R_7	0.01	5	No slowdown	0.09592	0.5331
R_8	0.01	0.02	No slowdown	0.00012	0.00023

To understand the role of the initial thermal velocity of the slabs, we perform similar simulations with the set-up described in the above section, but with a significant thermal velocity ($v_{th} = v_{fl}$, as shown in Table 4.2. In a warm plasma ($v_{fl} \leq v_{th}$), the

two peak structure seen in Fig. 4.2b, which drives the two-stream/oblique instability, is not present due to significant thermal spread. However, slowdown can occur due to the Weibel instability for $L/v_{fl}\Gamma_W \geq 10$. Therefore, in this scenario, we do not expect a slowdown in both the green and the blue region where the plasma slabs $L(\omega_p/c)$ are smaller than 10. This is confirmed in runs R_7 and R_8. However, in the red region, for plasma length $L(\omega_p/c)$ greater than 100, we always expect slowdown. This is confirmed in runs R_5 and R_6.

4.4 Parametric estimate of bounds on Dark-EM

Based on our simulation findings, we put a very strong constraint on the parameter space (α_D, m_D) for DM particles. Here $\alpha_D \equiv e_D^2/\hbar c$ and m_D are the respective dark electromagnetic coupling constant and mass, and e_D is the dark electromagnetic charge of the particle. Our numerical simulations so far have shown that for sufficiently large L the DM slab will slow down due to the Weibel and oblique instabilities. Given that we have estimates for $L \approx 100kpc$, as well as $v_{fl} \approx 0.1\,c$, $m_D \approx 1\,TeV$, and the mass density $\rho_D \approx 0.01GeV/cm^3$ [120–123, 129], we can recast our limit of a maximum L to evade slowdown to a limit on the coupling strength $\alpha_D(\ll 1)$

First we estimate coupling constant based on the Weibel growth. We found a significant slowdown occurs if the length $L > 10\,\Gamma_W^{-1} v_{fl}$.

$$\frac{L\Gamma w}{10 v_{fl}} = \frac{L}{10 v_{fl}} \left(\frac{4\pi\rho_D \alpha_D \hbar c}{m_D^2}\right)^{1/2} \frac{v_{fl}}{c} \tag{4.5}$$

Recast in terms of α_D this is equivalent to the constraint

$$\alpha_D < L^{-2} \rho_D^{-1} m_D^2 \left(\frac{4\pi\hbar}{100}\right)^{-1} \tag{4.6}$$

Using our estimates for the parameters, we find a quantitative limit on α_D in engineering form

$$\begin{aligned} \alpha_D < 4.2355 \times 10^{-25} \left(\tfrac{L}{100kpc}\right)^{-2} \left(\tfrac{\rho_D}{0.01GeV/cm^3}\right)^{-1} \\ \times \left(\tfrac{m_D}{1TeV}\right)^2 \end{aligned} \tag{4.7}$$

Similarly, we can estimate coupling constant due to the oblique instability. The limit on L for the oblique instability is

$$\frac{L\Gamma_{TS}}{10 v_{fl}} = \frac{L}{v_{fl}} \left(\frac{4\pi\rho_D \alpha_D \hbar c}{m_D^2}\right)^{1/2} \tag{4.8}$$

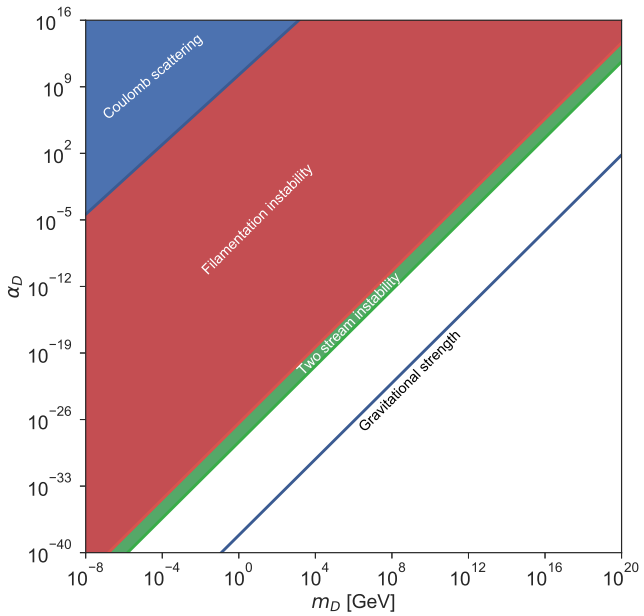

FIGURE 4.7: Constraints on the dark electromagnetic coupling constant α_D as a function of m_D. α_D must lie below the region (in blue) due to expected slowdown from Coulomb scattering, (in red) from filamentation, and (in green) from the two-stream/oblique instability. For reference, the dark electromagnetic coupling forces will be equal to the gravitational forces along the blue line.

which recast in terms of α_D is

$$\alpha_D < L^{-2} v_{fl}^2 \rho_D^{-1} m_D^2 \left(\frac{4\pi\hbar c^2}{100c}\right)^{-1} \tag{4.9}$$

and in engineering form is

$$\begin{aligned}\alpha_D < 4.2355 \times 10^{-27} \left(\tfrac{L}{100kpc}\right)^{-2} \left(\tfrac{\rho_D}{0.01GeV/cm^3}\right)^{-1} \\ \times \left(\tfrac{m_D}{1TeV}\right)^2 \left(\tfrac{v_{fl}}{0.1c}\right)^2\end{aligned} \tag{4.10}$$

Fig. 4.7 shows the two limits from Eqs. (4.7,4.10). In contrast, a much weaker bound on α_D has been established assuming a slowdown caused by Coulomb scattering [129]. For this limit the collision frequency

$$\nu = \left(\frac{4\pi\rho_D\alpha_D\hbar c}{m_D^2}\right)^2 \frac{m_D}{\rho_D} \frac{\ln(\Lambda_C)}{2\pi v_{fl}^3} \tag{4.11}$$

where $\ln(\Lambda_C)$ is the Coulomb logarithm, is comparable to the crossing time $\nu\tau_D = 1$, .

$$\begin{aligned} \alpha_D &< 1.9454 \times 10^4 \left(\frac{L}{100kpc}\right)^{-1/2} \left(\frac{\rho_D}{0.01GeV/cm^3}\right)^{-1/2} \\ &\times \left(\frac{m_D}{1TeV}\right)^{3/2} \left(\frac{v_f}{0.1c}\right)^2 \left(\frac{\ln(\Lambda_C)}{35}\right)^{-1/2} \end{aligned} \tag{4.12}$$

In the blue region, a slowdown due to Coulomb scattering is expected. In the red region, a slowdown due to the Weibel and oblique instabilities is expected. In the green region, a moderate slowdown due to the oblique instability is expected. In the white region, no slowdown is expected, consistent with observations. This establishes a strong upper bound on the the typical strength of any dark electromagnetic self-interaction. To emphasize how strong the bound on α_D this establishes, we also include a line where the strength of the dark electromagnetic force between two dark matter particles is equal in magnitude to the gravitational force. Larger α_D particles could potentially be explained by more complex theories which include an ionization fraction, where only a select few particles have this larger interaction [129].

4.5 Conclusion

In conclusion, using PIC simulation of the interpenetration of two e^-, e^+ plasma clouds, we established a strong upper bound on the strength of any dark electromagnetic self-interaction where the Dark-matter self-interaction strength $\alpha_{DM} \ll 1$. In case of the self-interactions of two cold dark plasmas clouds ($\mathbf{v_1} \geq \mathbf{u_{th}}$) lead to the generation of Weibel and Two-stream instability which deflects the particles trajectories such that the particles acquire transverse momentum. Hence, this process causes the slowdown due to Wiebel and Two-stream instability. We also have shown that for typical DM slab length much larger than $\mathbf{v\Delta t}$, DM particles lose half of its initial velocity. In the case of a hot plasma cloud ($\mathbf{v_1} \leq \mathbf{u_{th}}$), we observed slowdown mostly occur due to the Weibel instability. However, a slowdown is less efficient in this case.

CHAPTER 5

KINETIC SIMULATION OF MAGNETIC FIELD GENERATION IN THE CONTEXT OF LASER-PLASMA INTERACTION

5.1 INTRODUCTION

Unprecedented progress in high-intensity laser facilities is enabling the exploration of laser-matter interactions under extreme conditions, which is at the heart of High Energy Density Physics (HEDP) research. Much of the interest in short laser pulses started after the development in laser techniques like Chirped Pulse Amplification (CPA), developed by Strickland & Mourou [130], allowing the construction of lasers deliver hundreds of joules of energy down a single beam line in a sub-picosecond pulse. The interaction of ultra-high intensity lasers ($I \sim 10^{14} - 10^{19} W/cm^2$) with matter is characterized by the deposition of huge energy densities for a short period of time $\tau \sim 1ps$). A short intense laser-plasma interaction scenarios have been extensively studied, both theoretically and experimentally. The interest is mainly driven by the potential applications such as inertial confinement fusion, compact particle accelerator radiation sources, Gamma rays sources, electron-positron pair productions, and medical applications, for instance, ion accelerations, compact x-rays sources. One of the active areas of research with this configuration is self-magnetic field generation of MegaTesla (MT) strength.

Radiation from astrophysical events like Gamma-rays, Active Galactic Nuclei, Supernova explosions, TeV, pulsar wind outflows, etc indicates the presence of strong Magnetic fields. However, the origin of these magnetic fields is not clearly understood. Therefore, the origin of magnetic fields from zero-magnetic fields for nonther-

mal particles and radiation process is a fundamental and challenging problem in the context of the astrophysical and laboratory plasma (e.g. fast ignition). It is widely accepted that during the period before recombination, when the cosmic microwave background was generated, there was no magnetic field. However, such radiation process can be explained by two prominent steps: (1) existence of a seed field (2) amplification of that field by a dynamo mechanism. One of the main problems of the origin of seed magnetic fields is how to produce them coherently on cosmological (large) scales. There have been considerable theoretical and experimental investigation of self generating magnetic fields by microphysical plasma processes e.g. due to non-parallel electron density and temperature gradients $(\nabla n_e \times \nabla T_e)$ (known as the Biermann battery [131]), by electron temperature anisotropy (known as the Weibel instability [30]), by counterstreaming charged particle beams (known as the current-filamentation instability [132]), due to the inverse Faraday effect [133,134], and by the ponderomotive forces of intense laser beams [135,136].

Proof of principle experiments of self-generated magnetic fields were first investigated by Stamper et al. [60] involving measurements of magnetic fields in the underdense (coronal) plasma resulting from high power laser interactions with high-density targets. An analytical discussion of the many sources of magnetic fields in hot laser-produced plasmas is presented in [137]. To date, the self-generated magnetic field has been experimentally observed by many groups around the world using different techniques in under/over-dense region [138,139]. Important aspect of the experiments is to examine extremely large magnetic fields (up to Gigagauss) and their consequent effects on the dynamics of the plasma as well as on the propagation of fast electrons produced during the interaction.

Previously, the measurements of self-magnetic fields were extensively demonstrated resulting from high power laser interactions with high-density targets. For a target irradiated with one finite-sized laser beam, this process is most likely to occur in the outer regions of the laser spot, as shown in Fig. 5.1. The density gradient points into the solid-density target face, whereas near the edge of the laser spot the temperature gradient points radially inward toward the axis of the laser beam. The magnetic field is toroidal in shape, has a scale size comparable to the spot radius, and falls to zero at the axis of the laser beam. Since the intensity distribution of the laser beam is usually rather flat near the middle of the focal spot, radial temperature gradients are thought to be small there. Thus, one expects low magnetic fields at the center of the focal region. The order of magnitude of the magnetic field over a time Δt is roughly $\delta t(m_e/e)(V_{Te}^2/L_n T_T)\sin\theta$, where $V_{Te} = (k_B T_e/m_e)^{1/2}$ is the electron thermal speed, L_n and L_T are the scale lengths of the density and electron temperature gradients, respectively, and θ is the angle between the direction of the density and temperature inhomogeneities. To estimate the steady-state size of the magnetic field B_s, one could balance the baroclinic driver and the curl of the $\mathbf{u} \times \mathbf{B}$, where $\mathbf{u} =< \mathbf{v}_i >$ is the out-

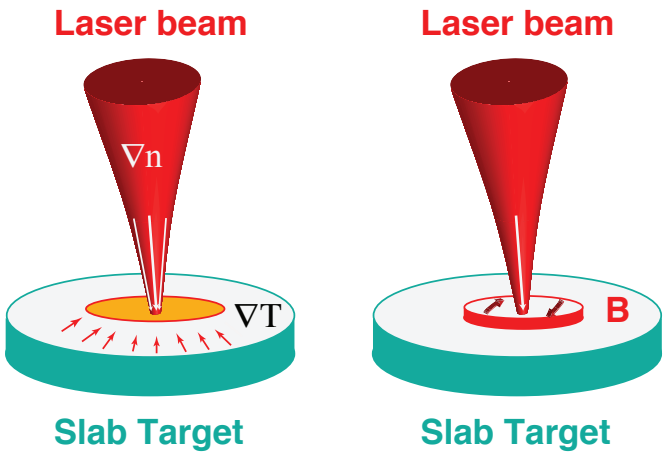

FIGURE 5.1: Schematic representation of produced toroidal dc magnetic fields by the $\nabla n_e \times \nabla T_e$ mechanism.

ward average ion fluid velocity

$$B_s \simeq \left(\frac{m_e L}{e}\right)\left(\frac{V_{Te}^2}{C_s L_n L_T}\right), \tag{5.1}$$

where L is the scale size of the variation of the $\mathbf{u} \times \mathbf{B}$ flow, $|\mathbf{u}| \sim c_s$, and c_s is the ion sound speed.

For a 1-KeV hydrogen plasma with the electron temperature and density gradient scale lengths of order 20 μm, one would obtain a magnetic field strength of the order $\simeq$ 4 MG at place where the density and temperature gradients were at large angles relative to each other. Recently, huge magnetic fields (of the order of 340 MG) have been measured in the high-density region of plasmas produced during intense laser-matter interaction, near the critical density surface [140].

Recent developments in laser technology (with the intensity of 10^{19}W/cm^2 and duration shorter than 1 ps, and high-resolution diagnostics) open the possibility to probe such processes through laser-solid interactions [140,142,143]. Much interest has been revived to demonstrate the generation of the magnetic fields driven by the Current Filamentation/Weibel Instability in the laboratory using an intense short/long pulse laser. The demonstration of magnetic field generation in laser-plasma interaction experiments is addressed by several labs around the world citations [98,144]. In particular, the experiments carried out by Kugland et al [141] shows the signature of the magnetic field generated by the Current Filamentation/Weibel Instability and Biermann Battery. In this experiment, two 2-mm-diameter $\times$0.5mm-thick CH_2 disc target target was ionized by two long pulse (2000 J, 3 ns) 351 nm laser beams with intensity $\sim 10^{15}$w/cm^2 shown in Fig 5.2. As a result, two counter-streaming plasmas

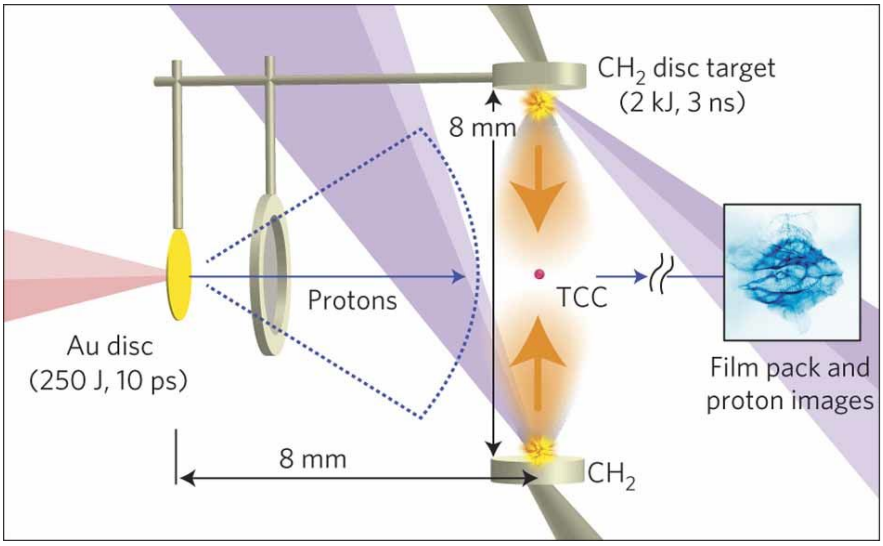

FIGURE 5.2: Experimental set-up at the OMEGA EP laser showing the targets, laser beams and diagnostic configuration Courtesy: Kugland *et al.* [141]

are created which leads to the generation of Current Filamentation/Weibel Instability. The magnetic filament structure is observed using proton beam imaging. It is pointed out that these structures can persist for thousands of ions- and tens of thousands of electron-kinetic timescales. Although it was not entirely clear how these structures form, evidence of their existence is clearly seen in the experimental data. A similar experiment was performed by Huntington et al [145] which then confirms the existence of filamentary structure as ion the Current Filamentation/Weibel Instability.

In another experiment, where the direct observation of a strong magnetic field is clearly seen in hot, dense laser-produced plasmas [98]. An optically the polished aluminum coated BK-7 glass plate target was used and ionized by an intense pump laser with the intensity $\sim 10^{18}\mathrm{w/cm^2}$ see Fig. 5.3. The filamentary structure of the magnetic field is observed at the critical surface of the plasma target see Fig. 5.4. 2D dimension PIC simulation supports underlying physics of CFI, where a forward current of relativistic energy "hot" electrons by the laser pulse and "cold" return currents of thermal electrons induced in the target. However, the power spectrum of magnetic fields spatial profiles does not seems to match with the spectrum of CFI.

In the present work explores a possibility of investigating self consistence magnetic field generation in Laser-plasma interactions via Weibel instability which is in contrast to the magnetic field due to Current filamentation instability seems to occur in the most experiments. We believe that these results are of fundamental importance to understand recent experimental results and to understand the long term evolution of the filaments generated by the Weibel instability.

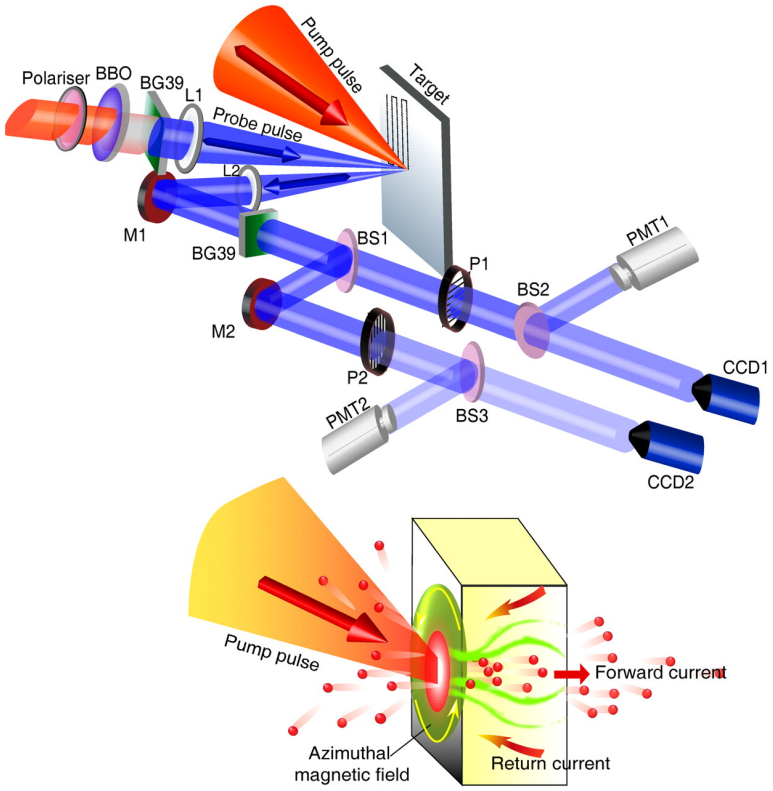

FIGURE 5.3: Sketch of the experimental arrangement for measuring spatial and temporal profiles of the magnetic field (Courtesy: S. Mondal et al. PNAS 2012;109:8011-8015)

5.2 WEIBEL INSTABILITY OCCURS ALONG WITH BIERMANN BATTERY IN COLLISIONLESS SYSTEMS

The Biermann battery is commonly explored in the context of hydrodynamical systems. It occurs due to the non-parallel electron density and temperature gradients which generates the static magnetic field order of $10^6 G$. In these experiments, the magnetic field generation is often attributed to the Biermann battery [60, 98, 146]. Magnetic field grows linearly as $B(t) \approx (m_e c/e)(v_{the}^2 t/L_T L_n)$, where $L_n \equiv n/\Delta n$ and $L_T \equiv T_e/\Delta T_e$ are the density and temperature gradient scale lengths, respectively. Intensive theoretical and computational studies have been carried out to demonstrate the magnetic field generation via the Biermann battery [60, 137, 138] in the context of hydrodynamical systems. Recently, Schoeffler *et.al* [147] investigated the kinetic effect of the Biermann battery in a collisionless expanding plasma (see in Fig. 5.5). For simplicity, $L = L_n = L_T$ was considered. It is found that the Weibel instability competes with the Biermann battery. The relative importance of the Biermann battery can be ad-

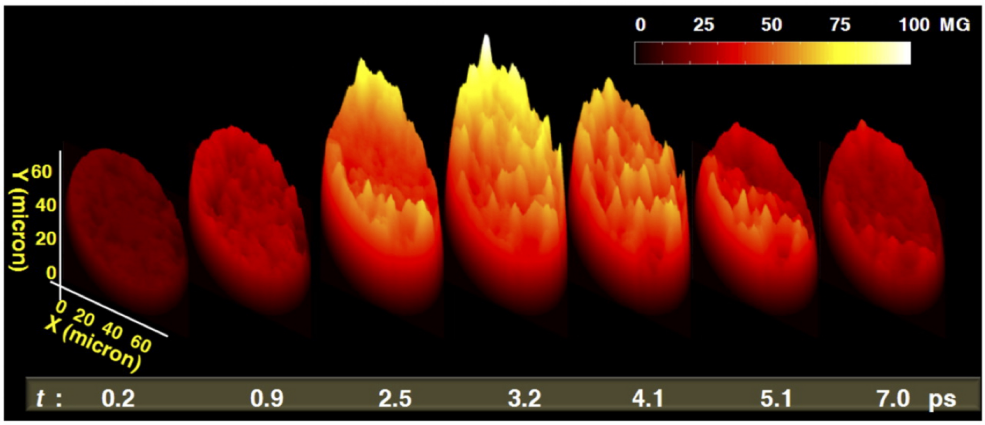

FIGURE 5.4: Complete dynamics of spatiotemporal evolution of the intense laser induced magnetic field at the critical surface of the plasma measured with a 400-nm probe pulse (Courtesy: S. Mondal et al. PNAS 2012;109:8011-8015)

justed by changing the scale length of the density and temperature non-uniformities such that the kinetic effects become important. The Biermann battery generated field obeys the scaling:

$$\frac{B}{\sqrt{8\pi P_{plasma}}} = \beta_e^{-1/2} \approx \frac{1}{\sqrt{2}} \frac{d_e}{L} \tag{5.2}$$

where P_{plasma} is the plasma pressure, $d_e \equiv c/\omega_p$ and $\omega_p = (4\pi e^2 n_e/m_e)^{1/2}$ are the electron skin depth and the plasma frequency, n_e is the electron density, e and m_e are the charge and the rest mass of the electrons and c is the speed of light in vacuum. In this configuration, it is pointed out that for small scale lengths $L/d_e < 100$ the dominant magnetic field is generated via the Biermann mechanism. In contrast when $L/d_e \geq 100$, the Weibel instability generates magnetic fields faster than the Biermann battery. Fig. 5.5 illustrates the scaling with the system size of the maximum and the average magnitude of the magnetic field. These simulations showed that there are magnetic fields even for very large scale lengths, where no Biermann driven magnetic fields are to be expected. At these scale lengths, the magnetic field is generated by the Weibel instability. It is pointed out for small systems $L_n/d_e < 100$ the dominant magnetic field is generated by Biermann mechanism. In contrast, $L_n/d_e \geq 100$, the Weibel fields, which are caused by temperature an anisotropy [30], grows faster than Biermann fields. The Biermann field is a pervasive mechanism in laser-solid experiments. The processes of generating magnetic fields via Weibel instability have been of strong interest to be demonstrated in experiments. Although this Weibel dominated regime has been shown to exist theoretically, it has not yet been demonstrated that this regime can be achieved and measured experimentally in the context of laser-plasma interaction.

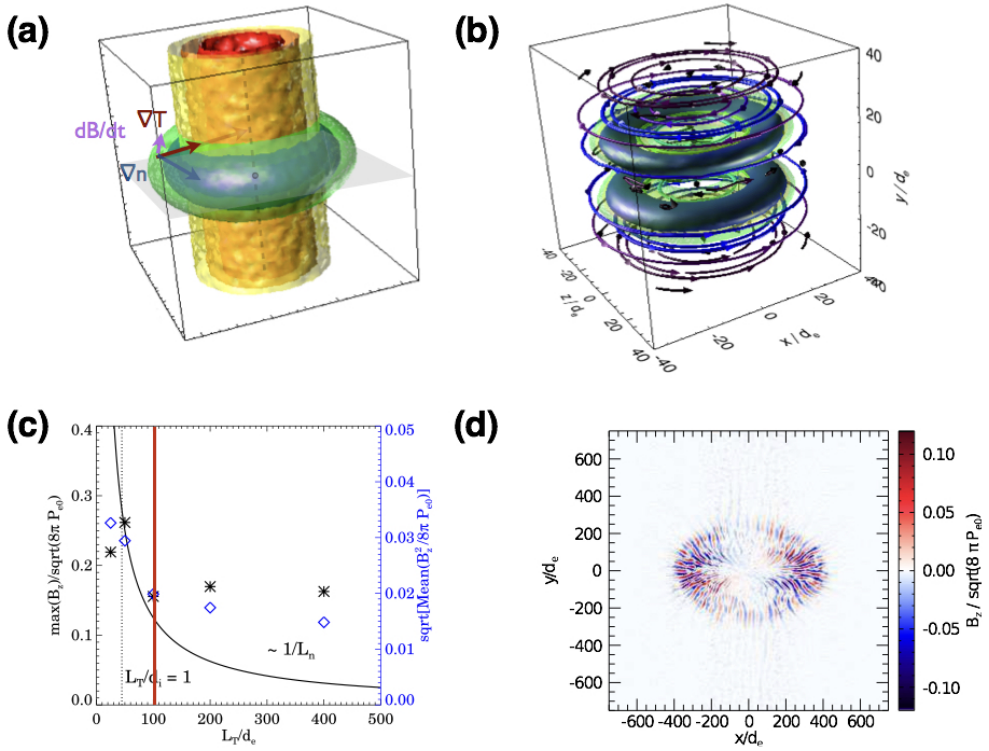

FIGURE 5.5: (a) Kinetic 3D simulation of Biermann battery (b) magnetic energy contours after saturation (c) Maximum (black asterisks), and average magnitude of the magnetic field B_z, vs. L_T/d_e with $m_i/m_e = 2000$ (d) Out-of-plane magnetic field at peak magnitude with m_i/m_e= 2000 showing existence of Weibel fields [147] .

In this work, we carry out a detailed numerical and theoretical study using first-principles particle-in-cell (PIC) simulations to investigate magnetic fields generated by the Weibel instability in the interaction of a short (ps) high intensity ($a_0 \geq 1$) laser pulse with a plasma having a sufficiently large gradient scale length (L). Our simulation results reveal that by tuning the delay between the ionizing pre-pulse and the main pulse, and the spot size of the laser such that $L/d_e \geq 100$, the Weibel generated magnetic fields can be observed in laser-plasma interaction experiments in current available facilities.

5.3 2D PIC Simulation model

In order to study the laser-driven Weibel instability, a series of two-dimensional (2D) PIC simulations have been performed with the fully relativistic, massively parallel code OSIRIS [70, 71]. We modeled the interaction of a s-polarized (i.e. the electric

field is perpendicular to the simulation plane) intense laser pulse with a pre-formed plasma, consisting of electrons and fully ionized hydrogen ions with $m_i = 1836\, m_e$, where m_e is the electron mass. We have chosen s-polarization in order to isolate the out-of-plane Biermann and Weibel magnetic fields from laser fields. In 2D simulations, a p-polarized laser will generate a higher temperature than 3D. Therefore, in order to better approximate 3D conditions, we use s-polarized simulations, which have been shown to have less heating than p-polarized. [148, 149].

A laser with normalized vector potential $a_0 = 2$ corresponding to a peak intensity of $I_L = 10^{19}\,\mathrm{W/cm^2}$ and wavelength $\lambda_L = 1.0\,\mu m$ propagating in the x_1 direction has been considered. We consider a reference plasma density $n_0 = 1.1 \times 10^{22}\, cm^{-3} = 10\, n_c$, where $n_c = \omega_L^2 m_e / 4\pi e^2$ is the critical density, and $\omega_L = 2\pi c/\lambda_L$ the laser frequency. The envelope of the pulse follows a flat-top (FT) function having rise (R) and fall (F) time $\tau_R = \tau_F = 10.0\,\omega_p^{-1}(1.7\,\mathrm{fs})$ and duration $\tau_{FT} = 1034\,\omega_p^{-1}(175\,\mathrm{fs})$. Its transverse profile is modelled as a Gaussian function with spot size at full width half maximum (FWHM) $w_{FWHM} = 100\, d_e(5\,\mu\mathrm{m})$. These are typical laser parameters in laser-solid interaction experiments [144]. The laser interacts with a plasma having longitudinal electron density profile $n(x_1) = 0.5\, n_0 \{\tanh[2\,(x_1 - x_{10})\,/L_n] + 1\}$, where $n_0 = 10\, n_c$ is the maximum density, x_1 the longitudinal coordinate, and $L_n (= n_0/\nabla n(x_{10}))$ is the initial density scale length.

In the simulation results presented here, $x_{10} = 1250\, d_e$, coinciding with the laser focal plane and $L_n = 400\, d_e(20\,\mu\mathrm{m})$, where $d_e \equiv c/\omega_p$ and $\omega_p = (4\pi e^2 n_0/m_e)^{1/2}$. In this configuration, we are interested to observe the magnetic field at the front surface of the target. The length of the target is chosen to be long enough that the back side does not influence the front, while the density is 0 at the right wall to avoid significant particle loss at the boundary. We chose a step function at $x_1 = 1750\, d_e$ to minimize the length and save computational time (see Figure 5.6 (a)) .

At the beginning of the simulation, electrons and ions have a temperature $T_e = 1\,\mathrm{keV}$ and $T_i = 1\,\mathrm{eV}$, respectively (small compared to the laser heating, but large enough that we can resolve the Debye length). A simulation box with size $2000 \times 2000\, d_e^2$ divided into 20000×20000 cells and a time step $\Delta t = 0.05\,\omega_p^{-1}$ have been employed. Each cell contains 12 macro-particles per species, whose dynamics have been followed for more than 100000 time steps. Absorbing boundary conditions along x_1 and periodic along x_2 have been selected for fields and particles. To suppress the numerical heating, a fourth order interpolation scheme has been used together with a 5-pass filter to evaluate current and fields. Larger transverse box sizes, higher spatial and temporal resolution and higher number of particles per cell were tested, showing overall result convergence. The laser enters the simulation domain from the left and at first, interacts with an underdense plasma. It penetrates until $1000\, d_e$, where the plasma density reaches the critical density n_c at time $t \simeq 1200.50\,\omega_p^{-1}$ (Figure 5.6 (a)). The interaction of the laser with the plasma resonantly heats the electrons and

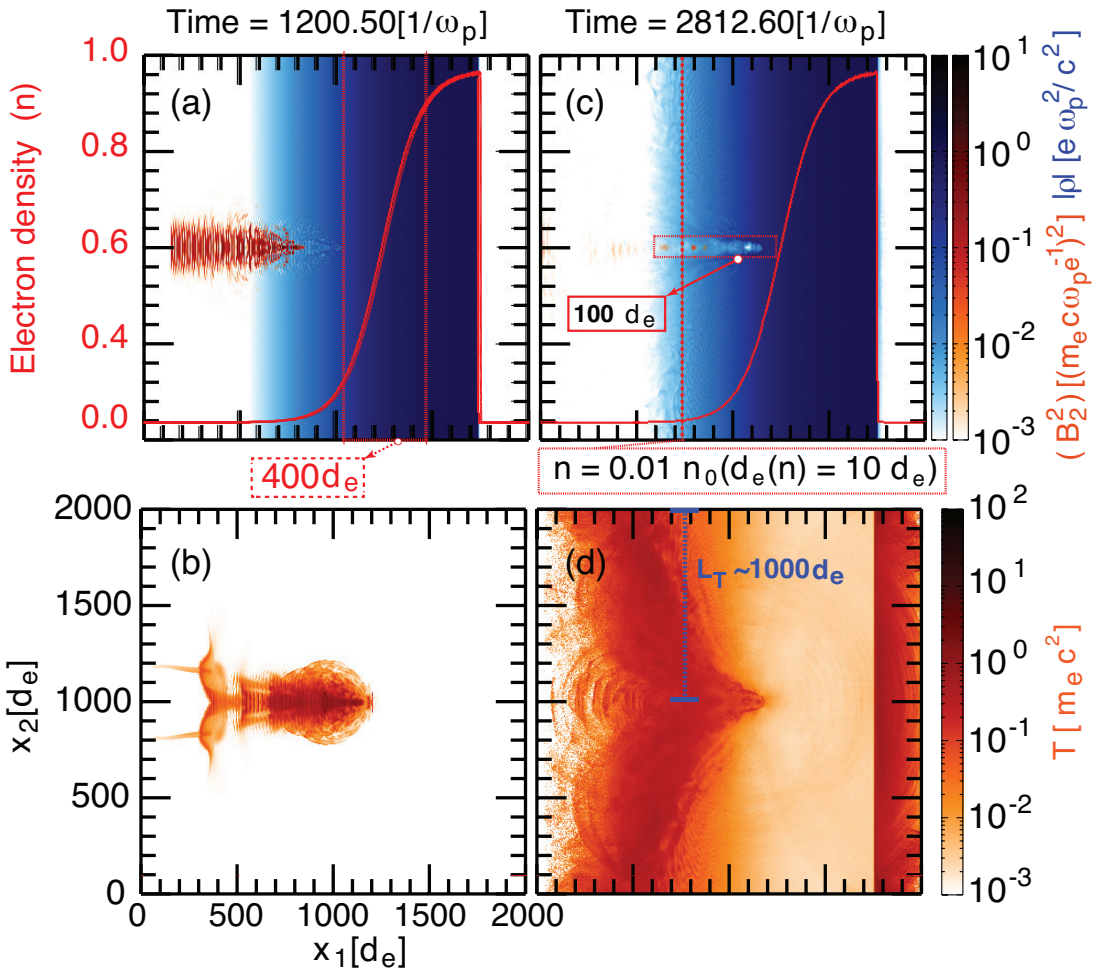

FIGURE 5.6: Electron density (blue) and laser magnetic field (B_2^2) (orange) (a, c) and electron temperature calculated at the fluid rest frame (b, d) at $t = 1200.5$ and $2812.6\,\omega_p^{-1}$ respectively. The red solid lines in (a) and (c) are an average of the density along the x_2 direction, and the dashed red line shows the gradient length scale $L_n = 400\,d_e$. The red dashed box in (c) indicates the focal spot of the laser. The red dashed line defines the boundary between $L_n > 100\,d_e(x_1)$ (left), and $L_n < 100\,d_e(x_1)$ (right). The blue dashed lines in (d) point to the location where $L_T \simeq 1000\,d_e$.

results in a temperature gradient pointing radially towards the axis of the laser beam (Figure 5.6 (b)). The temperature averaged in the region $x_1 = [850 - 1050]\,d_e, x_2 = [980 - 1020]\,d_e$ is $T_e \simeq 9.0\,m_e c^2$, comparable to the Pukhov scaling [150] for the laser intensity $a_0 = 2$ ($T_e \simeq 6.9\,m_e c^2$). The temperature gradient is not aligned with the density gradient along x_1 allowing the Biermann battery to generate a toroidal B-field. The laser compresses the target locally and pushes the electrons inwards via the ponderomotive force, creating a conical shaped channel by $t \simeq 2812.60\,\omega_p^{-1}$

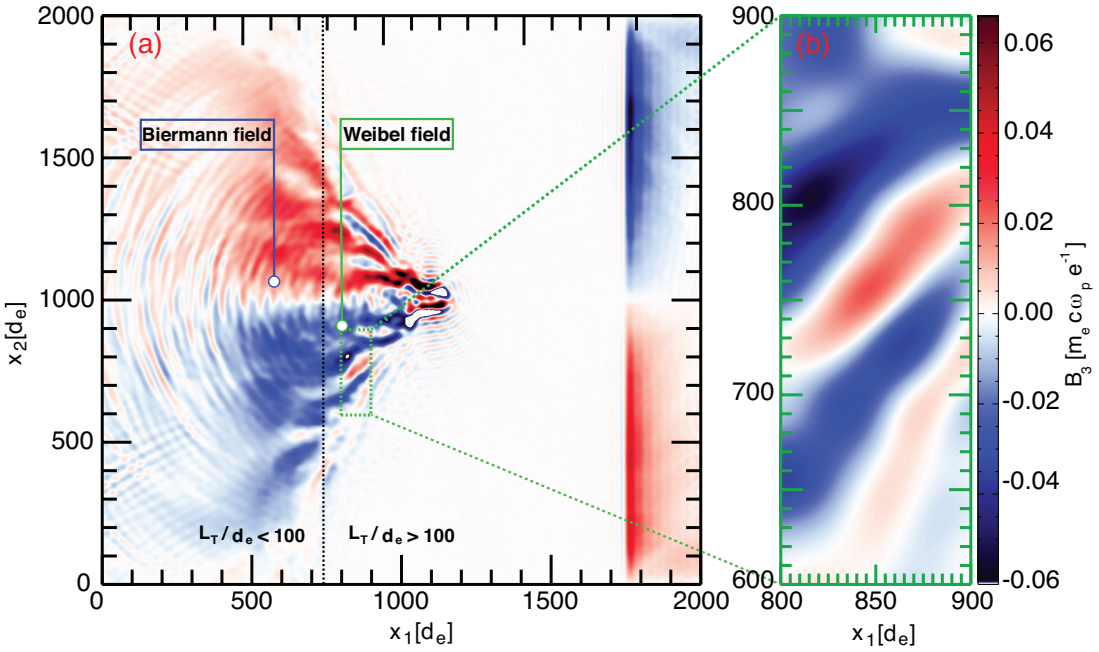

FIGURE 5.7: (color online). Transverse magnetic field B_3 at $t = 2641.10\,\omega_p^{-1}(440\,\text{fs})$ (a) and zoom-in of Weibel-generated magnetic filaments with $k \approx 0.06\,d_e^{-1}$. The black dashed line in (a) indicates the transition point between the region where Biermann fields dominate ($L_T/d_e < 100$) and the region where Weibel fields dominate ($L_T/d_e > 100$). Note that the spatial scale is identical in all sub-figures.

(Figure 5.6 (c)). Meanwhile the heat spreads across the target leading to a smoother temperature gradient. Along $x_1 = 700\,d_e$, the average temperature is $0.34\,m_e c^2$ (see Fig. 5.6). Given this lower temperature and the density $n_0 = 1.1 \times 10^{22}\,cm^{-3}$, we can make a conservative estimate on the collisionality, which we have neglected. The ratio of the gradient scale length L_n and the electron collisional mean free path l_e, $L_n/l_e = 0.00047 \ll 1$ [151], and thus collisions can be neglected. The Biermann-produced out-of-plane magnetic field B_3 is shown in Figure 5.7 at $t = 2641.10\,\omega_p^{-1}$. However, along side the Biermann-generated field, clearly recognizable in the region $x_1 = [0, 700]\,d_e$, a region where the field is due to the Weibel instability is also observed. Note that a low-pass filter was applied to the magnetic field only allowing wavelengths above 31.4 d_e (1.57 μm), mimicking the experimental resolution [144]. The boundary between Biermann and Weibel regimes can be estimated at the location where $L_T(x_1)/d_e(x_1) \approx 100$ [147, 152], where $d_e(x_1) \equiv c/\omega_p(x_1)$ is the local electron inertial length. At $x_1 \approx 700\,d_e$, $d_e(x_1) \approx 10\,c/\omega_p$ based on the density ($n = 0.01\,n_0$; see Figure 5.6(c)), and the length scale of $L_T(x_1) \approx 1000 d_e$ estimated from Figure 5.6(d). The dotted vertical line in Figure 5.7(a) therefore separates regimes of Biermann and Weibel fields at $L_T(x_1)/d_e(x_1) \approx 100$. In the region where $L_T(x_1)/d_e(x_1) < 100$

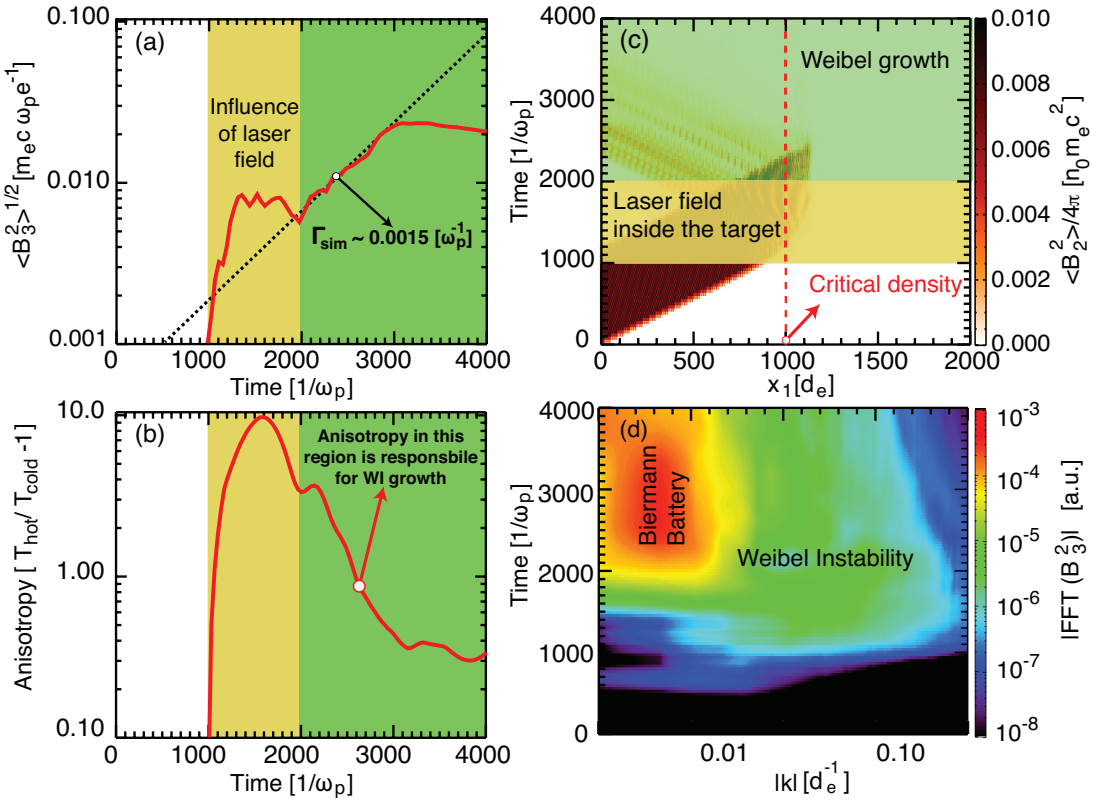

FIGURE 5.8: (color online). Temporal evolution of the out-of-plane magnetic field strength in the green box indicated in Fig 5.7 (a). The slope of the curve in (a) allows for inferring the growth rate of the Weibel instability, which is measured to be $\simeq 0.0015\,\omega_p$ (black dashed line). Average anisotropy $(T_{hot}/T_{cold} - 1)$ in the green box indicated in figure 5.7 (b). Average energy of the magnetic field (B_2) in the x_2 direction showing the time evolution of laser field energy for the same region (c) and temporal evolution of the transverse magnetic field energy (B_3^2) spectrum showing the contribution to B-field from Weibel instability and Biermann battery(d).

the dominant mechanism for magnetic field generation is the Biermann battery effect, which arises due to the gradients of electron density and temperature where $\nabla n_e \times \nabla T_e$ is non-zero. However, the Weibel instability dominates in the region where $L_T(x_1)/d_e(x_1) > 100$ (Figure 5.7) (a,b) exhibiting small magnetic filament structures. These results are consistent with the predictions from Schoeffler *et. al* [147]. Figure 5.8 (a) shows the temporal evolution of the averaged out-of-plane magnetic field B_3 in the region $x_1 = [800 - 900]\,d_e, x_2 = [600 - 900]\,d_e$, where the dominant source of the magnetic field is the Weibel instability. We observe an exponential growth of the magnetic field between $2000 - 3000\,\omega_p^{-1}$, after the laser has passed this region (see Figure 5.8 (c)). The expansion of the hot energetic electron population generated by laser-heating produces an anisotropy in the velocity distribution [153]. Furthermore, the laser itself will contribute to the temperature anisotropy. The anisotropy with the

temperature in one direction (T_{hot}), larger than the perpendicular temperature T_{cold}, provides the free energy that drives the Weibel instability.

The linear growth rate of the Weibel instability from the average magnetic field strength measured in the region $x_1 = [800 - 900]\, d_e, x_2 = [600 - 900]\, d_e$ is $\Gamma_{sim} = 0.0015\, \omega_p$ with a corresponding wave-vector $k \simeq 0.15\, d_e^{-1}$ (see Fig. 5.8(a)). The theoretical growth rate assuming a relativistic generalization of the bi-Maxwellian electron distribution according to Kaang [154] can be calculated using the measured temperatures and density ($T_{hot} = 0.34\, m_e c^2, T_{cold} = 0.18\, m_e c^2$, and $n_e = 0.019\, n_0$) averaged over the same region at time $t = 2006\, \omega_p^{-1}$. This is the earliest time after the laser field strength becomes negligible (see Fig. 5.8(b)), which avoids further deviation from a bi-Maxwellian distribution, as the Weibel field is biased towards isotropizing the particles with momentum $p/m_e c \sim 1$. Despite the roughness of the theoretical model, the theoretical fastest growth growing mode occurs at $k \simeq 0.05\, d_e^{-1}$, with a growth rate $\Gamma_{theory} = 0.0043\, \omega_p$, fitting the simulation within an order of magnitude.

To isolate the magnetic fields generated by the Weibel instability, we ran our simulation long enough ($t > 2000\, \omega_p^{-1} (330\,\text{fs})$) that the magnetic fields associated with the laser are no longer present. The spatiotemporal evolution of the laser magnetic field energy is shown in Figure 3 (c). The laser interacts with the target at the critical density at $1000\, \omega_p^{-1}$. The end of the laser pulse passes the region where we calculated the growth rate at $\sim 2000\, \omega_p^{-1}$. For $t > 2000\, \omega_p^{-1}$, the magnetic field is thus produced by the Weibel instability. The instability can generate a strong transverse magnetic field with maximum amplitudes of the order of $0.065\, m_e c / e\omega_p$ (22 MGauss). The spectrum of B_3^2 as a function of time is shown in 5.8(d), showing the contribution of the Weibel instability and the Biermann battery to the magnetic field energy. The spectra are obtained by performing a Fourier transform over the entire system for the out-of-plane magnetic fields, and then averaging over all directions of $\mathbf{k}$. Note that due to the log scale it may not be obvious that the energy contained in the Weibel magnetic fields is comparable to that of the Biermann. The Biermann magnetic field energy is five times higher than the Weibel magnetic fields energy.

By investigating the interaction of a laser with targets of various density gradients, we have demonstrated that there is a transition between the regimes where only the Biermann battery is present (for $L_n/d_e < 160$) and both the Weibel instability and the Biermann battery are present (for $L_n/d_e > 160$), as shown in Figure 5.9. We kept the laser and simulation parameters constant in order to isolate the role of the scale length. In experiments, after the target is ionized by the pre-pulse, the plasma expands resulting in a non-uniform density with a gradient length that can reach several micrometers when the main pulse arrives. A possible model for the density scale length as a function of time yields $L_n(t) = 2.75 \times 10^{-7}\text{cm} \cdot I_L^{10/27} A^{-2/27} \Lambda^{4/27} \lambda_L^{4/9} t^{31/27}$, where $A\ (= 2)$ and $\Lambda\ (= 5)$ are the nuclear mass number and Coulomb logarithm of deuterium [155]. For example, with these scalings, if we use a typical pre-pulse laser with intensity of

$I_L = 10^{12}\mathrm{W/cm}^{-2}$ and a pulse delay of 278 ps, we can obtain a density scale length L_n of $400\,d_e$, while for 68.4 ps we obtain $80\,d_e$. This confirms that these density scale lengths can be tuned experimentally.

We performed a parameter scan for $\mathrm{L_n}/d_e = 0, 80, 160, 240, 320, 400$ of the plasma. Note that by the time the laser reaches the target at $t \sim 1250\,\omega_p^{-1}$, the length scale should have risen by $\sim v_{th}\sqrt{m_e/m_i}\,t \sim 1.3\,d_e$ using our initial $T = 1\,\mathrm{keV}$. Therefore, for $L_n/d_e = 0$, the effective density scale length is $1.3\,d_e$. The out-of-plane magnetic field B_3 is shown in Figure 5.9 (a)-(d) at time $t = 2023.70\,\omega_p^{-1}$ for different density gradient lengths $L_n/d_e = 0, 80, 160, 320$. With a target of sufficiently large gradient scale length $L_n/d_e > 160$, the expanding hot energetic electron population generated by the laser leads to the region of Weibel generated magnetic fields as shown in Figure 5.9 (a) with $L_n/d_e = 320$. However, for short plasma scale lengths $(L_n/d_e < 160)$, the Biermann magnetic field dominates, and no region is found where the Weibel instability is prominent.

When the laser hits the plasma target with a sharp boundary density profile, a transverse magnetic field is generated via the current filamentation instability (CFI) [95, 156] which has been used to explain many experiments [157, 158]. Unlike the Weibel generated field described in this work, a sharp relativistic electron beam provides the free energy rather than a thermal expansion of the plasma. Although CFI does drive out-of-plane magnetic field B_3, our simulations show that the magnetic field generated by CFI is much weaker than both the Weibel and the Biermann fields. Furthermore, the Weibel instability is generated in the same region where the Biermann battery can be found (where the density and temperature gradients exist), rather than deep in the target.

The temporal evolution of the averaged magnetic fields in the region between $x_1 = (1250 - 1.875\,L_n)\,d_e$ and $x_1 = (1250 + 1.25\,L_n)\,d_e$ for each simulation is shown in Figure 5.9(e) (see highlighted regions in Figure 5.9 (a)-(d) for each scale length L_n/d_e). For all cases, except $(L_n/d_e = 0)$, the averaged magnetic field saturates at $t \sim 2000\,\omega_p^{-1}$ and slowly decays. The mean B-field energy is shown as a function of L_n/d_e. The maximum average magnetic field strength is achieved for $L_n/d_e = 160$, at the same length scale where the transition from Biermann to Weibel regimes occurs.

In addition to the standard method of measuring magnetic fields using proton radiography, it may be possible to measure the synchrotron radiation. If we consider a cone from $x = (750 - 1150)\,d_e$ with radius $r = 500\,d_e$ (where the Weibel magnetic field $B \approx 22\,\mathrm{MGauss}$), this would correspond to a volume $13000\mu m^3$ with average density $n_0 = 2.2 \times 10^{20}\,cm^{-3}$. Assuming the electrons have a Lorentz factor $\gamma = 2$, this would generate 881 kW of 1.02 eV radiation. If we assume 10% of those particles have $\gamma = 5$, these would generate 550 kW of 6.39 eV radiation. A measurement of the radiation spectra could be used to measure the magnetic field strength or the electron energy spectra. For higher power lasers, this signal would become stronger and approach

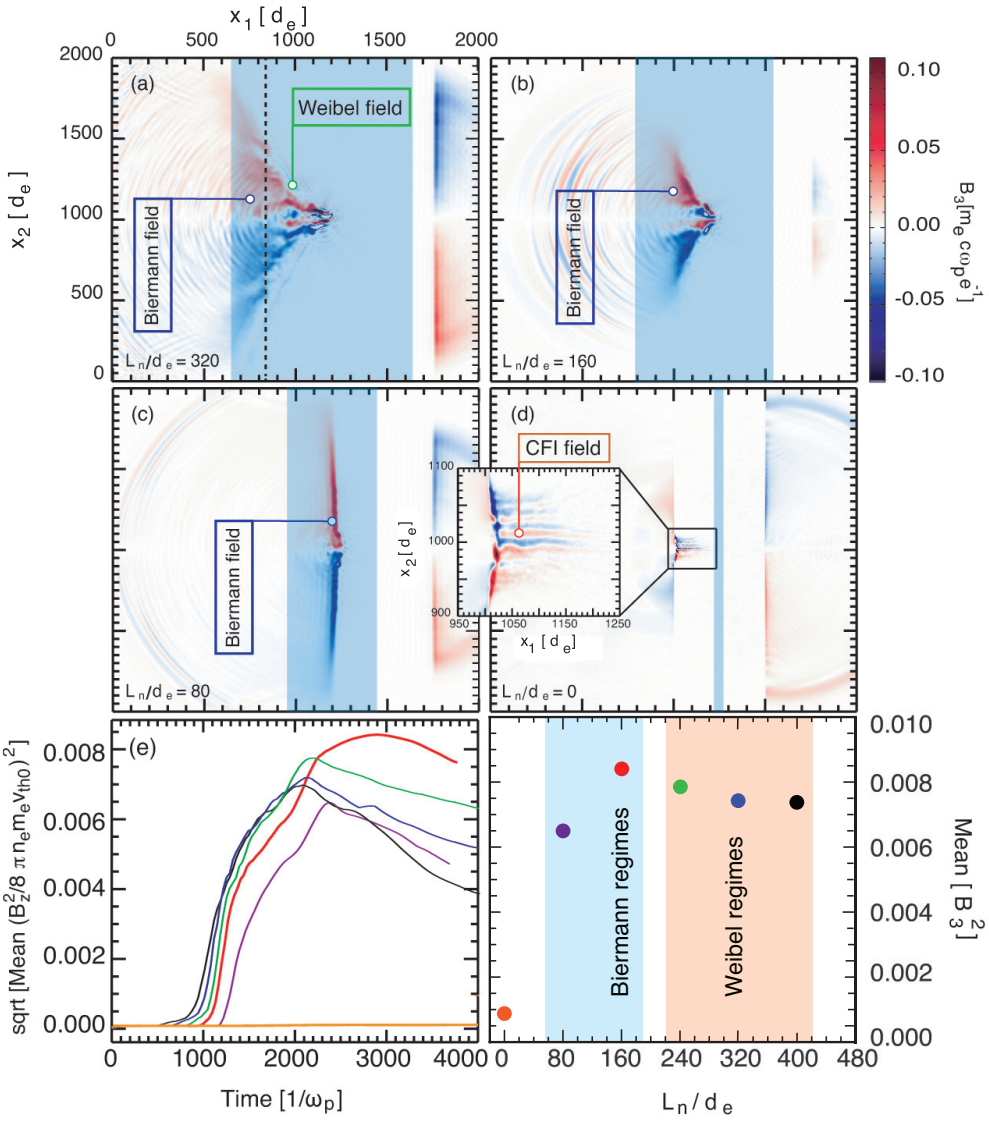

FIGURE 5.9: Out of plane magnetic field for $L_n/d_e = 320, 160, 80, 0$ at time $t = 2023.70\,\omega_p^{-1}$. Shaded regions where the mean field energy was averaged between $L = (1250 - 1.875L_n)\,d_e$ and $(1250 + 1.25L_n)\,d_e$. Temporal evolution of the average magnetic field energy (averaged over the specified regions highlighted in (a)-(d)). The average magnetic field reaches a maximum at Time $= t_{max}$ (c) The average magnetic field at t_{max} vs. L_n. The Biermann field dominates over the Weibel between $80 \geq L_n/d_e \geq 160$ (blue region), while a region where the Weibel field dominates exists when $240 \geq L_n/d_e$ (red region). Only the weak current filamentation instability is found for $L_n/d_e = 0$ (effectively 1.3).

x-ray frequencies.

5.4 CONCLUSIONS

In this chapter, we have demonstrated for the first time the possibility to clearly observe the generation of electron Weibel magnetic fields in laboratory experiments. First-principles PIC simulations of the interaction of an intense laser pulse with an overdense plasma target have shown that in the presence of sufficiently weak density gradients at the front of the target ($L_n/d_e \geq 160$ and $w_{FWHM} = 100\, d_e$), the Weibel instability grows on very short time scales and produces fields whose saturation strength is large compared to the Biermann battery fields, which naturally arise in laser-plasma experiments. The Weibel instability is driven by an electron pressure anisotropy caused by the rapid expansion of the electrons, which follows the laser-plasma interaction.

Finally, we notice that density gradients of the type needed to observe the instability at work could easily be achieved by tuning the delay between the ionizing prepulse and the main pulse of the laser system at existing laser facilities. For instance, facilities such as the Vulcan laser facility at Rutherford Appleton Laboratory [159] with a peak intensity around $I_L = 10^{19}\,\mathrm{W/cm^2}$, wavelength $\lambda_L = 1.054\,\mu m$ a duration of hundreds of femtosecond and a contrast of 10^7 would easily allow testing the interplay and the competition between the Weibel and the Biermann regimes, thus opening the way to explore magnetogensis due to these mechanisms and their interplay.

CHAPTER 6

CONCLUSIONS AND FUTURE WORK

6.1 SUMMARY

The generation of magnetic fields in astrophysical and laboratory plasmas is of paramount importance. In this context, this thesis investigates the role of plasma instabilities in the self-consistent generation of magnetic fields, as a mechanism for magnetic field generation in Gamma-ray-bursts (GRBs) as well as for its implication of probing magnetic field structure in laser-matter interactions. Leveraging on fully kinetic one-to-one particle-in-cell (PIC) simulations, I defined criteria for probing magnetic fields driven by Current Filamentation/Weibel instability (CFI/WI) experimentally. I have explored the microphysical plasma processes mimicking realistic astrophysical scenarios such as the fireball beam interaction with plasma, the interpenetration of two dark-plasma clouds, and intense-laser matter interactions. I demonstrated the temporal and spatial behaviours of these microphysical plasma processes on the smallest scales of the plasma.

In chapter 3, I investigated how electron-positron fireballs, that have been produced experimentally, could be used to investigate the CFI in the laboratory. I derived a set of threshold conditions that establish key criteria for the experimental observations of these processes. I show that the ratio between the density of the fireball and background plasma controls a transition between the CFI and the competing transverse two-stream instability. When the density ratio is higher than unity the CFI can grow as long as the beam expansion rate, caused by a finite emittance, is larger than the CFI growth rate. I find that the longitudinal energy spread, typical of plasma-based accelerated electron-positron fireball beams, plays a minor role in the growth of CFI.

In addition, motivated by recent observations of dark-matter with the constrained of dark fine-structure constant ($\alpha_D = 10^{-3}$) and the mass of the Dark matter (DM) ($m_D \leq 10$ TeV) dark matter might exhibit plasma like collective nature that could determine the dynamics of DM. Besides their differences in charge to mass ratio, DM like plasmas are considered being albeit cold and collisionless plasma. One of the key questions that has been pointed out, is whether plasma-like instabilities may have a significant impact on the dynamics of galactic DM clouds. In Chapter 4, I investigate if dark-matter could interact with itself through dark electromagnetic interactions. Because dark-matter electromagnetism is similar to classical electromagnetisms but acting only on dark-matter, I explored this topic using classical electromagnetic OSIRIS simulations, which enabled to set upper limits to the dark matter charge-mass ratio by considering the interaction between two DM plasma-like e^--e^+ clouds. I have shown the interpretation of DM suffers from the plasma-like instabilities generating dark electromagnetic fields at the expense of bulk flow energy. I estimate the slow down due to the interaction of two DM clouds via an electromagnetic-like interaction. The slow down is mostly due to the generated magnetic fields, which deflects particles trajectories such that their velocities acquire a transverse component. This isotropizes the velocity distribution and is responsible for slowing down the flow in the initial longitudinal direction. The isotropization of the velocity distribution would slow down the flow roughly by $1/\sqrt{2}$ in 2D and $1/\sqrt{3}$ in 3D. I have also shown that if typical dark matter slab length is much longer than v_1Dt, I always expect particles to slow down.

Finally, I demonstrated the possibility of driving the Weibel magnetic field in the laboratory by the interaction of an intense laser pulse with an overdense target under realistic conditions (finite laser spot size, realistic ion-electron mass ratio, and realistic target densities) in Chapter 5. The generation of the magnetic fields in laser-solid experiments is often attributed to the Biermann battery, which is generated by non-parallel density and temperature gradients. In this work, I demonstrate the possibility of experimentally generating a strong Weibel magnetic field. I model, using *ab initio* PIC simulations, the interaction of a short (ps) high intensity ($a_0 \geq 1$) laser pulse, with a target of sufficiently large gradient scale length. The expanding hot energetic electron population generated by the laser produces an anisotropy in the velocity distribution. This anisotropy provides the free energy that drives the Weibel instability that appears on the surfaces of the target and dominates over the Biermann battery field.

6.2 FUTURE DIRECTIONS

The work developed in this thesis provides fundamental guidelines for probing the generation of magnetic field in controlled laboratory environments, thus allowing

the comprehension of astrophysical phenomena, where in situ measurements are not possible and the available information mostly derives from indirect measurements of emitted radiation. Therefore, as a natural continuation of this work, I speculate that it would be interesting to determine the main radiation signatures linked to the analyzed framework resorting to post-processing diagnostics. These radiation signatures can then be used to perform predictions for future laboratory experiments and to compare them with astronomical observations. In particular, the innovative configuration explored in chapter 3, which leverages ultra-relativistic fireball beams, provides a realistic insight into the GRBs dynamics. Therefore radiation signatures could be directly correlated with the spectra of the afterglow of GRBs. The strong fields generated by the interaction of the fireball beams with the plasma will lead to extreme particle acceleration and emission of gamma rays via synchrotron or synchrotron self-Compton emission. Hence, it would be intriguing exploring the effects of more exotic physical processes, as radiation reaction or quantum electrodynamics effects on the dynamics of the interaction. Moreover, the same setup adding an external magnetic field could be employed to explore the interaction of astrophysical jets with the magnetized ambient medium. Also, in this case, it is expected that a multitude of plasma phenomena spanning from the generation of turbulence to particle acceleration will be observed. An ion component could be added to the fireball beam. This would provide an understanding of the jet composition, the relative abundance of ions and pairs and their roles in the jet dynamics, dissipation, and radiation. All these topics are in fact still the argument of debate by the scientific community. A similar simulation setup could also be exploited to explore the onset of shock formation and propagation.

Radiation reaction and quantum electrodynamics effects play a role also during ultraintense laser-matter interaction. Therefore, exploring their role on the physics examined in chapter 5 is of extreme importance. To plan a possible experiment to probe the Weibel instability via laser-solid target interaction, 2D simulations are enough to provide general guidance. However, in order to thoroughly interpret laboratory results, where experimental diagnostics might be limited, full 3D simulations will be necessary. They will be indeed required to examine the complex structures of 3D magnetic fields

Finally, about the existence of dark electromagnetism, which was extensively discussed in chapter 4, I believe that the effects of the dark plasma during the merger of galaxy clusters remain to be studied. Furthermore, the validity of the fluid approximation has to be identified as a function of the mass, charge, and density of the charged DM particles.

APPENDIX A

THE TWO STREAM INSTABILITY

Two-stream instability occurs due to two counter-streaming plasma flow in the space. The initial stage is described by using the linearized Vlasov equation

$$\frac{\partial f_{j1}}{\partial t} + v\frac{\partial f_{j1}}{\partial z} + \frac{q_j E}{m_j}\frac{\partial f_{j0}}{\partial v} = 0 \tag{A.1}$$

where f_{j0} is the distribution function of the unperturbed particles (s=e for electrons and j=0 for protons) and f_{j1} is the perturbation induced by and linearly proportional to the electric field E.

We consider an electrostatic propagation in the z-directions where the electric field point in the z-direction $\mathbf{E} = \mathbf{E}\mathbf{e_z}$, and varies with $e^{-i(kz-\omega t)}$ which imply $\partial/\partial t \to -i\omega$ and $\partial/\partial z \to ik$. Solving the equ. (A.1) for f_{j1}, we obtain

$$f_{j1} = \frac{-iq_j}{m_j(\omega - kv)}\frac{\partial f_{j0}}{\partial v}E \tag{A.2}$$

The electric field is calculated by using Poisson's equation

$$ikE_{j1} = \frac{\rho_{j1}}{\epsilon_0} \tag{A.3}$$

which leads to the dispersion relation:

$$\epsilon(k\omega) = 1 + \frac{e^2}{m_e\epsilon_0 k}\int_{-\infty}^{\infty}\frac{\frac{\partial f_{j0}}{\partial v}}{\omega - kv}dv = 0 \tag{A.4}$$

We chose a δ distribution function for each species with moving opposite bulk momenta ($\pm v_0$) along the z-direction in a Cartesian coordinate system

$$f_0(v) = \frac{1}{2}n[\delta(v - v_0) + \delta(v - v_0)] \tag{A.5}$$

where n is the total electron and proton density of the two streams. We then calculate the integral of the above equation using the integration by parts:

$$\int_{-\infty}^{\infty} \frac{\frac{\partial f_{j0}}{\partial v}}{\omega - kv} dv = \int_{-\infty}^{\infty} f_{j0} \frac{\partial}{\partial v} \frac{1}{(\omega - kv)} dv + \left[\frac{f_{j0}}{(\omega - kv)} \right] \tag{A.6}$$

$$\int_{-\infty}^{\infty} \frac{\frac{\partial f_{j0}}{\partial v}}{\omega - kv} dv = -\frac{kn}{2} \left(\frac{1}{(\omega - kv)^2} + \frac{1}{(\omega + kv)^2} \right) \tag{A.7}$$

The dispersion relation for a purely electrostatic mode is given by

$$\epsilon(k\omega) = 1 - \frac{1}{2} \left(\frac{\omega_p^2}{(\omega - kv)^2} + \frac{\omega_p^2}{(\omega + kv)^2} \right) \tag{A.8}$$

Hence, the instability develops when $v_0 > \omega_p / k$.

APPENDIX B

THE WEIBEL INSTABILITY

The Weibel instability occurs due to a pressure anisotropy in an arbitrary the direction in a plasma with a small magnetic field. A linear instability is derived from kinetic theory using the Vlasov equation and Maxwell's equations, implementing an anisotropic velocity distribution.

Consider the Vlasov equation for the distribution function $f_j(t, x, \mathbf{v}) = \mathbf{f_0}(\mathbf{v}) + \mathbf{f_{j1}}(\mathbf{t}, \mathbf{x}, \mathbf{v})$ by neglecting external $E_0 = B_0 = 0$,

$$\frac{\partial f_j}{\partial t} + \mathbf{v} \cdot \nabla f_j + \frac{e}{m}\left(\mathbf{E} + \frac{\mathbf{v} \times \mathbf{B}}{\mathbf{c}}\right) \cdot \frac{\partial f_j}{\partial \mathbf{v}} = 0 \tag{B.1}$$

The j subscript presents the species of interest, for instance electrons or ions. Taking only the first terms in $\mathbf{E}$, $\mathbf{B}$ and f_j, $\mathbf{v}$ assuming space-time dependence in the form $e^{i\mathbf{k}\cdot\mathbf{x} - \mathbf{i}\mathbf{l}\mathbf{t}}$. This yields

$$f_{j1} = -\frac{ie}{m(\omega - \mathbf{k} \cdot \mathbf{v})}\left(\mathbf{E_1} + \frac{\mathbf{v} \times \mathbf{B_1}}{\mathbf{c}}\right) \cdot \frac{\partial f_{j0}}{\partial \mathbf{v}} \tag{B.2}$$

Substituting $\mathbf{B}$ = c ($\mathbf{k} \times \mathbf{E}$)/$\omega$ obtained from the Faraday laws to Ampere's equation, gives $\mathbf{v} \times \mathbf{B}/\mathbf{c} = \mathbf{v} \times (\mathbf{k} \times \mathbf{E})$ = $\mathbf{k}(\mathbf{v} \cdot \mathbf{E})/\omega$ - $\mathbf{E}(\mathbf{k} \cdot \mathbf{v})/\omega$ leading to

$$-k \times (k \times E_1) = \frac{\omega^2}{c^2} E_1 + \frac{4\pi}{c^2}\frac{\partial J_1}{\partial t} \tag{B.3}$$

Combining the Eq. B.2 and B.3 and using the induced current (J_1=$\Sigma_j q_j n_{j0} \int d^3 v v f_j$). This gives

$$k^2 E_1 - k \cdot E_1 - \frac{\omega^2}{c^2} E_1 + \Sigma_j \frac{\omega_{pj}^2}{c^2} E_1 - \Sigma_j \frac{\omega_{pj}^2}{c^2} \int d^3 v v \frac{\omega E_1 + v \cdot E_1 k - v \cdot k E_1}{\omega - v \cdot k} \cdot \frac{\partial f_{j0}}{\partial \mathbf{v}} = 0 \tag{B.4}$$

where $\omega_{j0} = 4\pi n_{j0} e^2/m$ is the plasma frequency. Integrating by parts $\int d^3v v E_1 \cdot \nabla_v f_{j0} = -E_1$

$$k^2 E_1 - k \cdot E_1 - \frac{\omega^2}{c^2} E_1 + \Sigma_j \frac{\omega_{pj}^2}{c^2} E_1 - \Sigma_j \frac{\omega_{pj}^2}{c^2} \int d^3v v \frac{v \cdot E_1 k}{\omega - v \cdot k} \cdot \frac{\partial f_{j0}}{\partial \mathbf{v}} = 0 \tag{B.5}$$

We examine the x component of this equation which is the perpendicula components to $k = ky$. The integrate over an odd function in v_x therefore the perpendicular component of electric component can be dropped out. We evaluate the integrate over an even function in v_y and obtained a dispersion relation in the terms of longitudinal component E_{x1} terms

$$\omega^2 - k^2 c^2 - \Sigma_j \omega_{pj}^2 - \Sigma_j \omega_{pj}^2 \int d^3v \frac{k v_x^2 \partial f_{j0}/\partial v_y}{k v_y - \omega} = 0 \tag{B.6}$$

Now, we solve the integrals by parts I_x, I_y and I_z

$$\int d^3v \frac{k v_x^2 \partial f_{j0}/\partial v_y}{k v_y - \omega} = \int d^3v \frac{v_x^2 f_{j0}}{(v_y - \omega/k)^2} = I_x, I_y, I_z \tag{B.7}$$

We chose a Maxwellian distribution function $f = (m/2\pi T_x)^{1/2}(m/2\pi T)$ $exp[-(m/2\pi T_x)v_x^2 - (m/2\pi T)(v_y^2 + v_z^2)]$ to solve the integral $I_x, I_y I_z$

$$I_x = \int dv_x v_x^2 \left(\frac{m}{2\pi T_x}\right)^{1/2} exp\left(-\frac{m}{2\pi T_x} v_x^2\right) = \frac{T_x}{m} \tag{B.8}$$

$$I_y = \int dv_y \left(\frac{m}{2\pi T}\right)^{1/2} \frac{1}{(v_y - \omega/k)^2} exp\left(-\frac{m}{2\pi T} v_y^2\right) = \frac{m}{T}[1 + \zeta Z(\zeta)] \tag{B.9}$$

$$I_z = \int dv_z \left(\frac{m}{2\pi T}\right)^{1/2} exp\left(-\frac{m}{2\pi T} v_z^2\right) = \frac{T}{m} \tag{B.10}$$

where $\zeta = \omega/k\sqrt{2T/m}$ and $Z(\zeta)$= $1/\sqrt{\pi}\int_{-\infty}^{\infty} exp(-x^2)dx/(x-\zeta)$is the plasma dispersion relation. After substituting the integral, one arrives at the following dispersion relation

$$\omega^2 - k^2 c^2 - \omega_p^2 + \omega_p^2 \left(\frac{T_{jx}}{T_j}\right)[1 + \zeta Z(\zeta)] = 0 \tag{B.11}$$

We now examine the conditions where $\zeta \ll 1$ and $\zeta \gg 1$

(A) WHEN $\zeta \ll 1$ THE PLASMA DISPERSION RELATION IS $Z(\zeta) \approx i\sqrt{\pi}$

This yields the dispersion relations:

$$-k^2c^2 - \omega_p^2\left(1 - \frac{T_{jx}}{T_j}\right) + i\sqrt{\pi}\omega_p^2\frac{\omega^2}{k^2c^2}\left(1 - \frac{T_{jx}}{T_j}\right) = 0 \tag{B.12}$$

For $\omega/kc \ll \zeta$, one can neglect ζ^2 and ω^2 as compared to k^2c^2 which gives

$$\omega = -\frac{ik}{\sqrt{\pi}}\left(\frac{T_{jx}}{T_j}\right)\left(\frac{k^2c^2}{\omega_p^2} + 1 - \frac{T_{jx}}{T_j}\right) \tag{B.13}$$

where $A = \left(1 - \frac{T_{jx}}{T_j}\right)$ is anisotropy. If $T_{jx} > T_j$, one hence obtained $Im\omega > 0$ for small enough k, so there exists an instability.

(B) WHEN $\zeta \gg 1$ THE PLASMA DISPERSION RELATION IS $Z(\zeta) \approx -1/\zeta - 1/2\zeta^3$, SO $1 + \zeta Z(\zeta) \approx -k^2c^2/2\omega^2$

This yields the dispersion relations:

$$\omega^4 - (k^2c^2 + \omega_p^2)\omega^2 - \omega_p^2k^2 \tag{B.14}$$

B.1 RELATIVISTIC WEIBEL INSTABILITY

The case of the Weibel instability with the ultra-relativistic electron streams ($v_e/c \sim 1$) was investigated by Yoon and Davidson [160]. The dispersion relation was derived in a relativistic anisotropic plasma by considering the Waterbag model

$$f(p_\perp^2, p_\parallel) = \frac{\delta(p_\perp - p_{\perp 0})}{2\pi p_\perp}\frac{\Theta(p_\parallel^2 a - p_{\parallel 0}^2)}{2p_{\parallel 0}} \tag{B.15}$$

The dispersion reads:

$$1 - \frac{c^2k^2}{\omega^2} - \frac{\omega_p^2}{\gamma\omega^2}\left(G(\beta_\parallel - \frac{1}{2}\frac{\beta_\perp}{1-\beta_\parallel^2}\frac{\omega^2 - c^2k^2}{\omega^2 - c^2k^2\beta_\parallel^2})\right) \tag{B.16}$$

where $G\beta_\parallel = 1/2\beta\|ln[(1+\beta\|)/(1-\beta\|)]$ and $\gamma = 1/(1 - \beta\perp^2 - \beta\|^2)$.

For marginal instability, we simply set $\omega = 0$

$$c^2k^2 = \frac{\omega_p^2}{\gamma\omega^2}\left(\frac{\beta_\perp^2}{2\beta_\parallel^2}\frac{1}{1-\beta_\parallel^2} - G(\beta_\parallel)\right) \tag{B.17}$$

the condition for instability to occur

$$\frac{\beta_\perp^2}{2\beta_\parallel^2} > (1-\beta_\parallel^2)G(\beta_\parallel) \tag{B.18}$$

the maximum growth rate as

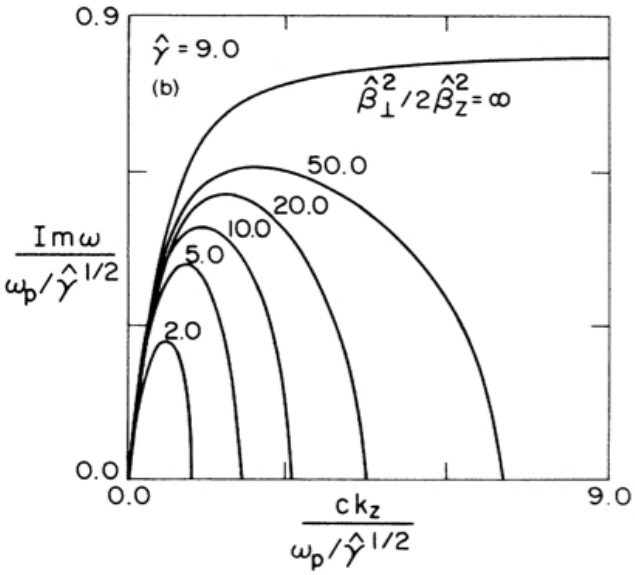

FIGURE B.1: Normalized growth rate Im $\omega[\omega_p/\gamma^{1/2}]$ vs $ck_z/[\omega_p/\gamma^{1/2}]$ for $\gamma = 9$ and several values of $\frac{\beta_\perp^2}{2\beta_\parallel^2}$

$$\Gamma = \frac{\omega_{pe}}{\gamma^{1/2}}, \tag{B.19}$$

where A = $\beta_\perp^2/2\beta_\parallel^2$ is the anisotropy factor. The instabilities are capable to generate transverse magnetic field. When the size and spacing are order of $\sim c/\omega_p$, the instability saturates. We did not mention here the magnetic field instability due to colliding electron clouds and Filamentation instability, since the free-energy sources in the latter drive purely growing magnetic fields which ought to be somehow saturated to depict the desired magnetic fields that could be associated with the observed magnetic fields in cosmic and laboratory plasmas.

APPENDIX C

THE OBLIQUE INSTABILITY

Interaction of a relativistic beam with a plasma drives the plasma instability converting the kinetic energy of electrons beam into plasma thermal energy and electromagnetic field. Two-stream and Weibel instability are unstable to $k_{\parallel}$ and $k_{\perp}$. However, Oblique mode is intermediate between two-stream and Weibel instability. We will look into a derivation of the instability based one from

To derived the dispersion relation for Oblique instability, we consider a relativistic electron beam propagating through a cold unmagnetized plasmas by ignoring the ion mass. The relevant equations to begin the derivation are the Maxwell's equation, continuity and Lorentz equations.

$$\nabla \times E_1 = -\frac{1}{c}\frac{\partial B_1}{\partial t}; \nabla \times B_1 = \frac{1}{c}\frac{\partial E_1}{\partial t} + -\frac{4\pi}{c}J_1. \tag{C.1}$$

and

$$\frac{\partial n_j}{\partial t} + \nabla \cdot n_j v_j = 0 \tag{C.2}$$

and

$$\frac{\partial P_j}{\partial t} = -\frac{e}{m}\left(\mathbf{E} + \frac{\mathbf{v} \times \mathbf{B}}{\mathbf{c}}\right) \tag{C.3}$$

where $J = q\Sigma_j n_j v_j - q n_{b0} v_{b0}$ is current density and $P_j = \gamma m v_j$ is the relativistic momentum, and $j = p, b$ is for plasma and beam electrons.

The density perturbation can be evaluated by linearizing the relativistic continuity equations

$$n_1 = \frac{n_{j0} k \cdot v_1}{\omega - k \cdot v_{j0}} \tag{C.4}$$

the variation of particle velocity can be derived

$$q\left(\mathbf{E}+\frac{\mathbf{v}\times\mathbf{B}}{\mathbf{c}}\right)=q\left[I+\frac{1}{\omega}(k_j-v_jk)\right]\cdot E \tag{C.5}$$

where I is the identity tensor.

$$\frac{\partial P_j}{\partial t}=\gamma m\frac{\partial v_j}{\partial t}+mv_j\frac{\partial\gamma}{\partial t}=\gamma m\left(\frac{\partial v_j}{\partial t}+v_j\cdot\nabla v_j\right)+mv_j\frac{\partial\gamma}{\partial t} \tag{C.6}$$

Linearizing equation (C.6) results in

$$\frac{\partial P_j}{\partial t}=\gamma_0 m\left(\frac{\partial v_{j1}}{\partial t}+v_{j0}\cdot\nabla v_{j1}\right)+mv_{j0}\frac{\partial\gamma}{\partial t} \tag{C.7}$$

The last term can be rewritten in terms of relativistic energy

$$mv_{j0}\frac{\partial\gamma}{\partial t}=\frac{v_{j0}}{c^2}\frac{d\gamma mc^2}{dt}=\frac{v_{j0}}{c^2}\frac{dW}{dt} \tag{C.8}$$

$$\frac{dW}{dt}=F\cdot v=q\left(\mathbf{E}+\frac{\mathbf{v}\times\mathbf{B}}{\mathbf{c}}\right)\cdot v \tag{C.9}$$

$$mv_{j0}\frac{\partial\gamma}{\partial t}=\frac{v_{j0}}{c^2}qE\cdot v_{j0} \tag{C.10}$$

$$\frac{\partial P_{j1}}{\partial t}=\gamma_0 m\left(\frac{\partial v_{j1}}{\partial t}+v_{j0}\nabla\cdot v_{j1}\right)+q\frac{v_{j0}}{c^2}v_{j0}\cdot E \tag{C.11}$$

$$\frac{\partial P_{j1}}{\partial t}=\gamma_0 m(i\omega v_{j1}+v_{j0}k\cdot v_{j1})+q\frac{v_{j0}}{c^2}v_{j0}\cdot E \tag{C.12}$$

where γ_{j0} is the unperturbed Lorentz factor. Neglecting second-order terms one can write

$$\frac{\partial P_{j1}}{\partial t}\approxeq q\left[I+\frac{1}{\omega}(kv_{j0}-v_{j0}k)\right]\cdot E \tag{C.13}$$

Perturbations in the plasma electron and beam velocity can be obtained by combining equ. (C.12, C.13)

$$v_{b1}=\frac{qi}{\gamma_0 m(\omega-k\cdot v_{b0})}\left[\frac{(\omega-k\cdot v_{b0})}{\omega}+\frac{kv_{b0}}{\omega}-\frac{v_{b0}}{c^2}v_{b0}\right]\cdot E \tag{C.14}$$

and

$$v_{p1}=\frac{qi}{\gamma_0 m\omega}E \tag{C.15}$$

$$J_1 = \frac{c^2}{4i\pi\omega}\left[\left(k^2 - \frac{\omega^2}{c^2}\right) I - kk\right] \cdot E \tag{C.16}$$

$$J_1 = -e[n_{p0}v_{p1} + n_{b0}v_{b0} + n_{b1}v_{b0}] \tag{C.17}$$

combining equ. C.16 and C.17, which give rise to

$$\frac{c^2 i}{4e\pi\omega}\left[\left(k^2 - \frac{\omega^2}{c^2}\right) I - kk\right] \cdot E = e\left[n_{p0}v_{p1} + n_{b0}\left(I + v_{b0}\frac{k}{(\omega - k\cdot v_{b0})}\right)\cdot v_{b1}\right] \tag{C.18}$$

or,

$$\{c^2 kk - \omega^2 - k^2c^2 - \omega_p^2 - \frac{\omega_b^2}{\gamma_0} - \frac{\omega_b^2}{(\omega - k\cdot v_{b0})^2}\left[(\omega - k\cdot v_{b0})(kv_{b0} + v_{b0}k) + \left(k^2 - \frac{\omega^2}{c^2}\right)v_{b0}v_{b0}\right]\} \cdot E = 0 \tag{C.19}$$

where ω_b is the beam frequency. The dispersion relation can be found setting up determinant to zero by using the following convention for the wavenumber $k = k_\perp \hat{e_x} + k_z \hat{e_z}$ and velocity vectors $v_{b0} = v_{b0}\hat{e_z}$, results in

$$\mathbf{A} \cdot \mathbf{E} = \mathbf{0} \tag{C.20}$$

or,

$$\mathrm{A} = \begin{bmatrix} A_{11} & 0 & A_{13} \\ 0 & A_{22} & 0 \\ A_{31} & 0 & A_{33} \end{bmatrix} \text{ where}$$

$$A_{11} = c^2k_\perp^2 - \omega^2 + k^2c^2 \tag{C.21}$$

$$A_{13} = A_{31} = c^2k_\perp k_z - \frac{\omega_b^2 k_\perp v_{b0}}{\gamma_0(\omega^2 + k^2c^2)} \tag{C.22}$$

$$A_{22} = \omega^2 - k^2c^2 - \omega_p^2 - \frac{\omega_b^2}{\gamma_0} \tag{C.23}$$

$$A_{33} = \omega^2 - k_\perp^2c^2 - \omega_p^2 - \frac{\omega_b^2\omega^2}{\gamma_0^3(\omega - k\cdot v_{b0})^2} - \frac{v_{b0}^2k_\perp^2\omega_b^2}{\gamma_0^3(\omega - k\cdot v_{b0})^2} \tag{C.24}$$

$$|A| = A_{11}A_{33} - A_{13}^2 = 0 \tag{C.25}$$

Substituting C.21, C.22 and C.24, the dispersion relation can then be rewritten as

$$\left(1-\frac{\omega_p^2}{\omega^2}-\frac{\omega_b^2}{\gamma_0^3(\omega-\mathbf{k}\cdot\mathbf{v_{b0}})^2}\right)\left(1+\frac{k^2c^2}{\omega^2}-\frac{\omega_p^2}{\omega^2}-\frac{\omega_b^2}{\gamma_0\omega^2}\right)=-\frac{v_{b0}^2k_\perp^2\omega_p^2\omega_b^2}{\omega^4\gamma_0(\omega-\mathbf{k}\cdot\mathbf{v_{b0}})^2} \tag{C.26}$$

BIBLIOGRAPHY

[1] J. N. Bahcall and J. P Ostriker. Unsolved problems in astrophysics. *Princeton University Press, Princeton, NJ08540*, pages pp. 343–377, 1997.

[2] P. P. Kronberg. Extragalactic magnetic fields. *Reports on Progress in Physics*, 57(4):325, 1994.

[3] L. W. Widrow. Origin of galactic and extragalactic magnetic fields. *Reviews of Modern Physics*, 74:775–823, 2002.

[4] A. Gruzinov and E. Waxman. Gamma-ray burst afterglow: Polarization and analytic light curves. *The Astrophysical Journal*, 511(2):852, 1999.

[5] L Vlahos, C. G. Tsagas, and D. Papadopoulos. Galaxy formation and cosmic-ray acceleration in a magnetized universe. *The Astrophysical Journal Letters*, 629(1):L9, 2005.

[6] R. Schlickeiser and P. K. Shukla. Cosmological magnetic field generation by the weibel instability. *The Astrophysical Journal Letters*, 599(2):L57, 2003.

[7] National Research Council. *Frontiers in High Energy Density Physics: The X-Games of Contemporary Science*. The National Academies Press, Washington, DC, 2003.

[8] P. P. Kronberg. Galaxies and the magnetization of intergalactic space. *Physics of Plasmas*, 10(5):1985–1991, 2003.

[9] R. Schlickeiser. On the origin of cosmological magnetic fields by plasma instabilities. *Plasma Physics and Controlled Fusion*, 47(5A):A205, 2005.

[10] M. Tatarakis, I. Watts, F. N. Beg, E. L. Clark, A. E. Dangor, A. Gopal, M. G. Haines, P. A. Norreys, U. Wagner, M.-S. Wei, M. Zepf, and K. Krushelnick. Laser technology: Measuring huge magnetic fields. *Nature*, 415:280.

[11] A. R. Bruce. High energy density laboratory astrophysics. *Plasma Physics and Controlled Fusion*, 47:A191–A203, 2005.

[12] A. A. Ruzmaikin, A.A. Shukurov, and D.D. Sokolo. Magnetic fields of galaxies. *Kluwer, Dordrecht*, 39:2422–2427, 1988.

[13] Y. B. Zeldovich, A.A. Ruzmaikin and, and D.D. Sokolo. Magnetic fields in astrophysics. *Gordon & Breach, New York*, 88:437–440, 1983.

[14] R. W. Klebesadel, I. B. Strong, and R. A. Olson. Observation of gamma-ray bursts of cosmic origin. *The Astrophysical Journal*, 182:L85–L88, 1973.

[15] G. Boella, R. C. Butler, G. C. Perola, L. Piro, L. Scarsi, and J. A. M Bleeker. Beppposax, the wide band mission for x-ray astronomy. *Astronomy and Astrophysics Supplement Series*, 122(2):299–307, 1997.

[16] G. J. Fishman and C. A. Meegan. Gamma-ray bursts. *Annual Review of Astronomy and Astrophysics*, 33(1):415–458, 1995.

[17] T. Piran. Unsolved problems in astrophysics. *Princeton University Press, Princeton, NJ08540*, NJ08540:pp. 343–377, 1998.

[18] E. Nakar and R. Sari. Relativistic shock breakouts- Äa variety of gamma-ray flares: From low-luminosity gamma-ray bursts to type ia supernovae. *The Astrophysical Journal*, 747(2):88, 2012.

[19] T. Piran. Towards understanding gamma-ray bursts. *ArXiv ID*, 9507114, 1995.

[20] P. Kumar and J. Granot. The evolution of a structured relativistic jet and gamma-ray burst afterglow light curve. *Astrophysical Journal*, 591(2):1075–1085, 2003.

[21] J. T. Frederiksen, C. B. Hededal, T. Haugbolle, and A. Nordlund. Magnetic field generation in collisionless shocks: Pattern growth and transport. *The Astrophysical Journal Letters*, 608:L13, 2004.

[22] T. Piran. The physics of gamma-ray bursts. *Reviews of Modern Physics*, 76:1143–1210, 2005.

[23] J. Goodman. Are gamma-ray-bursts optically thick? *The Astrophysical Journal Letters*, 308:L47–L50, 1986.

[24] B. Paczynski. Gamma-ray-bursts at cosmological distances. *The Astrophysical Journal Letters*, 308:L43–L46, 1986.

[25] A. Loeb. Are gamma -ray bursts at cosmological distances optically thin? *ArXiv ID*, 9308048, 1995.

[26] G. Cavallo and M. J. Rees. A qualitative study of cosmic fireballs and gamma-ray bursts. *Monthly Notices of the Royal Astronomical Society*, 183:359–365, 1978.

[27] M. J. Rees and P. Meszaros. Relativistic fireballs: energy conversion and time-scales. *The Astrophysical Journal Letters*, 308:L47, 1992.

[28] C. H. Jaroschek. Critical kinetic plasma processes in relativistic astrophysics. *Ludwig-Maximilians-Universität München*, 2005.

[29] A. Uzdensky and S. Rightley. Plasma physics of extreme astrophysical environments. *Reports on Progress in Physics*, 77:036902, 2014.

[30] E. S. Weibel. Spontaneously growing transverse waves in a plasma due to an anisotropic velocity distribution. *Physical Review Letters*, 2:83–84, 1959.

[31] E. Waxman and A. Loeb. Constraints on the local sources of ultra high-energy cosmic rays. *Journal of Cosmology and Astroparticle Physics*, 2009(08), 2009.

[32] J. Hantao and E Zweibel. Understanding particle acceleration in astrophysical plasmas. *Science*, 347(6225):944–945, 2015.

[33] K.-I. Nishikawa, J. Niemiec, P. E. Hardee, M. Medvedev, H. Sol, Y. Mizuno, B. Zhang, M. Pohl, M. Oka, and D. H. Hartmann. Weibel instability and associated strong fields in a fully three-dimensional simulation of a relativistic shock. *The Astrophysical Journal Letters*, 698(1):L10, 2009.

[34] T. Piran. Magnetic fields in gamma?ray bursts: A short overview. *AIP Conference Proceedings*, 784:164–174, 2005.

[35] R. Sari and T. Piran. Cosmological gamma-ray bursts: internal versus external shocks. *Monthly Notices of the Royal Astronomical Society*, 287(1):110, 1997.

[36] A Spitkovsky. Particle acceleration in relativistic collisionless shocks: Fermi process at last? *The Astrophysical Journal*, 682:L5–L8, 2008.

[37] A. Bret. Weibel, two-stream, filamentation, oblique, bell, buneman...which one grows faster? *The Astrophysical Journal*, 699(2):990, 2009.

[38] A. Gruzinov. Gamma-ray burst phenomenology, shock dynamo, and the first magnetic fields. *The Astrophysical Journal Letters*, 563(1):L15, 2001.

[39] R. A. Fonseca, L. O. Silva, J. Tonge, R. G. Hemker, J. M. Dawson, and W. B. Mori. Three-dimensional particle-in-cell simulations of the weibel instability in electron-positron plasmas. *IEEE Transactions on Plasma Science*, 30(1):28–29, 2002.

[40] L. O. Silva, R. A. Fonseca, J. W. Tonge, J. M. Dawson, W. B. Mori, and M. V. Medvedev. Interpenetrating plasma shells: Near-equipartition magnetic field generation and nonthermal particle acceleration. *The Astrophysical Journal Letters*, 596(1):L121, 2003.

[41] M. V. Medvedev and L. Abraham. Generation of magnetic fields in the relativistic shock of gamma-ray burst sources. *The Astrophysical Journal*, 526(2):697, 1999.

[42] N. Shukla, A. Stockem, F. Fiuza, and L. O. Silva. Enhancement in the electromagnetic beam-plasma instability due to ion streaming. *Journal Plasma Physics*, 78:181–187, 2012.

[43] P. Ade *et al.* Planck 2015 results - xiii. cosmological parameters. *Astronomy & Astronomy*, 594:A13, 2016.

[44] S. M. Carroll L. Ackerman, M. R. Buckley and M. Kamionkowski. Towards understanding gamma-ray bursts. *ArXiv ID*, arXiv:1704.00014, 2017.

[45] M. Heikinheimo, M. Raidal, C. Spethmann, and H. Veermae. Dark matter self-interactions via collisionless shocks in cluster mergers. *Physics Letters B*, 749:236–241, 2015.

[46] A. A. Scherbakov. Ignition of a laser-fusion target by a focusing shock wave. *Sov. J. Plasma Phys.*, 9:240, 1983.

[47] The National Ignition Facility project/The High Power laser Energy Research facility project:. *http://www.llnl.gov/nif/project/,http://www.hiper-laser.org/*.

[48] A. J Schmitt, Jason W. Bates, Steven P. Obenschain, Steven T. Zalesak, and David E. Fyfe. Shock ignition target design for inertial fusion energy. *Physics of Plasmas*, 17(4):042701, 2010.

[49] R. Ramis and J. Ramirez. Indirectly driven target design for fast ignition with proton beams. *Nuclear Fusion*, 44:720, 2004.

[50] B. Canaud and M. Temporal. High-gain shock ignition of direct-drive icf targets for the laser mégajoule. *New J. Phys.*, 12:043037, 2010.

[51] R. B. Campbell, R. Kodama, T. A. Mehlhorn, K. A. Tanaka, and D. R. Welch. Simulation of heating-compressed fast-ignition cores by petawatt laser-generated electrons. *Physical Review Letters*, 94:055001, 2005.

[52] R. Kodama*et.al*. Fast heating of ultrahigh-density plasma as a step towards laser fusion ignition. *Nature*, 412:798–802, 2001.

[53] P.A. Norreys, R.H.H. Scott, K.L. Lancaster, J.S. Green, A.P.L. Robinson, M. Sherlock, R.G. Evans, M.G. Haines, S. Kar, M. Zepf, M.H. Key, J. King, T. Ma, T. Yabuuchi, M.S. Wei, F.N. Beg, P. Nilson, W. Theobald, R.B. Stephens, J. Valente, J.R. Davies, K. Takeda, H. Azechi, M. Nakatsutsumi, T. Tanimoto, R. Kodama, and

K.A. Tanaka. Recent fast electron energy transport experiments relevant to fast ignition inertial fusion. *Nuclear Fusion*, 49(10):104023, 2009.

[54] K. Estabrook. Qualitative aspects of underdense magnetic fields in laser-fusion plasmas. *PRL*, 41:1808–1811, Dec 1978.

[55] N. Shukla, P. K. Shukla, and L. Stenflo. Magnetization of a warm plasma by the nonstationary ponderomotive force of an electromagnetic wave. *Physical Review E*, 80:027401, 2009.

[56] O.M. Gradov and L. Stenflo. Magnetic-field generation by a finite-radius electromagnetic beam. *Physics Letters A*, 95(5):233 – 234, 1983.

[57] V. I. Karpman and Washimi H. Two-dimensional self-modulation of a whistler wave propagating along the magnetic field in a plasma. *Journal of Plasma Physics*, 18(1):173–187, 1977.

[58] E. V. George et al. J. F. Holzrichter, D. Eimerl. High power pulsed lasers. *The Journal of Fusion Energy*, 2:1, 1982.

[59] M. G. Haines. Magnetic-field generation in laser fusion and hot-electron transport. *Canadian Journal of Physics*, 64(8):912–919, 1986.

[60] J. A. Stamper, K. Papadopoulos, R. N. Sudan, S. O. Dean, E. A. McLean, and J. M. Dawson. Spontaneous magnetic fields in laser-produced plasmas. *Physical Review Letters*, 26:1012–1015, 1971.

[61] M. Tabak, J. Hammer, M. E. Glinsky, W. L. Kruer, S. C. Wilks, J. Woodworth, E. M. Campbell, M. D. Perry, and R. J. Mason. Ignition and high gain with ultrapowerful lasers. *Physics of Plasmas*, 1(5):1626–1634, 1994.

[62] J. M Hill, M. H. Key, P. Hatchett, S., and R. F. Richard. Beam- weibel filamentation instability in near-term and fast-ignition experiments. *Physics of Plasmas*, 12:082304, 2005.

[63] C. Ren, M. Tzoufras, F. S. Tsung, W. B. Mori, S. Amorini, R. A. Fonseca, L. O. Silva, J. C. Adam, and A. Heron. Global simulation for laser-driven mev electrons in fast ignition. *Physical Review Letters*, 93:185004, 2004.

[64] T. Y. B. Yang, J Arons, and A. B. Langdon. Evolution of the weibel instability in relativistically hot electron-positron plasmas. *Physics of Plasmas*, 1(9):3059–3077, 1994.

[65] M. Honda, J. Meyer-ter Vehn, and A. Pukhov. Collective stopping and ion heating in relativistic-electron-beam transport for fast ignition. *Physical Review Letters*, 85:2128–2131, 2000.

[66] R. J. Mason. Heating mechanisms in short-pulse laser-driven cone targets. *Physical Review Letters*, 96:035001, 2006.

[67] L. O. Silva, R. A. Fonseca, and et.al J. W. Tonge. On the role of the purely transverse weibel instability in fast ignitor scenarios. *Physics of Plasmas*, 9:2458, 2002.

[68] M. Roth, T. E. Cowan, M. H. Key, S. P. Hatchett, C. Brown, W. Fountain, J. Johnson, D. M. Pennington, R. A. Snavely, S. C. Wilks, K. Yasuike, H. Ruhl, F. Pegoraro, S. V. Bulanov, E. M. Campbell, M. D. Perry, and H. Powell. Fast ignition by intense laser-accelerated proton beams. *Physical Review Letters*, 86:436–439, 2001.

[69] A. S. Sandhu, A. K. Dharmadhikari, P. P. Rajeev, G. R. Kumar, S. Sengupta, A. Das, and P. K. Kaw. Laser-generated ultrashort multimegagauss magnetic pulses in plasmas. *Physical Review Letters*, 89:225002, 2002.

[70] R. A. Fonseca, L. O. Silva, F. S. Tsung, V. K. Decyk, W. Lu, C. Ren, W. B. Mori, S. Deng, S. Lee, T. Katsouleas, and J. C. Adam. Osiris: A three-dimensional, fully relativistic particle in cell code for modeling plasma based accelerators. 2331/2002(342 – 351), 2002.

[71] R. A. Fonseca, S.F. Martins, L. O. Silva, J. W. Tonge, F.S. Tsung, and W.B. Mori. *One-to-one direct modeling of experiments and astrophysical scenarios: pushing the envelope on kinetic plasma simulations*, volume 50. IOP Publishing, 2008.

[72] C. K. Birsdall and A. B. Langdon. *Plasma physics via computer simulation*. McGraw Hill Book Company, 1985.

[73] R. L. Morse and C. W. Nielson. Numerical simulation of the weibel instability in one and two dimensions. *The Physics of Fluids*, 14(4):830–840, 1971.

[74] Open mpi: open source high performance computing. *http://www.open-mpi.org/.*

[75] Hdf: Hierarchical data format. *http://www.hdfgroup.org/.*

[76] T. Tajima and J. M. Dawson. Laser electron accelerator. *Physical Review Letters*, 43:267–270, 1979.

[77] C. Joshi, W. B. Mori, T. Katsouleas, J. M. Dawson, and D. W. Forslund. Ultrahigh gradient particle acceleration by intense laser-driven plasma density waves. *Nature*, 311:525–529, 1984.

[78] C. Joshi and T. Katsouleas. Plasma accelerators at the energy frontier and on tabletops. *Physics today*, 56:47–51, 2003.

[79] J. J. Su, T. Katsouleas, J. M. Dawson, P. Chen, M. Jones, and R. Keinigs. Stability of the driving bunch in the plasma wakefield accelerator. *IEEE Trans. Plasma Sci.*, 15(2):192–198, 1987.

[80] G. Sarri, K. Poder, J. M. Cole, W. Schumaker, A. Di Piazza, B. Reville, T. Dzelzainis, D. Doria, L. A. Gizzi, G. Grittani, S. Kar, C. H. Keitel, K. Krushelnick, S. Kuschel, S. P. D. Mangles, Z. Najmudin, N. Shukla, L. O. Silva, D. Symes, A. G. R. Thomas, M. Vargas, J. Vieira, and M. Zepf. Generation of neutral and high-density electron-positron pair plasmas in the laboratory. *Nature Communications*, 6(6747):1–6, 2015.

[81] A. Hannes. On the motion of cosmic rays in interstellar space. *Physical Review*, 55:425–429, 1939.

[82] R. B. Miller. An introduction to the physics of intense charged particle beams. *Fusion Technology*, 6(2P1):306–308, 1984.

[83] W. H. Bennett. Self-focusing streams. *Physical Review*, 98:1584–1593, 1955.

[84] I. D. Kaganovich, R. C. Davidson, M. A. Dorf, E. A. Startsev, A. B. Sefkow, E. P. Lee, and A. Friedman. Physics of neutralization of intense high-energy ion beam pulses by electrons. *Physics of Plasmas*, 17(5):056703, 2010.

[85] I. Blumenfeld, C. E. Clayton, F.J. Decker, M.J. Hogan, C. Huang, R. Ischebeck, R. Iverson, C. Joshi, T. Katsouleas, N. Kirby, W. Lu, K. Marsh, W. B. Mori, P. Muggli, E. Oz, R. Siemann, D. Waltz, and M. Zhou. Energy doubling of 43 gev electrons in metre-scale plasma wakefield accelerator. *Nature*, 445:741–744, February 2007.

[86] W. P. Leemans, B. Nagler, A. J. Gonsalves, Cs. Toth, K. Nakamura, C. G. R. Geddes, E. Esarey, C. B. Schroeder, and S. M. Hooker. Gev electron beams from a centimetre-scale accelerator. *Nature Physics*, 2:696 – 699, Sep 2006.

[87] R Bingham, J T Mendonça, and P K Shukla. Plasma based charged-particle accelerators. *Plasma Physics and Controlled Fusion*, 46(1):R1–R23, nov 2003.

[88] J. J. Su, T. Katsouleas, J. M. Dawson, P. Chen, M. Jones, and R. Keinigs. Stability of the driving bunch in the plasma wakefield accelerator. *IEEE Trans. Plasma Sci.*, 15(2):192–198, 1987.

[89] P. Chen, J. J. Su, T. Katsouleas, S. Wilks, and J. M. Dawson. Plasma focusing for high-energy beams. *IEEE Trans. Plasma Sci.*, 15(2):218 – 225, 1987.

[90] B. Allen, V. Yakimenko, M. Babzien, M. Fedurin, K. Kusche, and P. Muggli. Experimental study of current filamentation instability. *Physical Review Letters*, 109:185007, 2012.

[91] P. Muggli. Regimes of interaction between charges particle bunches and plasmas. *2014 IEEE 41st International Conference on Plasma Sciences (ICOPS) held with*

2014 IEEE International Conference on High-Power Particle Beams (BEAMS), pages 1–1, 2014.

[92] K. Floettmann. Some basic features of the beam emittance. *Physical Review Accelerators and Beams*, 6:034202, 2003.

[93] M. Reiser. Theory and design of charged particle beams. *Wiley series in beam physics and accelerator technology. John Wiley & Sons, New York*, ISBN 978-3-527-40741-5., 2008.

[94] A. Bret, L. Gremillet, and M. E. Dieckmann. Multidimensional electron beam-plasma instabilities in the relativistic regime. *Physics of Plasmas*, 17(12):120501, 2010.

[95] B. D. Fried. Mechanism for instability of transverse plasma waves. *The Physics of Fluids*, 2(3):337–337, 1959.

[96] S. A. Bludman, K. M. Watson, and M. N. Rosenbluth. Statistical mechanics of relativistic streams. ii. *The Physics of Fluids*, 3(5):747–757, 1960.

[97] A. Bret. Weibel, two-stream, filamentation, oblique, bell, buneman...which one grows faster? *The Astrophysical Journal*, 699(2):990, 2009.

[98] S. Mondal, V. Narayanan, W. J. Ding, A. D. Lad, B. Hao, S. Ahmad, W. M. Wang, Z. M. Sheng, S. Sengupta, P. Kaw, A. Das, and G. R. Kumar. Direct observation of turbulent magnetic fields in hot, dense laser produced plasmas. *Proceedings of the National Academy of Sciences*, 109:21, 2012.

[99] L. O. Silva, R. A. Fonseca, J. W. Tonge, W. B. Mori, and J. M. Dawson. On the role of the purely transverse weibel instability in fast ignitor scenarios. *Physics of Plasmas*, 9:2458, 2002.

[100] A. B. Langdon L. A. Cottrill, B. F. Lasinski, S. M. Lund, K. Molvig, M. Tabak, R. P. J. Town, and E. A. Williams. Kinetic and collisional effects on the linear evolution of fast ignition relevant beam instabilities. *Physics of Plasmas*, 15(8):082108, 2008.

[101] J. S. T. Ng. Accelerator experiments for astrophysics. *https://arxiv.org/abs/astro-ph/0310625*, 2003.

[102] P. Muggli, S. F. Martins, N. Shukla, J. Vieira, and L. O. Silva. Interaction of ultra relativistic e^-, e^+ fireball beam with plasma. *http://arxiv.org/abs/1306.4380*, 17(3), 2018.

[103] T. Y. B. Yang, J Arons, and A. B. Langdon. Evolution of the weibel instability in relativistically hot electron-positron plasmas. *Physics of Plasmas*, 1(9):3059–3077, 1994.

[104] A. Achterberg, J. Wiersma, and C. A. Norman. The weibel instability in relativistic plasmas ii. nonlinear theory and stabilization mechanism. *Astronomy & Astronomy*, 475:19–36, 2007.

[105] A Bret and L Gremillet. Oblique instabilities in relativistic electron beam plasma interaction. *Plasma Physics and Controlled Fusion*, 48(12B), 2006.

[106] M. Fiore, F. Fiuza, M. Marti, R. A. Fonseca, and L. O. Silva. Relativistic effects on the collisionless-collisional transition of the filamentation instability in fast ignition. *Journal of Plasma Physics*, 76(Special Issue 06):813–832, 2010.

[107] M. Tzoufras, C. Ren, F. S. Tsung, J. W. Tonge, W. B. Mori, M. Fiore, R. A. Fonseca, and L. O. Silva. Space-charge effects in the current-filamentation or weibel instability. *Physical Review Letters*, 96:105002, 2006.

[108] C. B. Schroeder, C. Benedetti, E. Esarey, F. J. Grüner, and W. P. Leemans. Growth and phase velocity of self-modulated beam-driven plasma waves. *Physical Review Letters*, 107:145002, 2011.

[109] F. Pegoraro, S. V. Bulanov, F. Califano, and M. Lontano. Nonlinear development of the weibel instability and magnetic field generation in collisionless plasmas. *Physica Scripta*, T63:262, 1996.

[110] A. Inglebert, A. Ghizzo, T Reveille, D. D. Sarto, P. Bertrand, and F. Califano. Multi-stream vlasov model for the study of relativistic weibel-type instabilities. *Plasma Physics and Controlled Fusion*, 54(8), 2012.

[111] F. Zwicky. On the masses of nebulae and of clusters of nebulae. *Astrophysical Journal*, 86:217, 1937.

[112] V. Trimble. Existence and nature of dark matter in the universe. *Annual Review of Astronomy and Astrophysics*, 25:425–472, 1987.

[113] H. M. Lee and J. P. Ostriker. The evolution and final disintegration of spherical stellar systems in a steady galactic tidal field. *Astrophysical Journal*, 322:123–132, 1987.

[114] A. Einstein. Lens-like action of a star by the deviation of light in the gravitational. *Science*, 84:506, 1936.

[115] F. Zwicky. Nebulae as gravitational lenses. *Physical Review Letters*, 51:290, 1937.

[116] D. Clowe, M. Bradac, A. H. Gonzalez, M. Markevitch, S. W. Randall, C. Jones, and D. Zaritsky. A direct empirical proof of the existence of dark matter. *The Astrophysical Journal Letters*, 648(L109-L113), 2006.

[117] P. Collaboration *et. al*. Planck 2015 results. xiii. cosmological parameters. *Astronomy & Astrophysics*, 594(63), 2015.

[118] M. Kamionkowski G. Jungman and K. Griest. Supersymmetric dark matter. *Physics Reports*, 267(195-373), 1996.

[119] L. Baudis. Darwin dark matter wimp search with noble liquids. *Journal of Physics: Conference Series*, 375(012028), 2012.

[120] L. Ackerman, M. R. Buckley, S. M. Carroll, and M. Kamionkowski. Dark matter and dark radiation. *Physical Review D*, 79(023519), 2009.

[121] J. L. Feng, M. Kaplinghat, H. Tu, and H.-B. Yu. Hidden charged dark matter. *Journal of Cosmology and Astroparticle Physics*, 0907(004), 2009.

[122] P. Ko, N. Nagata, and Y. Tang. Hidden charged dark matter and chiral dark radiation. *Physics Letters B*, 773:513 – 520, 2017.

[123] P. Agrawal, F. Cyr-Racine, L. Randall, and J. Scholtz. Make dark matter charged again. *Journal of Cosmology and Astroparticle Physics*, 2017(05):022–022, 2017.

[124] A. Kamada, M. Kaplinghat, A. B. Pace, and H. Yu. Self-interacting dark matter can explain diverse galactic rotation curves. *Physical Review Letters*, 119:111102, 2017.

[125] B. Rennan. Possible interaction between baryons and dark-matter particles revealed by the first stars. *Nature*, 555:71, 2018.

[126] D. Clowe, A. Gonzalez, and M. Markevitch. Weak-lensing mass reconstruction of the interacting cluster 1e 0657-558: Direct evidence for the existence of dark matter. *The Astrophysical Journal*, 604(2):596–603, 2004.

[127] D. Bohm and E. P. Gross. Theory of plasma oscillations. a. origin of medium-like behavior. *Physical Review*, 75:1851–1864, 1949.

[128] Y. B. Fainberg, V. D. Shapiro, and V. I. Shevchenko. Nonlinear theory of interaction between a monochromatic beam of relativistic electrons and a plasmas. *JETP Letters*, 30(2):528, 1970.

[129] M. Heikinheimo, M. Raidal, C. Spethmann, and H. Veermae. Dark matter self-interactions via collisionless shocks in cluster mergers. *Physics Letters B*, 749:236 –241, 2015.

[130] G. Perry, M. D. an d Mourou. Terawatt to petawatt sub-picosecond lasers. *Science*, 264(5161):917–924, 1994.

[131] L. Biermann. über den ursprung der magnetfelder auf sternen und im interstellaren raum. *znt*, 5A:65, 1950.

[132] M. E. Dieckmann, P. K. Shukla, and L. Stenflo. Simulation study of the filamentation of counter-streaming beams of the electrons and positrons in plasmas. *Plasma Physics and Controlled Fusion*, 51(6), 2009.

[133] J. J. Deschamps, M. Fitaire, and M. Lagoutte. Inverse faraday effect in a plasma. *Physical Review Letters*, 25:1330–1332, 1970.

[134] Z. Najmudin, M. Tatarakis, E. L. Clark A. Pukhov, R. J. Clarke, A. E. Dangor, J. Faure, V. Malka, D. Neely, M. I. K. Santala, and K. Krushelnick. Measurements of the inverse faraday effect from relativistic laser interactions with an underdense plasma. *Physical Review Letters*, 87:215004, 2001.

[135] V. I. Karpman and H. Washimi. Two-dimensional self-modulation of a whistler wave propagating along the magnetic field in a plasma. *Journal of Plasma Physics*, 18(1):173–187, 1977.

[136] B.J. Green and P. Mulser. Ponderomotive forces in the interaction of laser radiation with a plasma. *Physics Letters A*, 37(4):319 – 320, 1971.

[137] M. G. Haines. Magnetic-field generation in laser fusion and hot-electron transport. *Canadian Journal of Physics*, 64(8):912–919, 1986.

[138] S. C. Wilks, W. L. Kruer, M. Tabak, and A. B. Langdon. Absorption of ultraintense laser pulses. *Physical Review Letters*, 69:1383–1386, 1992.

[139] R. N. Sudan. Mechanism for the generation of 10^9 g magnetic fields in the interaction of ultraintense short laser pulse with an overdense plasma target. *Physical Review Letters*, 70:3075–3078, 1993.

[140] I. Watts M. Tatarakis, F. N. Beg, E. L. Clark, A. E. Dangor, A. Gopal, M. G. Haines, P. A. Norreys, U. Wagner, M.-S. Wei, M. Zepf, and K. Krushelnick. Laser technology: Measuring huge magnetic fields. *Nature (London)*, 415:280, 2002.

[141] N. L. Kugland, D. D. Ryutov, P-Y. Chang, R. P. Drake, G. Fiksel, D. H. Froula, S. H. Glenzer, G. Gregori, M. Grosskopf, M. Koenig, Y. Kuramitsu, C. Kuranz, M. C. Levy, E. Liang, J. Meinecke, F. Miniati, T. Morita, A. Pelka, C. Plechaty, R. Presura, A. Ravasio, B. A. Remington, B. Reville, J. S. Ross, Y. Sakawa, A. Spitkovsky, H. Takabe, and H-S. Park. Self-organized electromagnetic field structures in laser-produced counter-streaming plasmas. *Nature Physics*, 8:809–812, 2012.

[142] C. Ruyer, L. Gremillet, and G. Bonnaud. Weibel-mediated collisionless shocks in laser-irradiated dense plasmas: Prevailing role of the electrons in generating the field fluctuations. *Physics of Plasmas*, 22(8):082107, 2015.

[143] N. Shukla, P. K. Shukla, and L. Stenflo. Magnetization of a warm plasma by the nonstationary ponderomotive force of an electromagnetic wave. *Physics Review E*, 80:027401, 2009.

[144] M. S. Wei, F. N. Beg, E. L. Clark, A. E. Dangor, R. G. Evans, A. Gopal, K. W. D. Ledingham, P. McKenna, P. A. Norreys, M. Tatarakis, M. Zepf, and K. Krushelnick. Observations of the filamentation of high-intensity laser-produced electron beams. *Physical Review E*, 70:056412, 2004.

[145] C. M. Huntington, F. Fiuza, and J. S. Ross et al. Observation of magnetic field generation via the weibel instability in interpenetrating plasma flows. *Nature Physics*, 11:173–176, 2015.

[146] Y. Sakagami, H. Kawakami, S. Nagao, and C. Yamanaka. Two-dimensional distribution of self-generated magnetic fields near the laser-plasma resonant-interaction region. *Physics Review Letter*, 42:839–842, 1979.

[147] K. M. Schoeffler, N. F. Loureiro, R. A. Fonseca, and L. O. Silva. Magnetic-field generation and amplification in an expanding plasma. *Physics Review Letter*, 112:175001, 2014.

[148] S. C. Wilks and W. L. Kruer. Absorption of ultrashort, ultra-intense laser light by solids and overdense plasmas. *IEEE Journal of Quantum Electronics*, 33(11):1954–1968, 1997.

[149] L. Chopineau, A. Leblanc, G. Blaclard, A. Denoeud, M. Thévenet, J-L. Vay, G. Bonnaud, Ph. Martin, H. Vincenti, and F. Quéré. Identification of coupling mechanisms between ultraintense laser light and dense plasmas. *arXiv.org*, 1809.03903, 2018.

[150] A. Pukhov, Z.-M. Sheng, and J. Meyer ter Vehn. Particle acceleration in relativistic laser channels. *Physics of Plasmas*, 6:2847, 1999.

[151] J D Huba. *NRL PLASMA FORMULARY Supported by The Office of Naval Research*. Naval Research Laboratory, Washington, DC, 2013.

[152] K. M. Schoeffler, N. F. Loureiro, R. A. Fonseca, and L. O. Silva. The generation of magnetic fields by the biermann battery and the interplay with the weibel instability. *Physics of Plasmas*, 23(5):056304, 2016.

[153] K. M. Schoeffler, N. F. Loureiro, and L. O. Silva. The fully kinetic biermann battery and associated generation of pressure anisotropy. *Physical Review E*, 97:033204, 2018.

[154] H. H. Kaang, C-M Ryu, and P. H. Yoon. Nonlinear saturation of relativistic weibel instability driven by thermal anisotropy. *Physics of Plasmas*, 16:082103, 2009.

[155] Y. J. Li and J. Zhang. Hydrodynamic characteristics of transient ni-like x-ray lasers. *Physical Review E*, 63:036410, 2001.

[156] P. Kolodner and E. Yablonovitch. Two-dimensional distribution of self-generated magnetic fields near the laser-plasma resonant- interaction region. *Physical Review Letters*, 43:1402–1403, 1979.

[157] M. Tatarakis, A. Gopal, I. Watt et. al. Measurements of ultra-strong magnetic fields during relativistic laser- plasma interactions. *Physics of Plasmas*, 9:2244, 2002.

[158] S. Göde, C. Rödel, K. Zeil, R. Mishra, M. Gauthier, F.-E. Brack, T. Kluge, M. J. MacDonald, J. Metzkes, L. Obst, M. Rehwald, C. Ruyer, H.-P. Schlenvoigt, W. Schumaker, P. Sommer, T. E. Cowan, U. Schramm, S. Glenzer, and F. Fiuza. Relativistic Electron Streaming Instabilities Modulate Proton Beams Accelerated in Laser-Plasma Interactions. *Physical Review Letters*, 118:194801, 2017.

[159] `www.clf.stfc.ac.uk/Pages/Vulcan-laser.aspx`.

[160] P. H. Yoon and R. C. Davidson. Exact analytical model of the classical weibel instability in a relativistic anisotropic plasma. *Physical Review A*, 35:2718–2721, 1987.